

---

# THICK/THIN PLATES. REISSNER-MINDLIN THEORY

## 6.1 INTRODUCTION

Kirchhoff plate elements studied in the previous chapter are restricted to thin plate situations only (thickness/average side  $\leq 0.10$ ). Also the  $C^1$  continuity requirement for Kirchhoff elements poses severe difficulties for deriving a conforming deflection field. These problems can be overcome by using the plate formulation due to Reissner [Re] and Mindlin [Mi] presented in this chapter.

The so called Reissner-Mindlin plate theory assumes that the normals to the plate do not remain orthogonal to the mid-plane after deformation, thus allowing for transverse shear deformation effects. This assumption is analogous to that made for the rotation of the transverse cross section in Timoshenko beam theory (Chapter 2). This allows us to use  $C^0$  continuous elements. Unfortunately, some difficulties arise when Reissner-Mindlin elements are used for thin plate situations due to the excessive influence of the transverse shear deformation terms. The “shear locking” defect is analogous to that found when Timoshenko beam elements are applied to slender beams. Elimination of shear locking is possible via reduced integration, linked interpolations or assumed transverse shear strain fields, similarly as described for beams in Chapter 2.

Reissner-Mindlin plate elements can be taken as the starting point for deriving  $C^0$  continuous thin plate elements by adequately constraining the transverse shear deformation to be zero at selected element points. Some of the so called Discrete-Kirchhoff (DK) plate elements are described.

A method for extending the basic rotation-free plate triangle described in Section 5.8.2 to accounting for shear deformation effects is also outlined in the last part of the chapter.

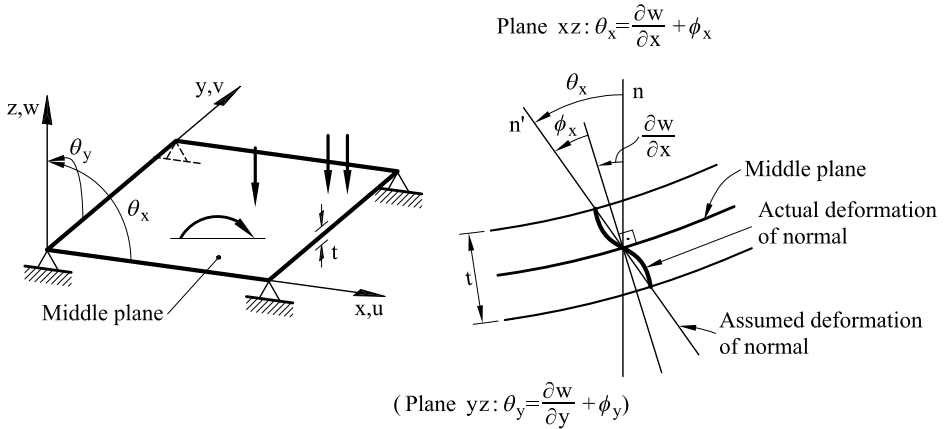


**Fig. 6.1** Reissner-Mindlin plate theory. Sign convention for the displacements and the rotations of the normal. For loading types see [Figure 4.1](#).

Reissner-Mindlin plate theory is very adequate for studying composite laminate plates for which shear deformation effects are important. The derivation of finite elements for this type of structures is presented in the next chapter.

Reissner-Mindlin plate theory can be readily extended to shell analysis. The study of this and the following chapters is therefore recommended as an introduction to the chapters dealing with shell structures.

The simplicity of Reissner-Mindlin plate elements and their versatility for analysis of thick and thin plates with homogeneous and composite material have contributed to their popularity for practical applications (see references in chapters on plate analysis in [CMPW,Cr,HO,ZT2]).

## 6.2 REISSNER-MINDLIN PLATE THEORY

Reissner-Mindlin plate bending theory shares the first three assumptions of Kirchhoff plate theory (Section 5.2.1). The fourth assumption on the rotation of the normal is different and reads as follows:

- 4) A straight line normal to the undeformed middle plane *remains straight* but *not necessarily orthogonal* to the middle plane after deformation ([Figure 6.1](#)).

The reader will recognize the analogy of this assumption with that for the rotation of the cross section in Timoshenko beams (Section 2.2). There are in fact many common features between both plate and beam theories.

### 6.2.1 Displacement field

The 3D displacement field is expressed in terms of the middle plane kinematic variables  $w$ ,  $\theta_x$  and  $\theta_y$  as

$$\begin{aligned} u(x, y, z) &= -z\theta_x(x, y) \\ v(x, y, z) &= -z\theta_y(x, y) \\ w(x, y, z) &= w(x, y) \end{aligned} \quad (6.1)$$

where  $\theta_x$  and  $\theta_y$  are the angles defining the rotation of the normal vector. Eq.(6.1) is identical to (5.2) for Kirchhoff theory. Here again the middle plane is taken as the reference plane ( $z = 0$ ). The displacement vector is

$$\mathbf{u} = [w, \theta_x, \theta_y]^T \quad (6.2)$$

Assumption 4 of previous page allows us to express the rotation of the normal on the plane  $xz$  as (Figure 6.1)

$$\theta_x = \frac{\partial w}{\partial x} + \phi_x \quad (6.3)$$

Similarly, for the plane  $yz$

$$\theta_y = \frac{\partial w}{\partial y} + \phi_y \quad (6.4)$$

The rotation of the normal in each of the two vertical planes  $xz$  and  $yz$  is obtained as the sum of two terms: 1) the adequate slope of the plate middle plane, and 2) an additional rotation  $\phi$  resulting from the lack of orthogonality of the normal with the middle plane after deformation (Figure 6.1). Consequently, the rotations  $\theta_x$  and  $\theta_y$  can not be computed in terms of the deflection only and, therefore, are treated as *independent variables*. This is a substantial difference between Reissner–Mindlin and Kirchhoff plate theories.

The assumption of straight normals is an approximation of the true plate kinematics as in reality the plate normals are distorted during deformation. Clearly this effect is more important for thick plates. The angles  $\theta_x$  and  $\theta_y$  can be interpreted as the rotations of the straight line representing the “average” deformation of the normal (Figure 6.1).

### 6.2.2 Strain and stress fields

Substituting the displacement field (6.1) into the expression for the strains in a 3D solid (see Eq.(8.3) of [On4]) gives

$$\varepsilon_x = \frac{\partial u}{\partial x} = -z \frac{\partial \theta_x}{\partial x}$$

$$\begin{aligned}
\varepsilon_y &= \frac{\partial v}{\partial y} = -z \frac{\partial \theta_y}{\partial y} \\
\varepsilon_z &= \frac{\partial w}{\partial z} = 0 \\
\gamma_{xy} &= \frac{\partial u}{\partial y} + \frac{\partial v}{\partial x} = -z \left( \frac{\partial \theta_x}{\partial y} + \frac{\partial \theta_y}{\partial x} \right) \\
\gamma_{xz} &= \frac{\partial u}{\partial z} + \frac{\partial w}{\partial x} = -\theta_x + \frac{\partial w}{\partial x} = -\phi_x \\
\gamma_{yz} &= \frac{\partial v}{\partial z} + \frac{\partial w}{\partial y} = -\theta_y + \frac{\partial w}{\partial y} = -\phi_y
\end{aligned} \tag{6.5}$$

The non-orthogonality of the normal vector induces *non zero transverse shear strains*  $\gamma_{xz}$  and  $\gamma_{yz}$ , which coincide (in absolute value) with the rotations  $\phi_x$  and  $\phi_y$ . These strains are independent of the coordinate  $z$ .

Making zero the transverse shear strains we recover the normal orthogonality condition of Kirchhoff plate theory as  $\theta_x = \frac{\partial w}{\partial x}$  and  $\theta_y = \frac{\partial w}{\partial y}$ .

The same comments on the irrelevance of the normal strain  $\varepsilon_z$  made in Section 5.2.3 apply in this case.

The strain vector containing the significant strains is therefore

$$\boldsymbol{\varepsilon} = \begin{Bmatrix} \varepsilon_x \\ \varepsilon_y \\ \gamma_{xy} \\ \dots\dots\dots \\ \gamma_{xz} \\ \gamma_{yz} \end{Bmatrix} = \begin{Bmatrix} -z \frac{\partial \theta_x}{\partial x} \\ -z \frac{\partial \theta_y}{\partial y} \\ -z \left( \frac{\partial \theta_x}{\partial y} + \frac{\partial \theta_y}{\partial x} \right) \\ \dots\dots\dots \\ \frac{\partial w}{\partial x} - \theta_x \\ \frac{\partial w}{\partial y} - \theta_y \end{Bmatrix} = \begin{Bmatrix} \boldsymbol{\varepsilon}_b \\ \dots\dots\dots \\ \boldsymbol{\varepsilon}_s \end{Bmatrix} \tag{6.6}$$

where vectors  $\boldsymbol{\varepsilon}_b$  and  $\boldsymbol{\varepsilon}_s$  contain the bending and transverse shear strains, respectively. The strain vector of Eq.(6.6) can be expressed as

$$\boldsymbol{\varepsilon} = \mathbf{S} \hat{\boldsymbol{\varepsilon}} \tag{6.7}$$

where

$$\hat{\boldsymbol{\varepsilon}} = \begin{Bmatrix} \hat{\boldsymbol{\varepsilon}}_b \\ \hat{\boldsymbol{\varepsilon}}_s \end{Bmatrix} \tag{6.8}$$

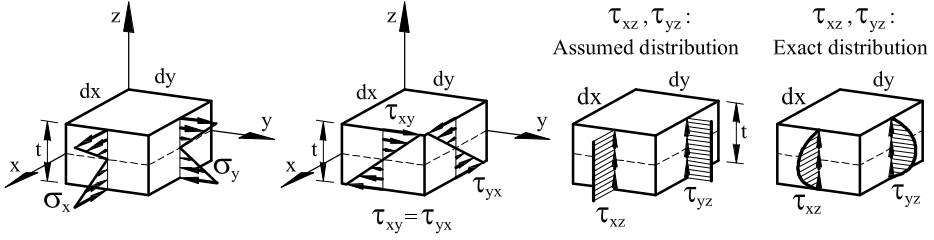


**Fig. 6.2** Sign convention for the in-plane stresses  $\sigma_x$ ,  $\sigma_y$ ,  $\tau_{xy}$  and the transverse shear stresses  $\tau_{xz}$  and  $\tau_{yz}$

is the *generalized strain vector* and

$$\hat{\epsilon}_b = \begin{Bmatrix} \frac{\partial \theta_x}{\partial x} \\ \frac{\partial \theta_y}{\partial y} \\ \left( \frac{\partial \theta_x}{\partial y} + \frac{\partial \theta_y}{\partial x} \right) \end{Bmatrix} \quad \text{and} \quad \hat{\epsilon}_s = \begin{Bmatrix} \frac{\partial w}{\partial x} - \theta_x \\ \frac{\partial w}{\partial y} - \theta_y \end{Bmatrix} \quad (6.9)$$

are the generalized bending strain vector and the transverse shear strain vector, respectively. The strain transformation matrix  $\mathbf{S}$  in Eq.(6.7) is

$$\mathbf{S} = \begin{bmatrix} -z & 0 & 0 & 0 & 0 \\ 0 & -z & 0 & 0 & 0 \\ 0 & 0 & -z & 0 & 0 \\ 0 & 0 & 0 & 1 & 0 \\ 0 & 0 & 0 & 0 & 1 \end{bmatrix} \quad (6.10)$$

The stress vector is

$$\boldsymbol{\sigma} = \begin{Bmatrix} \sigma_x \\ \sigma_y \\ \tau_{xy} \\ \dots \\ \tau_{xz} \\ \tau_{yz} \end{Bmatrix} = \begin{Bmatrix} \boldsymbol{\sigma}_b \\ \dots \\ \boldsymbol{\sigma}_s \end{Bmatrix} \quad (6.11)$$

where  $\boldsymbol{\sigma}_b$  and  $\boldsymbol{\sigma}_s$  are the stresses due to pure bending and transverse shear effects, respectively. As usual in plate theory  $\sigma_z$  has been excluded from Eq.(6.11) due to the plane stress assumption ( $\sigma_z = 0$ ). The sign convention for the stresses is shown in [Figure 6.2](#).

### 6.2.3 Stress–strain relationship

We will consider in the following the material to be *homogeneous* and isothermal conditions only. This is consistent with the assumption of plate bending theory, as no axial strains or axial forces are introduced during the plate deformation. Axial effects appear for composite laminated plates or when thermal effects are taken into account. These situations are treated in the next chapter.

Starting from the constitutive equation of 3D elasticity (Eq.(8.5) of [On4]) and using the plane stress assumption ( $\sigma_z = 0$ ), we can find a relationship between the non-zero stresses and strains. For an *orthotropic* material with orthotropy axes 1,2,3 with 3 =  $z$  and satisfying the condition of plane anisotropy (i.e. the plane 1,2 is a plane of material symmetry [BD4]) we can write

$$\boldsymbol{\sigma}_I = \begin{Bmatrix} \boldsymbol{\sigma}_1 \\ \boldsymbol{\sigma}_2 \end{Bmatrix} = \begin{bmatrix} \mathbf{D}_1 & \vdots & \mathbf{0} \\ \dots & \dots & \dots \\ \mathbf{0} & \vdots & \mathbf{D}_2 \end{bmatrix} \begin{Bmatrix} \boldsymbol{\varepsilon}_1 \\ \boldsymbol{\varepsilon}_2 \end{Bmatrix} = \mathbf{D}_I \boldsymbol{\varepsilon}_I \quad (6.12)$$

where

$$\begin{aligned} \boldsymbol{\sigma}_1 &= [\sigma_1, \sigma_2, \tau_{12}]^T, & \boldsymbol{\sigma}_2 &= [\tau_{13}, \tau_{23}]^T \\ \boldsymbol{\varepsilon}_1 &= [\varepsilon_1, \varepsilon_2, \gamma_{12}]^T, & \boldsymbol{\varepsilon}_2 &= [\gamma_{13}, \gamma_{23}]^T \end{aligned} \quad (6.13)$$

are the bending and transverse shear stresses and strains in the principal orthotropy axes and

$$\mathbf{D}_1 = \frac{1}{1 - \nu_{12}\nu_{21}} \begin{bmatrix} E_1 & \nu_{21}E_1 & 0 \\ \nu_{12}E_1 & E_2 & 0 \\ 0 & 0 & (1 - \nu_{12}\nu_{21})G_{12} \end{bmatrix}, \quad \mathbf{D}_2 = \begin{bmatrix} G_{13} & 0 \\ 0 & G_{23} \end{bmatrix} \quad (6.14)$$

with  $\nu_{12}E_2 = \nu_{21}E_1$ . If isotropy exists in the direction 1 (i.e. on the plane 2 –  $z$ , [Figure 6.3](#)) as for fiber composites with fibers in the direction 1 covered by a matrix, then  $G_{13} = G_{12}$ .

The following relationships hold [BC,BD4,CMPW]

$$\begin{aligned} \boldsymbol{\varepsilon}_1 &= \mathbf{T}_1 \boldsymbol{\varepsilon}_b, & \boldsymbol{\varepsilon}_2 &= \mathbf{T}_2 \boldsymbol{\varepsilon}_s \\ \boldsymbol{\sigma}_b &= \mathbf{T}_1^T \boldsymbol{\sigma}_1, & \boldsymbol{\sigma}_s &= \mathbf{T}_2^T \boldsymbol{\sigma}_2 \end{aligned} \quad (6.15a)$$

with

$$\mathbf{T}_1 = \begin{bmatrix} C^2 & S^2 & CS \\ S^2 & C^2 & -CS \\ -2CS & 2CS & C^2 - S^2 \end{bmatrix}, \quad \mathbf{T}_2 = \begin{bmatrix} C & S \\ -S & C \end{bmatrix} \quad (6.15b)$$

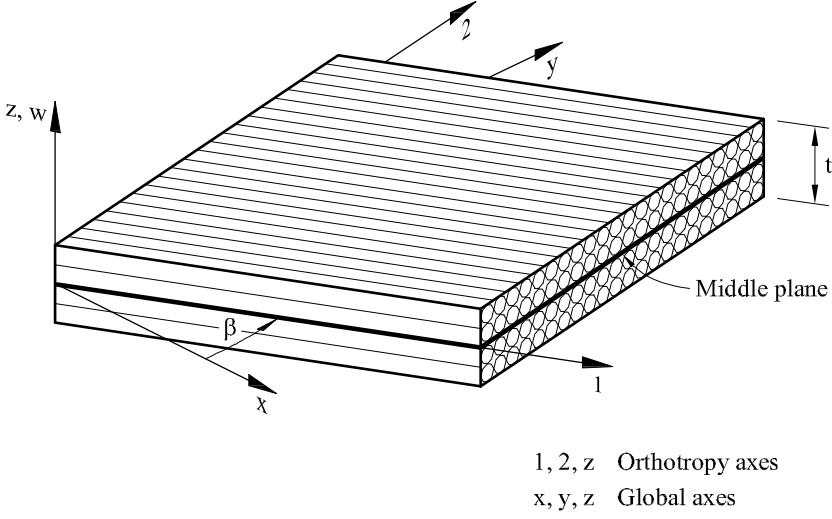


**Fig. 6.3** Orthotropic material in the plane 1-2 and isotropic in the plane 2 - z

where  $C = \cos \beta$ ,  $S = \sin \beta$  and  $\beta$  is the angle between the axes 1 and  $x$  (Figure 6.3) and  $\epsilon_b$ ,  $\epsilon_s$  are defined in Eq.(6.6).

The inverse relationship can be obtained simply by replacing  $\beta$  by  $-\beta$  in Eqs.(6.15) [BC], i.e.

$$\begin{aligned} \epsilon_b &= \bar{\mathbf{T}}_1 \epsilon_1 \quad , \quad \epsilon_s = \bar{\mathbf{T}}_2 \epsilon_2 \\ \sigma_1 &= \bar{\mathbf{T}}_1^T \sigma_b \quad , \quad \sigma_2 = \bar{\mathbf{T}}_2^T \sigma_s \end{aligned} \quad (6.16a)$$

with

$$\bar{\mathbf{T}}_1 = \begin{bmatrix} C^2 & S^2 & -CS \\ S^2 & C^2 & CS \\ 2CS & -2CS & C^2 - S^2 \end{bmatrix} \quad , \quad \bar{\mathbf{T}}_2 = \begin{bmatrix} C & -S \\ S & C \end{bmatrix} \quad (6.16b)$$

Combining Eqs.(6.12) and (6.15) gives the constitutive equations for the bending and transverse shear stresses in global axes as

$$\sigma_b = \mathbf{D}_b \epsilon_b \quad , \quad \sigma_s = \bar{\mathbf{D}}_s \epsilon_s \quad (6.17a)$$

or

$$\sigma = \begin{Bmatrix} \sigma_b \\ \sigma_s \end{Bmatrix} = \mathbf{D} \begin{Bmatrix} \epsilon_b \\ \epsilon_s \end{Bmatrix} = \mathbf{D} \epsilon \quad \text{with} \quad \mathbf{D} = \begin{bmatrix} \mathbf{D}_b & \mathbf{0} \\ \mathbf{0} & \bar{\mathbf{D}}_s \end{bmatrix} \quad (6.17b)$$

and

$$\mathbf{D}_b = \mathbf{T}_1^T \mathbf{D}_1 \mathbf{T}_1, \quad \bar{\mathbf{D}}_s = \mathbf{T}_2^T \mathbf{D}_2 \mathbf{T}_2 \quad (6.17c)$$

The case of isotropic material is simply recovered for  $\beta = 0$ , giving

$$\mathbf{D}_b = \frac{E}{1-\nu^2} \begin{bmatrix} 1 & \nu & 0 \\ \nu & 1 & 0 \\ 0 & 0 & \frac{1-\nu}{2} \end{bmatrix}, \quad \bar{\mathbf{D}}_s = G \begin{bmatrix} 1 & 0 \\ 0 & 1 \end{bmatrix} \quad (6.18)$$

Substituting Eq.(6.7) into (6.17) gives the relationship between the stresses at a point across the thickness and the generalized strains as

$$\boldsymbol{\sigma} = \begin{Bmatrix} \sigma_b \\ \sigma_s \end{Bmatrix} = \mathbf{D}\mathbf{S}\hat{\boldsymbol{\epsilon}} = \mathbf{D} \begin{Bmatrix} -z\hat{\boldsymbol{\epsilon}}_b \\ \hat{\boldsymbol{\epsilon}}_s \end{Bmatrix} \quad (6.19)$$

Eq.(6.19) shows that the distribution of the “in-plane” bending stresses  $\sigma_x$ ,  $\sigma_y$  and  $\tau_{xy}$  varies linearly with  $z$ , while the transverse shear stresses  $\tau_{xz}$  and  $\tau_{yz}$  are constant across the thickness (Figure 6.2).

The “exact” thickness distribution of the transverse shear stresses obtained from 3D elasticity theory is not uniform and they vanish at the upper and lower plate surfaces. For isotropic material the distribution is parabolic (Figure 6.2) [TW]. This problem, which also appeared for Timoshenko beam theory (Section 2.2.3), can be overcome by scaling the internal work associated to the transverse shear stresses so that it coincides with the exact internal work obtained from 3D elasticity theory. Thus, the total strain work is computed exactly, although the transverse shear stresses have not a correct thickness distribution locally.

In practice this implies modifying the shear constitutive relationship of Eq.(6.17a) as

$$\boldsymbol{\sigma}_s = \mathbf{D}_s \boldsymbol{\epsilon}_s \quad \text{with} \quad \mathbf{D}_s = \begin{bmatrix} k_{11} \bar{D}_{s11} & k_{12} \bar{D}_{s12} \\ k_{12} \bar{D}_{s12} & k_{22} \bar{D}_{s22} \end{bmatrix} \quad (6.20)$$

where  $\mathbf{D}_{sij}$  are the components of  $\bar{\mathbf{D}}_s$  of Eq.(6.17c) and  $k_{ij}$  are shear correction parameters. Their computation follows a procedure analogous to that explained for Timoshenko beams. For an isotropic plate  $k_{12} = 0$  and  $k_{11} = k_{22} = 5/6$ , as for rectangular beams (Section 2.2.3.1). The computation of the shear correction parameters for composite laminated beams is presented in Section 7.3 and in Annex D.

## 6.2.4 Resultant stresses and generalized constitutive matrix

The vector of resultant stresses at a point of the plate middle plane is



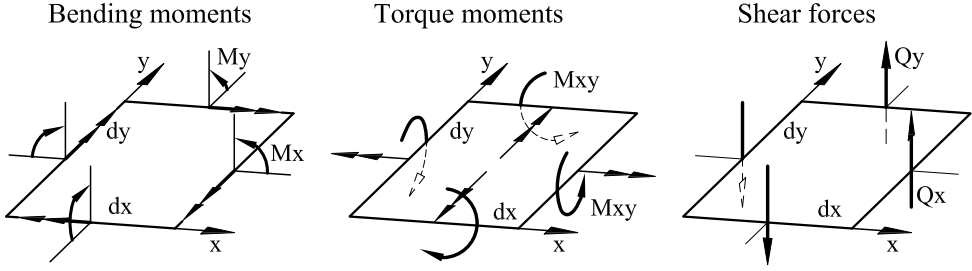


**Fig. 6.4** Sign convention for the resultant stresses in a plate

defined as

$$\begin{aligned}
 \hat{\sigma} &= \begin{Bmatrix} \hat{\sigma}_b \\ \dots \\ \hat{\sigma}_s \end{Bmatrix} = \begin{Bmatrix} M_x \\ M_y \\ M_{xy} \\ \dots \\ Q_x \\ Q_y \end{Bmatrix} = \int_{-\frac{t}{2}}^{+\frac{t}{2}} \begin{Bmatrix} -z\sigma_x \\ -z\sigma_y \\ -z\tau_{xy} \\ \dots \\ \tau_{xz} \\ \tau_{yz} \end{Bmatrix} dz = \\
 &= \int_{-\frac{t}{2}}^{+\frac{t}{2}} \begin{Bmatrix} -z\sigma_b \\ \dots \\ \sigma_s \end{Bmatrix} dz = \int_{-\frac{t}{2}}^{+\frac{t}{2}} \mathbf{S}^T \boldsymbol{\sigma} dz
 \end{aligned} \tag{6.21}$$

where  $\mathbf{S}$  is the transformation matrix of Eq.(6.10) and vectors  $\hat{\sigma}_b$  and  $\hat{\sigma}_s$  contain the *moments* and the *shear forces*, respectively. For sign convention see [Figure 6.4](#).

Eq.(6.21) can be modified using Eqs.(6.17) and (6.7) as

$$\hat{\sigma} = \begin{Bmatrix} \hat{\sigma}_b \\ \dots \\ \hat{\sigma}_s \end{Bmatrix} = \int_{-\frac{t}{2}}^{+\frac{t}{2}} \mathbf{S}^T \mathbf{D} \boldsymbol{\varepsilon} dz = \int_{-\frac{t}{2}}^{+\frac{t}{2}} \mathbf{S}^T \mathbf{D} \mathbf{S} \hat{\boldsymbol{\varepsilon}} dz = \int_{-\frac{t}{2}}^{+\frac{t}{2}} \begin{Bmatrix} z^2 \mathbf{D}_b \hat{\boldsymbol{\varepsilon}}_b \\ \dots \\ \mathbf{D}_s \hat{\boldsymbol{\varepsilon}}_s \end{Bmatrix} dz = \hat{\mathbf{D}} \hat{\boldsymbol{\varepsilon}} \tag{6.22}$$

where  $\hat{\boldsymbol{\varepsilon}}$  is the generalized strain vector of Eq.(6.9) and

$$\hat{\mathbf{D}} = \int_{-\frac{t}{2}}^{+\frac{t}{2}} \mathbf{S}^T \mathbf{D} \mathbf{S} dz = \int_{-\frac{t}{2}}^{+\frac{t}{2}} \begin{bmatrix} z^2 \mathbf{D}_b & \mathbf{0} \\ \mathbf{0} & \mathbf{D}_s \end{bmatrix} dz = \begin{bmatrix} \hat{\mathbf{D}}_b & \mathbf{0} \\ \mathbf{0} & \hat{\mathbf{D}}_s \end{bmatrix} \tag{6.23}$$

is the *generalized constitutive matrix* with  $\mathbf{D}_b$  and  $\mathbf{D}_s$  given in Eqs.(6.17c) and (6.20), respectively.

For isotropic material

$$\hat{\mathbf{D}}_b = \frac{t^3}{12} \mathbf{D}_b \quad \text{and} \quad \hat{\mathbf{D}}_s = t \mathbf{D}_s = \frac{5}{6} t G \mathbf{I}_2 \tag{6.24}$$

where  $\mathbf{D}_b$  is given by Eq.(6.18) and  $\mathbf{I}_2$  is the  $2 \times 2$  unit matrix.

Eq.(6.22) relates the resultant stresses and the generalized strains at any point of the plate surface. The stresses across the thickness can be recovered from the generalized strains combining Eqs.(6.7) and (6.17) as

$$\boldsymbol{\sigma} = \mathbf{D}\mathbf{S}\hat{\boldsymbol{\varepsilon}} \quad (6.25)$$

Eq.(6.25) gives an inaccurate constant distribution of the transverse shear stresses across the thickness. Enhanced values can be obtained by assuming a parabolic distribution of these stresses and computing their maximum value at  $z = 0$  from the shear forces using Eq.(5.27).

### 6.2.5 Virtual work principle

Let us consider a plate loaded by a vertical distributed loads  $\mathbf{t}$  and point loads  $\mathbf{p}_i$ . The virtual work expression is written as

$$\iiint_V \delta \boldsymbol{\varepsilon}^T \boldsymbol{\sigma} dV = \iint_A \delta \mathbf{u}^T \mathbf{t} dA + \sum_i \delta \mathbf{u}_i^T \mathbf{p}_i \quad (6.26a)$$

where

$$\delta \mathbf{u} = [\delta w, \delta \theta_x, \delta \theta_y]^T, \quad \mathbf{t} = [f_z, m_x, m_y]^T, \quad \mathbf{p}_i = [P_{z_i}, M_{x_i}, M_{y_i}]^T \quad (6.26b)$$

and  $\delta \mathbf{u}$  are the virtual displacement vector,  $\delta \boldsymbol{\varepsilon}$  is the virtual strain vector,  $f_z$ ,  $m_x$  and  $m_y$  are the vertical distributed load and the distributed moments acting on the  $xz$  and  $yz$  planes, respectively.  $P_{z_i}$ ,  $M_{x_i}$  and  $M_{y_i}$  are the vertical point load and the concentrated bending moments acting at a point  $i$ , respectively (Figure 5.1).

The virtual internal work over the plate domain can be expressed in terms of the middle plane variables (i.e. resultant stresses and generalized strains) using Eqs.(6.7) and (6.21) as follows

$$\iiint_V \delta \boldsymbol{\varepsilon}^T \boldsymbol{\sigma} dV = \iint_A \delta \hat{\boldsymbol{\varepsilon}}^T \left[ \int_{-t/2}^{t/2} \mathbf{S}^T \boldsymbol{\sigma} dz \right] dA = \iint_A \delta \hat{\boldsymbol{\varepsilon}}^T \hat{\boldsymbol{\sigma}} dA \quad (6.27)$$

The PVW is finally written in terms of integrals over the plate surface as

$$\iint_A \delta \hat{\boldsymbol{\varepsilon}}^T \hat{\boldsymbol{\sigma}} dA = \iint_A \delta \mathbf{u}^T \mathbf{t} dA + \sum_i \delta \mathbf{u}_i^T \mathbf{p}_i \quad (6.28a)$$

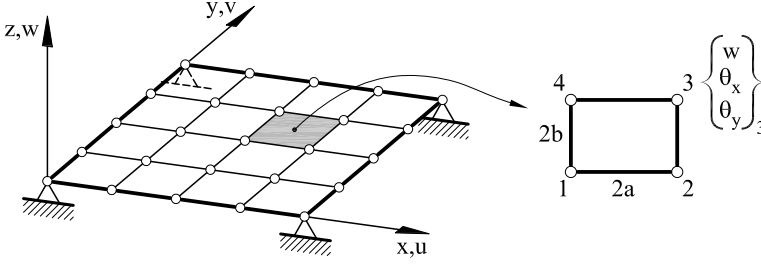


**Fig. 6.5** Discretization of a plate using 4-noded Reissner-Mindlin rectangles

Above integrals contain displacement derivatives up to first order only. This allows us to use  $C^0$  continuous elements which are simpler than Kirchhoff plate elements.

Sometimes it is interesting to split the virtual internal work in terms of the bending and transverse shear contributions using Eqs.(6.8) and (6.21). The PVW is then written as

$$\iint_A [\delta \hat{\boldsymbol{\varepsilon}}_b^T \hat{\boldsymbol{\sigma}}_b + \delta \hat{\boldsymbol{\varepsilon}}_s^T \hat{\boldsymbol{\sigma}}_s] dA = \iint_A \mathbf{u}^T \mathbf{t} dA + \sum_i \delta \mathbf{u}_i^T \mathbf{p}_i \quad (6.28b)$$

## 6.3 FINITE ELEMENT FORMULATION

### 6.3.1 Discretization of the displacement field

The plate middle plane is discretized into a mesh of  $n$  node elements; for instance Figure 6.5 shows a discretization in 4-noded plate rectangles. The deflection and the two rotations *are independent variables* and the displacement field is interpolated in the standard  $C^0$  form; i.e.

$$\begin{aligned} \mathbf{u} = \begin{Bmatrix} w \\ \theta_x \\ \theta_y \end{Bmatrix} &= \sum_{i=1}^n \begin{Bmatrix} N_i w_i \\ N_i \theta_{x_i} \\ N_i \theta_{y_i} \end{Bmatrix} = \begin{bmatrix} N_1 & 0 & 0 & \vdots & \vdots & N_n & 0 & 0 \\ 0 & N_1 & 0 & \vdots & \vdots & 0 & N_n & 0 \\ 0 & 0 & N_1 & \vdots & \vdots & 0 & 0 & N_n \end{bmatrix} \begin{Bmatrix} w_1 \\ \theta_{x_1} \\ \theta_{y_1} \\ \vdots \\ \vdots \\ w_n \\ \theta_{x_n} \\ \theta_{y_n} \end{Bmatrix} = \\ &= [\mathbf{N}_1, \mathbf{N}_2, \dots, \mathbf{N}_n] \begin{Bmatrix} \mathbf{a}_1^{(e)} \\ \vdots \\ \mathbf{a}_n^{(e)} \end{Bmatrix} = \mathbf{N} \mathbf{a}^{(e)} \end{aligned} \quad (6.29)$$

where

$$\mathbf{N} = [\mathbf{N}_1, \mathbf{N}_2, \dots, \mathbf{N}_n] \quad , \quad \mathbf{a}^{(e)} = \begin{Bmatrix} \mathbf{a}_1^{(e)} \\ \mathbf{a}_2^{(e)} \\ \vdots \\ \mathbf{a}_n^{(e)} \end{Bmatrix} \quad (6.30a)$$

and

$$\mathbf{N}_i = \begin{bmatrix} N_i & 0 & 0 \\ 0 & N_i & 0 \\ 0 & 0 & N_i \end{bmatrix} \quad , \quad \mathbf{a}_i^{(e)} = \begin{Bmatrix} w_i \\ \theta_{x_i} \\ \theta_{y_i} \end{Bmatrix} \quad (6.30b)$$

are the shape function matrix and the displacement vector for the element and a node  $i$ , respectively.

### 6.3.2 Discretization of the generalized strains and resultant stress fields

The generalized strains are expressed in terms of the nodal displacements (using Eqs.(6.8), (6.9) and (6.29)) as

$$\begin{aligned} \hat{\boldsymbol{\varepsilon}} = \begin{Bmatrix} \hat{\boldsymbol{\varepsilon}}_b \\ \dots \\ \hat{\boldsymbol{\varepsilon}}_s \end{Bmatrix} &= \begin{Bmatrix} \frac{\partial \theta_x}{\partial x} \\ \frac{\partial \theta_y}{\partial y} \\ \left( \frac{\partial \theta_x}{\partial y} + \frac{\partial \theta_y}{\partial x} \right) \\ \dots \\ \frac{\partial w}{\partial x} - \theta_x \\ \frac{\partial w}{\partial y} - \theta_y \end{Bmatrix} = \sum_{i=1}^n \begin{Bmatrix} \frac{\partial N_i}{\partial x} \theta_{x_i} \\ \frac{\partial N_i}{\partial y} \theta_{y_i} \\ \left( \frac{\partial N_i}{\partial y} \theta_{x_i} + \frac{\partial N_i}{\partial x} \theta_{y_i} \right) \\ \dots \\ \frac{\partial N_i}{\partial x} w_i - N_i \theta_{x_i} \\ \frac{\partial N_i}{\partial y} w_i - N_i \theta_{y_i} \end{Bmatrix} = \\ &= \sum_{i=1}^n \begin{Bmatrix} \mathbf{B}_{b_i} \\ \mathbf{B}_{s_i} \end{Bmatrix} \mathbf{a}_i^{(e)} = [\mathbf{B}_1, \dots, \mathbf{B}_n] \begin{Bmatrix} \mathbf{a}_1^{(e)} \\ \vdots \\ \mathbf{a}_n^{(e)} \end{Bmatrix} = \mathbf{B} \mathbf{a}^{(e)} \end{aligned} \quad (6.31)$$

where  $\mathbf{B}$  and  $\mathbf{B}_i$  are the generalized strain matrices for the element and a node  $i$ , respectively. From Eq.(6.31) we deduce

$$\mathbf{B}_i = \begin{Bmatrix} \mathbf{B}_{b_i} \\ \dots \\ \mathbf{B}_{s_i} \end{Bmatrix} \quad \text{with} \quad \mathbf{B}_{b_i} = \begin{bmatrix} 0 & \frac{\partial N_i}{\partial x} & 0 \\ 0 & 0 & \frac{\partial N_i}{\partial y} \\ 0 & \frac{\partial N_i}{\partial y} & \frac{\partial N_i}{\partial x} \end{bmatrix} \quad , \quad \mathbf{B}_{s_i} = \begin{bmatrix} \frac{\partial N_i}{\partial x} & -N_i & 0 \\ \frac{\partial N_i}{\partial y} & 0 & -N_i \end{bmatrix} \quad (6.32)$$

$\mathbf{B}_{b_i}$  and  $\mathbf{B}_{s_i}$  are the bending and transverse shear strain matrices associated to the  $i$ th node, respectively.

The resultant stresses are expressed in terms of the nodal displacements using Eqs.(6.22) and (6.31) as

$$\hat{\boldsymbol{\sigma}} = \hat{\mathbf{D}}\mathbf{B}\mathbf{a}^{(e)} \quad \text{and} \quad \hat{\boldsymbol{\sigma}}_b = \hat{\mathbf{D}}_b\mathbf{B}_b\mathbf{a}^{(e)} \quad , \quad \hat{\boldsymbol{\sigma}}_s = \hat{\mathbf{D}}_s\mathbf{B}_s\mathbf{a}^{(e)} \quad (6.33a)$$

with

$$\mathbf{B}_b = [\mathbf{B}_{b_1}, \mathbf{B}_{b_2}, \dots, \mathbf{B}_{b_n}] \quad , \quad \mathbf{B}_s = [\mathbf{B}_{s_1}, \mathbf{B}_{s_2}, \dots, \mathbf{B}_{s_n}] \quad (6.33b)$$

### 6.3.3 Derivation of the equilibrium equations for the element

The PVW for a single element under distributed loads reads (Eq.(6.28a))

$$\iint_{A^{(e)}} \delta \hat{\boldsymbol{\varepsilon}}^T \hat{\boldsymbol{\sigma}} dA = \iint_{A^{(e)}} \delta \mathbf{u}^T \mathbf{t} dA + [\delta \mathbf{a}^{(e)}]^T \mathbf{q}^{(e)} \quad (6.34)$$

where, as usual,  $\delta \mathbf{a}^{(e)}$  is the virtual nodal displacement vector and the last term of the r.h.s. is the virtual work of the equilibrating nodal forces  $\mathbf{q}^{(e)}$ , with

$$\delta \mathbf{a}^{(e)} = \begin{Bmatrix} \delta \mathbf{a}_1^{(e)} \\ \vdots \\ \delta \mathbf{a}_n^{(e)} \end{Bmatrix} , \quad \delta \mathbf{a}_i^{(e)} = \begin{Bmatrix} \delta w_i \\ \delta \theta_{x_i} \\ \delta \theta_{y_i} \end{Bmatrix} , \quad \mathbf{q}^{(e)} = \begin{Bmatrix} \mathbf{q}_1^{(e)} \\ \vdots \\ \mathbf{q}_n^{(e)} \end{Bmatrix} , \quad \mathbf{q}_i^{(e)} = \begin{Bmatrix} F_{z_i} \\ \mathcal{M}_{x_i} \\ \mathcal{M}_{y_i} \end{Bmatrix} \quad (6.35)$$

Substituting Eq.(6.33a) into (6.34) and using Eqs.(6.29) and (6.31) yields the standard discrete equilibrium expression for the element

$$\mathbf{K}^{(e)} \mathbf{a}^{(e)} - \mathbf{f}^{(e)} = \mathbf{q}^{(e)} \quad (6.36)$$

where

$$\mathbf{K}_{ij}^{(e)} = \iint_{A^{(e)}} \mathbf{B}_i^T \hat{\mathbf{D}} \mathbf{B}_j dA \quad (6.37)$$

$$\mathbf{f}_i^{(e)} = \iint_{A^{(e)}} \mathbf{N}_i [f_z, m_x, m_y]^T dA \quad (6.38)$$

are the element stiffness matrix connecting nodes  $i$  and  $j$  and the equivalent nodal force vector due to a distributed vertical load  $f_z$  and distributed bending moments  $m_x$  and  $m_y$ .

The global system of equations  $\mathbf{K}\mathbf{a} = \mathbf{f}$  is obtained by assembling the element contributions to the global stiffness matrix  $\mathbf{K}$  and the global equivalent nodal force vector  $\mathbf{f}$  in the usual manner.

The element stiffness matrix can be split into the bending and transverse shear contributions using Eqs.(6.23) and (6.32) as follows.

$$\begin{aligned} \mathbf{K}_{ij}^{(e)} &= \iint_{A^{(e)}} [\mathbf{B}_{b_i}^T, \mathbf{B}_{s_i}^T]^T \hat{\mathbf{D}} \begin{Bmatrix} \mathbf{B}_{b_j} \\ \mathbf{B}_{s_j} \end{Bmatrix} dA = \\ &= \iint_{A^{(e)}} \left( \mathbf{B}_{b_i}^T \hat{\mathbf{D}}_b \mathbf{B}_{b_j} + \mathbf{B}_{s_i}^T \hat{\mathbf{D}}_s \mathbf{B}_{s_j} \right) dA = \mathbf{K}_{bij}^{(e)} + \mathbf{K}_{sij}^{(e)} \end{aligned} \quad (6.39a)$$

where

$$\mathbf{K}_{bij}^{(e)} = \iint_{A^{(e)}} \mathbf{B}_{b_i}^T \hat{\mathbf{D}}_b \mathbf{B}_{b_j} dA \quad ; \quad \mathbf{K}_{sij}^{(e)} = \iint_{A^{(e)}} \mathbf{B}_{s_i}^T \hat{\mathbf{D}}_s \mathbf{B}_{s_j} dA \quad (6.39b)$$

Above splitting provides a more economical way for computing the element stiffness matrix. It also helps explaining the behaviour of the element for thin plate situations.

Differently to Kirchhoff plate elements, vertical loads and bending moments contribute to the terms of  $\mathbf{f}_i^{(e)}$  in an uncoupled manner, i.e. vertical loads do not introduce bending moment components in  $\mathbf{f}_i^{(e)}$ . This is due to the independent interpolation for the deflection and the rotations.

Self-weight is treated as a vertical distributed loading. For the gravity  $g$  acting in opposite direction to the global  $z$  axis,  $f_z = -\rho g t$  and

$$\mathbf{f}_i^{(e)} = - \iint_{A^{(e)}} \mathbf{N}_i \rho g t [1, 0, 0]^T dA \quad (6.40a)$$

where  $\rho$  and  $t$  are the material density and the plate thickness, respectively. Finally, the equivalent nodal force vector due to an external vertical point load  $P_{z_j}$  and concentrated bending moments  $M_{x_j}, M_{y_j}$  acting at a node with global number  $j$  is

$$\mathbf{p}_j = [P_{z_j}, M_{x_j}, M_{y_j}]^T \quad (6.40b)$$

As usual concentrated forces acting at nodes are assembled directly into the global vector  $\mathbf{f}$ .

The reactions at the prescribed nodes are computed a posteriori once the nodal displacements have been found as explained in Section 1.3.4.

### 6.3.4 Numerical integration

The integrals appearing in the element stiffness matrix and the equivalent nodal force vector are typically computed by a Gauss quadrature.

From Eq.(6.39a) we deduce

$$\mathbf{K}_{ij}^{(e)} = \sum_{p=1}^{n_{bp}} \sum_{q=1}^{n_{bq}} \left[ \mathbf{B}_{bi}^T \hat{\mathbf{D}}_b \mathbf{B}_{bj} |\mathbf{J}^e| \right]_{p,q} W_p W_q + \sum_{p=1}^{n_{sp}} \sum_{q=1}^{n_{sq}} \left[ \mathbf{B}_{si}^T \hat{\mathbf{D}}_s \mathbf{B}_{sj} |\mathbf{J}^e| \right]_{p,q} W_p W_q \quad (6.41)$$

where  $|\mathbf{J}^e|$  is the Jacobian determinant [On4],  $(n_{bp}, n_{bq})$  and  $(n_{sp}, n_{sq})$  are the integration points for the bending and transverse shear stiffness matrices, respectively and  $W_p, W_q$  are the corresponding weights. Eq.(6.11) allows us to use a selective integration rule for the bending and transverse shear stiffness matrices.

The Gauss quadrature for the equivalent nodal force vector of Eq.(6.38) is

$$\mathbf{f}_i^{(e)} = \sum_{p=1}^{n_p} \sum_{q=1}^{n_q} \left[ N_i [f_z, m_x, m_y]^T |\mathbf{J}^e| \right]_{p,q} W_p W_q \quad (6.42)$$

### 6.3.5 The boundary conditions

The standard boundary conditions are:

*Point support:*  $w_i = 0$

*Symmetry axis (of geometry and loading):*  $\theta_n = 0$ , where  $n$  is the orthogonal direction to the symmetry axis.

*Clamped (CL) side:*  $w = \theta_x = \theta_y = 0$

*Simply supported (SS) side:*

- Hard support:  $w = \theta_s = 0$
- Soft support:  $w = 0$

where  $s$  is the direction of the side. Recall that in Kirchhoff theory constraining of  $w$  along a direction  $s$  automatically specifies  $\theta_s = 0$  (Section 5.2.7). This is not the case for Reissner–Mindlin theory where both  $w$  and  $\theta_s$  have to be independently prescribed.

Figure 6.6 shows graphically the different boundary conditions. A free edge requires no specific constraint, as usual.

In plates with corners, the soft support condition introduces a boundary layer of order  $t$  adjacent to the prescribed side for the resultant stresses  $Q_s$ ,  $Q_n$  and  $M_{ns}$  where  $n$  is the orthogonal direction to the side. The hard

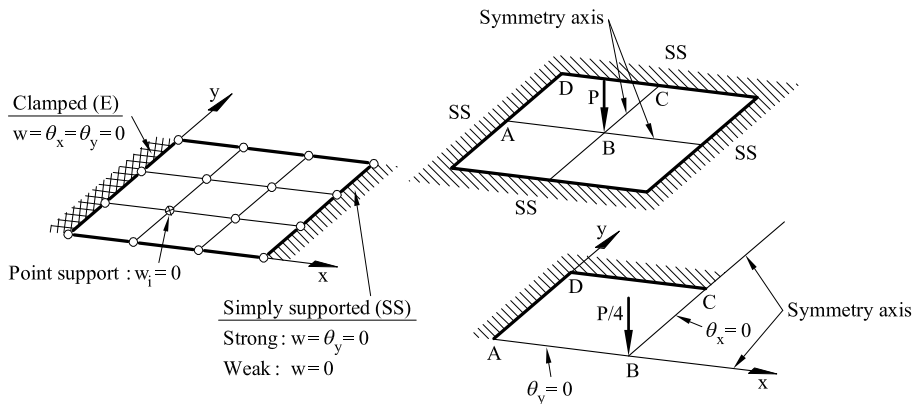


Fig. 6.6 Some boundary conditions in Reissner-Mindlin plates

a) SS (hard support)                      b) SS (soft support)

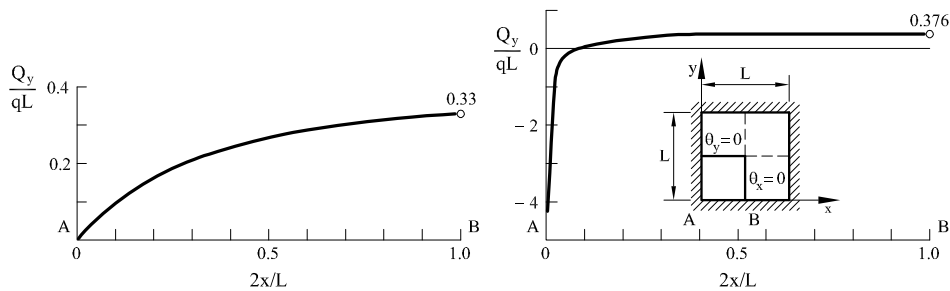
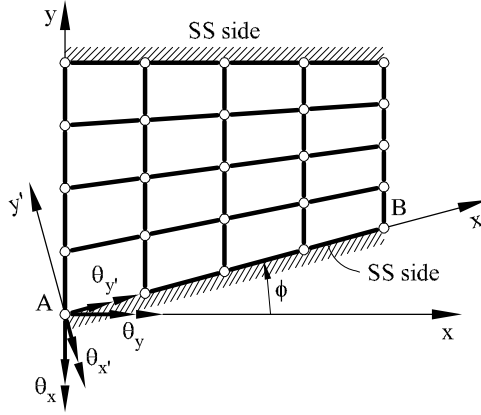


Fig. 6.7 Simply supported (SS) square plate under uniform distributed loading  $q$ . Distribution of shear force  $Q_y$  along the support line  $AB$  for hard support (a) and soft support (b) conditions. Solution obtained with an adapted mesh of  $10 \times 10$  QLQL elements in a quarter of the plate and  $t/L = 0.02$

support condition is recommended in those cases, as capturing the boundary layer requires a very fine discretization near the side. Figure 6.7 shows a situation of this kind for a simply supported square plate under uniformly distributed loading ( $f_z = q$ ) and  $\frac{t}{L} = 0.02$ . The distribution of the shear force  $Q_y$  along the support line  $AB$  is plotted for the hard support ( $w = \theta_x = 0$ ) and soft support ( $w = 0$ ) conditions. Note the strong variation of  $Q_y$  in the vicinity of the corner  $A$  for the soft support assumption whereas the value at the center is quite insensible to the boundary conditions chosen. The analysis was performed with a mesh of  $10 \times 10$  QLQL elements in a quarter of plate due to symmetry (Section 6.7.4). The mesh





**Fig. 6.8** Boundary conditions in a plate with inclined simply supported (SS) side

density was higher near the plate edges in order to capture the boundary layer [BD5].

The condition  $\theta_s = 0$  along an inclined axis requires transforming the cartesian rotations to the boundary axes.

For instance, the boundary conditions on the simply supported inclined side  $AB$  in the plate of Figure 6.8 are  $w' = \theta_{x'} = 0$  (note the definition of the rotation vectors in the figure). The displacement transformation for all nodes belonging to the inclined boundary line  $AB$  is written as

$$\mathbf{a}_i^{(e)} = [w_i, \theta_{x_i}, \theta_{y_i}]^T = \mathbf{L}_i [w_i, \theta_{x'_i}, \theta_{y'_i}]^T = \mathbf{L}_i \mathbf{a}'_i^{(e)} \quad (6.43a)$$

where

$$\mathbf{L}_i = \begin{bmatrix} 1 & 0 & 0 \\ 0 & \cos \phi_i & -\sin \phi_i \\ 0 & \sin \phi_i & \cos \phi_i \end{bmatrix} \quad (6.43b)$$

Clearly in the plate of Figure 6.8  $\phi_i = \phi$  for all nodes on the boundary  $AB$ .

The stiffness matrix of the element adjacent to the boundary line  $AB$  is transformed as (Section 9.2 of [On4])

$$\bar{\mathbf{K}}_{ij} = \hat{\mathbf{L}}_i^T \mathbf{K}_{ij} \hat{\mathbf{L}}_j \quad (6.44)$$

with

$$\hat{\mathbf{L}}_i = \begin{cases} \mathbf{L}_i, & \text{if node } i \text{ lays on the inclined boundary} \\ \mathbf{I}_3, & \text{if node } i \text{ belongs to the interior domain} \end{cases}$$

where  $\mathbf{I}_3$  is the  $3 \times 3$  unit matrix.

## 6.4 PERFORMANCE OF REISSNER-MINDLIN PLATE ELEMENTS FOR THIN PLATE ANALYSIS

### 6.4.1 Locking. Reduced integration. Constraint index

Reissner-Mindlin plate elements suffer from the same drawbacks as Timoshenko beam elements, i.e. the numerical solution “locks” for thin plate situations.

This defect can be observed following the same procedure as for beams (Section 2.5). Let us consider an isotropic plate of constant thickness under nodal point loads. The global equilibrium equations are written as

$$(\mathbf{K}_b + \mathbf{K}_s)\mathbf{a} = \mathbf{f} \quad (6.45)$$

where  $\mathbf{K}_b$  and  $\mathbf{K}_s$  assemble the individual bending and shear stiffness contributions for each element. Since the material properties and the thickness are constant we can rewrite Eq.(6.45) as

$$\left( \frac{Et^3}{12(1-\nu^2)} \bar{\mathbf{K}}_b + Gt \bar{\mathbf{K}}_s \right) \mathbf{a} = \mathbf{f} \quad (6.46)$$

The “exact” thin Kirchhoff plate solution, termed hereafter  $\mathbf{a}_k$ , is inversely proportional to  $\frac{Et^3}{12(1-\nu^2)}$  [TW]. Dividing Eq.(6.46) by this expression gives

$$\left( \bar{\mathbf{K}}_b + \frac{1}{\beta} \bar{\mathbf{K}}_s \right) \mathbf{a} = \frac{12(1-\nu^2)}{Et^3} \mathbf{f} = O(\mathbf{a}_k) \quad (6.47a)$$

with

$$\beta = \frac{Et^2}{12(1-\nu^2)G} \quad (6.47b)$$

The r.h.s. of Eq.(6.47a) is *of the order of magnitude* of the exact thin plate solution. Clearly, as  $t \rightarrow 0$ , then  $\beta \rightarrow 0$  and  $\frac{1}{\beta} \rightarrow \infty$ , i.e. the transverse shear terms in Eq.(6.47a) dominate the solution as the plate is thinner. The influence of the bending terms is negligible for very thin plates and Eq.(6.47a) tends to

$$\frac{1}{\beta} \bar{\mathbf{K}}_s \mathbf{a} = O(\mathbf{a}_k) \quad \text{and} \quad \bar{\mathbf{K}}_s \mathbf{a} = \beta O(\mathbf{a}_k) \rightarrow \mathbf{0} \quad (6.48)$$

Hence, for very thin plates the solution is infinitely stiffer than the “exact” thin plate solution. From Eq.(6.48) we deduce that the only possibility for obtaining a solution different from  $\mathbf{a} = 0$  is that  $\mathbf{K}_s$  be singular.

Singularity of  $\mathbf{K}_s$  can be achieved by reduced integration, similarly as for Timoshenko beam elements [ZT2,ZTZ]. Eq.(2.50) can be used to check the singularity of  $\mathbf{K}_s$  for each mesh “a priori”.

To clarify concepts the following terminology will be used hereonwards:

*Full integration:* exact integration for  $\mathbf{K}_b^{(e)}$  and  $\mathbf{K}_s^{(e)}$

*Selective integration:* exact integration for  $\mathbf{K}_b^{(e)}$  and reduced integration for  $\mathbf{K}_s^{(e)}$

*Reduced integration:* reduced integration for both  $\mathbf{K}_b^{(e)}$  and  $\mathbf{K}_s^{(e)}$

Exact integration is only possible for simple geometrical element shapes, i.e. rectangles or straight-sided triangles, as for 2D solid elements. The term full integration hereonwards therefore refers to the Gauss quadrature that yields an exact integration for the element in its rectangular or straight-sided triangular form [On4].

The singularity of  $\mathbf{K}_s$  can be anticipated by evaluating the *constraint index* (CI) of each element. The CI is obtained by applying Eq.(2.50) for a single quadrilateral plate element with two adjacent edges clamped and the other two edges free. This gives (for  $s = 2$ )

$$\text{CI} = \text{Free DOFs} - 2 * \text{NGP} \quad (6.49)$$

where NGP is the number of Gauss points chosen for integrating  $\mathbf{K}_s^{(e)}$ .

Values of  $\text{CI} \geq 4$  ensure the singularity of  $\mathbf{K}_s$  for any mesh [BD5,ZT]. Values of  $\text{CI} < 0$  indicate that  $\mathbf{K}_s^{(e)}$  is not singular and invalidate the element. A value of CI close to zero indicates that the element is not reliable and that some situations where singularity is not satisfied can be found (leading to locking). Figure 6.9 shows the CI for some plate elements. The CI is the same for reduced and selective integration as it only depends on the quadrature for  $\mathbf{K}_s^{(e)}$ .

Alternative indexes based on the rank of  $\mathbf{K}_s^{(e)}$  for assessing the tendency of the element to lock have been proposed [BD5]. The same conclusions regarding the merits using a reduced quadrature for  $\mathbf{K}_s^{(e)}$  were found.

## 6.4.2 Mechanisms induced by reduced integration

An element has a mechanism when it can adopt a deformed shape compatible with the boundary conditions, without consuming internal work (strain energy). For this reason mechanisms are also called zero energy

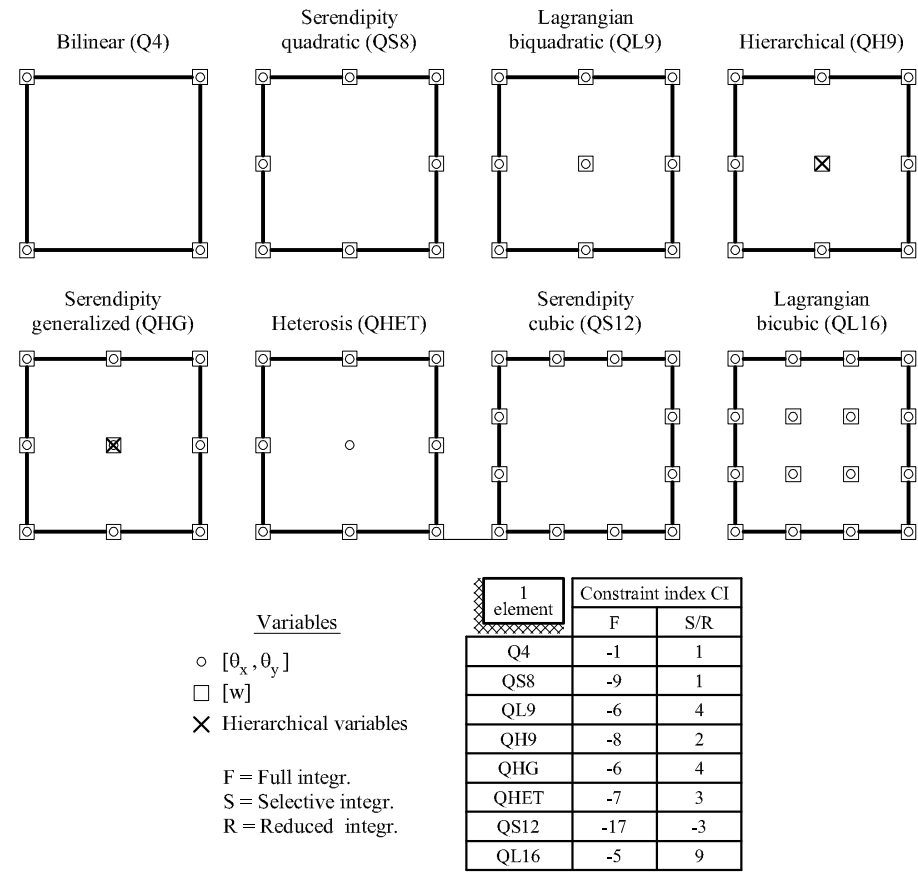


**Fig. 6.9** Some Reissner-Mindlin plate quadrilaterals. Constraint index (CI) for full (F), selective (S) and reduced (R) integration

modes. An individual element, free of external constraints, has the standard rigid body mechanisms of translation and rotation which disappear by prescribing the boundary conditions. Thus, a beam element has two mechanisms (the vertical deflection and the rotation) which vanish when the beam is simply supported at two points, or clamped at one end. Similarly, a plate element has three mechanisms: the deflection and two rotations. (Figure 6.10). These mechanisms can be identified by computing the zero eigenvalues of the stiffness matrix for an unconstrained element [CMPW,Cr,ZT2]. Each zero eigenvalue corresponds to a mechanism whose shape is given by the corresponding eigenmode. This procedure can be applied to any element assembly.

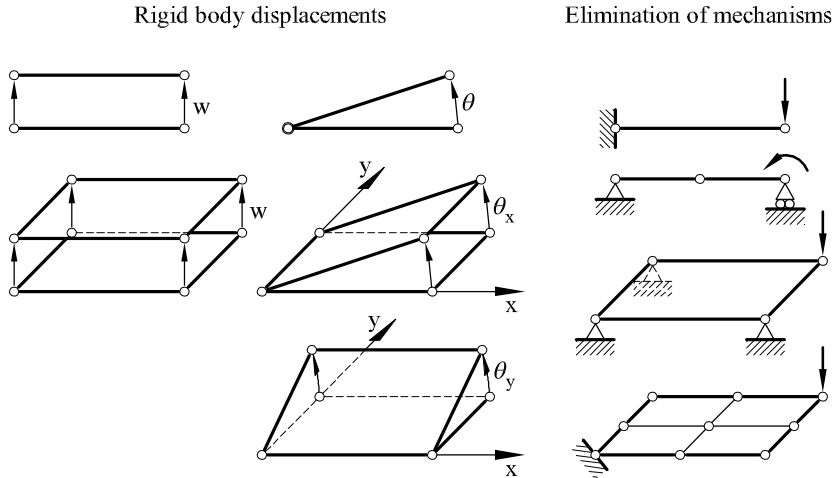


**Fig. 6.10** Rigid body mechanisms for beam and plate elements

Reduced integration can induce additional zero eigenvalues in the element stiffness matrix and hence originate new mechanisms in addition to the rigid body motions. These new mechanisms can or can not propagate themselves within a mesh. This depends on their compatibility with adjacent elements and with the boundary conditions. Consequently, the singularity of  $\mathbf{K}_s^{(e)}$  must always be verified together with the existence of spurious mechanisms in the global element stiffness matrix  $\mathbf{K}^{(e)}$  and on their capacity to propagate within a mesh.

### 6.4.3 Requirements for the ideal plate element

On the basis of the preceedings arguments the ideal plate element should fulfil the following requirements:

- It should be applicable to both thick and thin situations.
- It should not have other mechanisms than the standard rigid body modes.
- It should satisfy the usual invariance and convergence conditions.
- It should give accurate solutions for the deflection, the rotations, the bending moments and the shear forces.
- It should be insensitive to geometry distortions.
- Its formulation should not be based on user's dependent adjustment parameters.
- It should be easy to implement and use in a computer program.

The more popular Reissner–Mindlin plate elements satisfying most of these conditions are presented in the next sections. In order to facilitate their study, the elements have been classified in three groups: i) those based on *selective/reduced integration* techniques, ii) those based on *assumed transverse shear strain fields*, and iii) those based on *linked interpolations*. Recent research experiences favour the second, and to some extent the third, approaches. However, didactic and historical reasons justify the overview of the elements based on selective and reduced quadratures which have enjoyed popularity in last decades.

## 6.5 REISSNER-MINDLIN PLATE QUADRILATERALS BASED ON SELECTIVE/REDUCED INTEGRATION

All elements presented in this section are based on the strict application of the concepts explained in Section 6.4.1, i.e. the singularity of matrix  $\mathbf{K}_s^{(e)}$  is sought by using a lower order quadrature.

### 6.5.1 Four-noded plate quadrilateral (Q4)

The bilinear 4-noded plate quadrilateral was initially developed using selective integration by Hughes *et al.* [HTK] and Pugh *et al.* [PHZ]. This element is contemporary of the 8 and 9-noded elements of next sections.

The Q4 element has the standard bilinear shape functions of the 4-noded quadrilateral (Section 4.4.1 of [On4]). Full integration for rectangular shapes requires a  $2 \times 2$  Gauss quadrature for  $\mathbf{K}_b^{(e)}$  and  $\mathbf{K}_s^{(e)}$  (Table 6.1). Figure 6.9 shows that the CI is negative in this case. The one point quadrature for  $\mathbf{K}_s^{(e)}$  makes this matrix singular and gives  $\text{CI} = 1$ , far from the optimum value of  $\text{CI} \geq 4$ . The quadratures shown in Table 6.1 are applicable for both rectangular and quadrilateral shapes.

Reduced integration leads to seven zero energy modes (Table 6.2). After subtracting the three rigid body modes the element still has the four spurious mechanisms shown in Figure 6.11 which invalidate the quadrature. Belytschko *et al.* [BT,BTL] derived a procedure to stabilize these mechanisms. This allows using the Q4 element with the simple one point reduced quadrature.

Selective integration (Table 6.1) brings down the number of spurious mechanisms to the first two of Figure 6.11. The second one can not propagate in a mesh, but the first one can lead to problems. An example is a square plate simply supported at the four corners where the stiffness

Element	Quadrature	Quadrature for integration of	
		$\mathbf{K}_b^{(e)}$	$\mathbf{K}_s^{(e)}$
Q4	F	$2 \times 2$	$2 \times 2$
	S	$2 \times 2$	$1 \times 1$
	R	$1 \times 1$	$1 \times 1$
QS8,QL9	F	$3 \times 3$	$3 \times 3$
QH9,QHG	S	$3 \times 3$	$2 \times 2$
QHET	R	$2 \times 2$	$2 \times 2$
QS12, QL16	F	$4 \times 4$	$4 \times 4$
	S	$4 \times 4$	$3 \times 3$
	R	$3 \times 3$	$3 \times 3$

**Table 6.1** Full (F), selective (S) and reduced (R) quadratures for various Reissner-Mindlin plate quadrilaterals

Element	Number of zero eigenvalues (mechanisms) for $\mathbf{K}^{(e)}$ in an isolated element		
	Full integration	Selective integration	Reduced integration
Q4	3 (0)	5 (2)	7 (4)
QS8	3 (0)	3 (0)	4 (1)
QL9	3 (0)	4 (1)	7 (4)
QH9,QHG	3 (0)	3 (0)	4 (1)
QHET	3 (0)	3 (0)	6 (3)
QS12	3 (0)	3 (0)	3 (0)
QL16	3 (0)	4 (1)	7 (4)

**Table 6.2** Mechanisms in quadrilateral Reissner-Mindlin plate elements induced by different quadratures. Numbers within brackets denote the number of spurious mechanisms

matrix is singular. These mechanisms can be stabilized, yielding a safe element [BT,BTL]. The element performs well with selective integration for a clamped plate, as shown in [Figure 6.10](#).

The resultant stresses must be computed at the  $2 \times 2$  Gauss points, while the central point is optimal for evaluating the shear forces [HTK].

McNeal [Ma2] proposed an interesting version of this element using a modified shear modulus similarly as done for Timoshenko beams in Section 2.6. This idea was applied to higher order plate elements by Tessler and Hughes [TH] (Section 6.7.6).

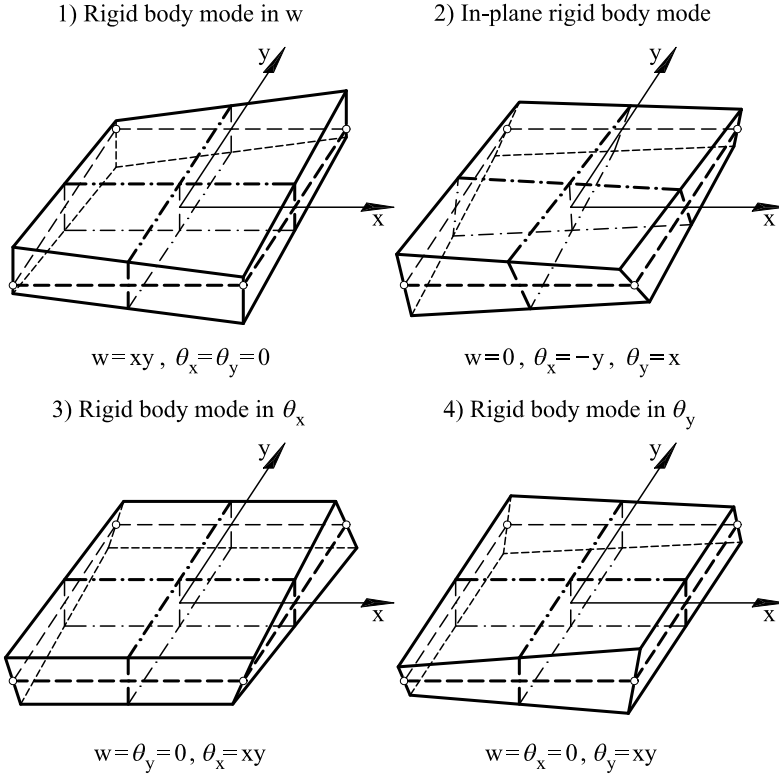


**Fig. 6.11** Q4 plate element. Spurious mechanisms induced by reduced (1-4) and selective (1 and 2) integration

### 6.5.2 Eight-noded Serendipity plate quadrilateral (QS8)

The QS8 8-noded Serendipity Reissner-Mindlin plate quadrilateral (Figure 6.9) has an irregular behaviour for thick and thin plates. Full integration requires a  $3 \times 3$  Gauss quadrature for both  $\mathbf{K}_b^{(e)}$  and  $\mathbf{K}_s^{(e)}$  (Table 6.1) and CI is negative in this case. The  $2 \times 2$  reduced quadrature for  $\mathbf{K}_s^{(e)}$  gives an insufficient value of  $\text{CI} = 1$  (Figure 6.9).

Reduced integration introduces a spurious zero eigenvalue in  $\mathbf{K}^{(e)}$  (Table 6.2). The associated mechanism *can not propagate* in a mesh and the element is “safe” for practical purposes. Unfortunately, reduced integration does not suffice to ensure the singularity of  $\mathbf{K}_s^{(e)}$  and the element locks for some problems. An example is the clamped plate of Figure 6.12.

In conclusion, the QS8 plate element should be used with precaution. It is free from spurious mechanisms and performs well for thick and moder-



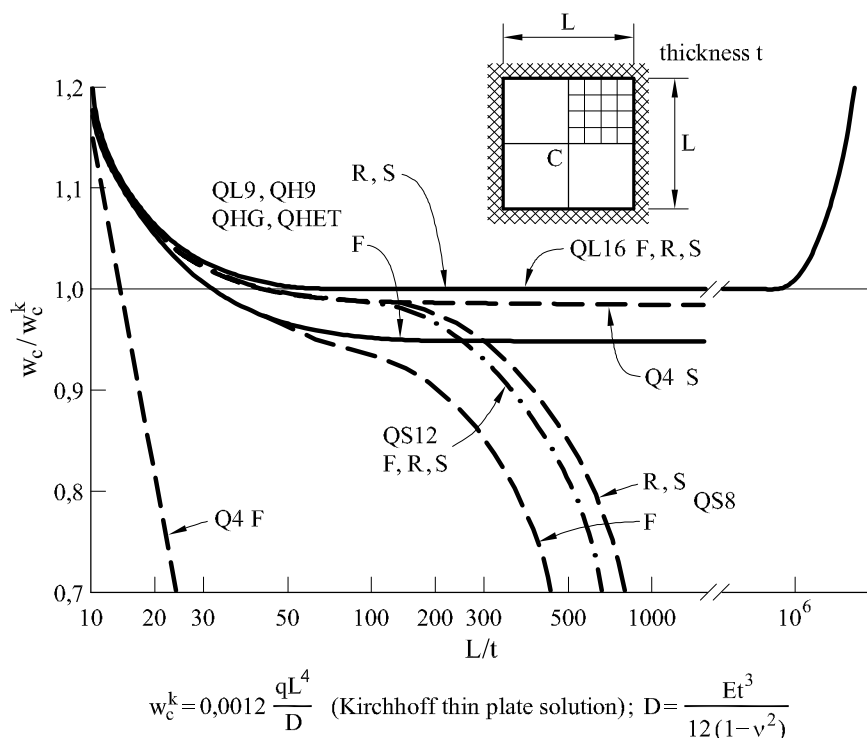


**Fig. 6.12** Clamped square plate under uniform load. Central deflection versus  $L/t$  for different quadrilateral elements: Bilinear (Q4), Serendipity quadratic and cubic (QS8 and QS12), Lagrangian biquadratic and cubic (QL9 and QL16), Heterosis (QHET) and Hierarchical (QH9, QHG) with full (F), selective (S) and reduced (R) integration. A quarter of the plate is analyzed with a  $4 \times 4$  mesh due to symmetry

ately thin plates. Its behaviour for very thin plates depends on the boundary conditions.

### 6.5.3 Nine-noded Lagrange plate quadrilateral (QL9)

The QL9 9-noded Lagrange plate quadrilateral (Figure 6.9) has an opposite behaviour to the QS8 element. A  $3 \times 3$  full integration yields a negative CI. The  $2 \times 2$  reduced quadrature for  $\mathbf{K}_s^{(e)}$  raises the CI to 4, thus anticipating a good behaviour for thin situations (Figure 6.9). This is shown in the clamped plate of Figure 6.12 where excellent results are obtained for a wide range of thicknesses. The solution deteriorates for  $\frac{L}{t} \geq 10^6$  due to round-off errors when solving the equations. This deficiency can be avoided by using a fictitious thickness when computing  $\mathbf{K}_s^{(e)}$

such that  $(\frac{L}{t})^2 \geq 10^{p/2}$ , where  $p$  is the number of decimal digits which the computer can store, while the bending stiffness is computed with the correct thickness. In this manner, the shear strain is computed incorrectly when its effect is so small that it does not influence the numerical solution [CMPW,Fr,Fr2,HTK].

Reduced integration excites four spurious mechanisms (Table 6.2), while selective integration induces just one mechanism. This mechanism can propagate in a mesh for some boundary conditions and thus the element is not reliable. Figure 6.13 shows an example of two square plates under a corner point load with the minimum boundary constraints to avoid rigid body movements. The QL9 element with reduced integration yields such poor results that can not even be graphically plotted. Selective integration induces an oscillatory solution due to the propagable mechanism (Figure 6.13b). The QS8 element yields the correct solution (for moderate thickness), as well as the 9-noded Hierarchical and Heterosis quadrilaterals presented in the next sections.

#### 6.5.4 Nine-noded hierarchical plate quadrilateral (QH9)

The behaviour of the QS8 and QL9 quadrilaterals evidences the need for an element which incorporates their best features, i.e. a plate quadrilateral free of spurious mechanisms and valid for all range of thicknesses.

Cook [CPMW] modified the QS8 element by adding a central node with a bubble function for the deflection only (Figure 6.9). The displacement field is defined as

$$\theta_x = \sum_{i=1}^8 N_i \theta_{x_i}, \quad \theta_y = \sum_{i=1}^8 N_i \theta_{y_i} \quad (6.50a)$$

$$w = \left( \sum_{i=1}^8 N_i w_i \right) + \bar{N}_9 \bar{w}_9 \quad (6.50b)$$

where  $N_i$  are the standard shape functions for the QS8 element and  $\bar{N}_9 = (1 - \xi^2)(1 - \eta^2)$ . The hierarchical variable  $\bar{w}_9$  is the difference between the nodal deflections obtained with the QS8 and QL9 elements. For the isoparametric description the  $N_i$  shape functions are used.

Reduced integration (Table 6.1) gives  $CI = 2$ , which places the element at an intermediate position between the QS8 and QL9. Reduced integration excites one spurious mechanism (Table 6.2). The mechanism can be eliminated by multiplying the diagonal stiffness coefficient corresponding

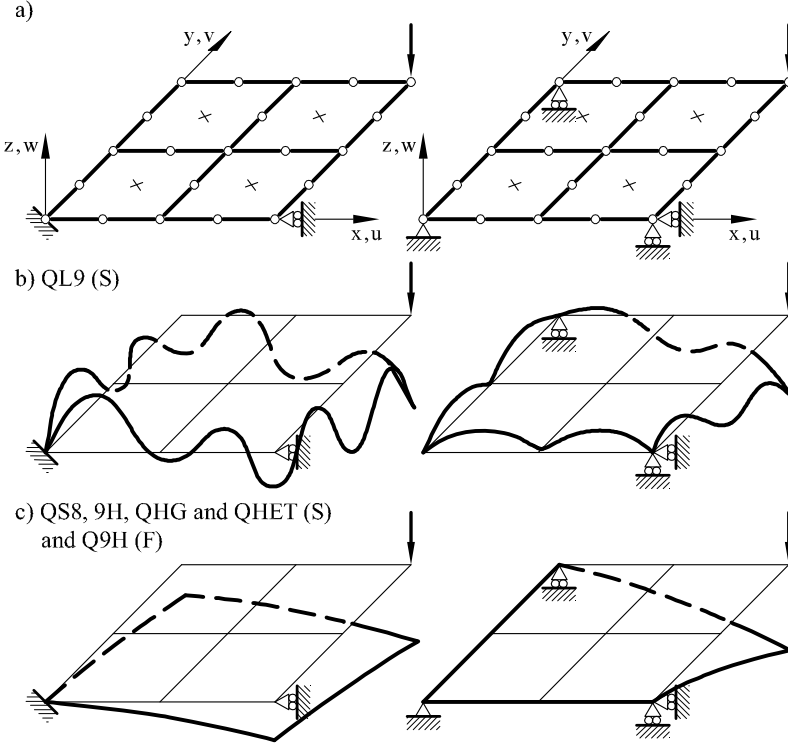


**Fig. 6.13** Analysis of two square plates under corner point load with minimum boundary constraints: (a) Geometry, b.c. and loading. (b) and (c) Deformed shapes obtained using QL9, QS8, QH9, QHG and QHET elements with full (F) and selective (S) integration

to  $\bar{w}_9$  by  $(1+e)$  where  $e$  is a small number ( $e = 10^{-2}t/L$  is recommended). This is equivalent to adding a small “spring” to the hierarchical node. Selective integration eliminates the internal mechanism (Table 6.2) and leads to good results for thick and thin plates (Figures 6.12 and 6.13).

### 6.5.5 A generalization of the 9-noded hierarchical plate quadrilateral (QH9)

Oñate *et al.* [OHG] generalized and improved the QH9 element by including the two rotations as hierarchical variables. The displacement field is

$$\begin{Bmatrix} w \\ \theta_x \\ \theta_y \end{Bmatrix} = \left( \sum_{i=1}^8 N_i \begin{Bmatrix} w_i \\ \theta_{x_i} \\ \theta_{y_i} \end{Bmatrix} \right) + \bar{N}_9 \begin{Bmatrix} \bar{w}_9 \\ \theta_{x_9} \\ \theta_{y_9} \end{Bmatrix} \quad (6.51)$$

where  $N_i$  and  $\bar{N}_9$  have the same meaning as in Eq.(6.50).

This allows us to retain three variables per node. Also, the value of CI with the reduced  $2 \times 2$  quadrature increases to 4 (Figure 6.9).

The diagonal coefficients of  $\mathbf{K}^{(e)}$  corresponding to the three hierarchical variables are multiplied by  $(1 + e_1)$ ,  $(1 + e_2)$  and  $(1 + e_3)$ , respectively. By choosing  $e_1 = e_2 = e_3 = 0$  the element performs as the QL9 one. Making  $e_1$ ,  $e_2$  and  $e_3$  very large is equivalent to eliminating the hierarchical variables and the behaviour of the QS8 element is reproduced. Finally, making  $e_1$  and  $e_2$  very large reproduces the QH9 element.

Reduced integration introduces one spurious mechanism (Table 6.2). This can be eliminated by adjusting the spring parameters ( $e_1 = e_2 = e_3 = 0.004$  is recommended in [OHG]) or by selective integration. Figures 6.12 and 6.13 show the good behaviour of the QHG element with selective integration.

The choice of different spring parameters for the hierarchical variables allows us to derive plate elements with features laying between the QS8 and QL9. An example is the element presented in the next section.

### 6.5.6 Nine-noded heterosis plate quadrilateral (QHET)

Hughes and Cohen [HC] proposed a 9-noded plate quadrilateral termed Heterosis (hybrid which inherits the best properties of its parents) with the following interpolation

$$\theta_x = \sum_{i=1}^9 N_i^L \theta_{x_i}; \quad \theta_y = \sum_{i=1}^9 N_i^L \theta_{y_i} \quad y \quad w = \sum_{i=1}^8 N_i^S w_i \quad (6.52)$$

where  $N_i^L$  and  $N_i^S$  are the shape functions of the 9-noded Lagrangian and the 8-noded Serendipity quadrilaterals, respectively (Appendix I). The Serendipity shape functions are used to interpolate the element geometry.

The element (termed here QHET) has an acceptable value of CI = 3 (Figure 6.9). Selective integration eliminates the spurious mechanism typical of the QL9 element (Table 6.2). This preserves the good performance for thin plate analysis as shown in Figures 6.12 and 6.13.

The QHET element is a particular case of the QHG of previous section by making  $e_1 = e_2 = 0$  and  $e_3$  equal to a large number [OHG].

An inconvenient of the QHET element is that, similarly as for the QH9, it has a different number of DOFs at the central node. Also it does not satisfy the patch test for irregular shapes [Cr].

### 6.5.7 Higher order Reissner–Mindlin plate quadrilaterals with 12 and 16 nodes

Higher order Serendipity and Lagrange Reissner–Mindlin plate quadrilaterals present a behaviour analogous to the QS8 and QL9 ones. We consider here the cubic 12-noded Serendipity (QS12) and the 16-noded Lagrange (QL16) quadrilaterals (Figure 6.9 and Table 6.1). Selective integration for the QS12 element eliminates all spurious mechanisms, similarly as for the QS8 one (Table 6.2). However, its behaviour for thin plate analysis is poor as indicated by the negative value of  $CI = -3$  (Figure 6.9). The QL16 element has  $CI = 9$  with reduced and selective integration and it behaves well for thin plates. Unfortunately, both quadratures induce a spurious mechanism, similarly as for the Q9L element (Table 6.2). Figure 6.12 shows the performance of the QS12 and QL16 elements for a clamped plate under uniform loading. The merit of selective/reduced integration versus the full quadrature is not relevant for these elements [PHZ,ZT2].

## 6.6 REISSNER-MINDLIN PLATE ELEMENTS BASED ON ASSUMED TRANSVERSE SHEAR STRAIN FIELDS

### 6.6.1 Basic concepts

A thin plate element must satisfy Kirchhoff condition of zero transverse shear strains. From Eq.(6.31) we can write

$$\begin{aligned} \hat{\epsilon}_s = \mathbf{B}_s \mathbf{a}^{(e)} = & \alpha_1(w_i, \theta_i) + \alpha_2(w_i, \theta_i)\xi + \alpha_3(w_i, \theta_i)\eta + \dots\dots\dots \\ & \dots\dots\dots + \alpha_n(w_i, \theta_i)\xi^p\eta^q = 0 \end{aligned} \quad (6.53)$$

The fulfilment of Eq.(6.53) implies

$$\alpha_j(w_i, \theta_i) = 0; \quad j = 1, n \quad (6.54)$$

Eq.(6.54) imposes a linear constraint between the nodal deflections and the rotations which can be interpreted from a physical standpoint. Elements which are able to satisfy Eq.(6.54) can reproduce the thin plate condition without locking.

However, in many elements the  $\alpha_j$ 's are a function of the nodal rotations only. The condition  $\alpha_j(\theta_i) = 0$  is then too restrictive (and sometimes even non physical!) and this leads to locking.

**Example. The 4-noded plate rectangle**

As an example let us consider the simple 4-noded plate rectangle of [Figure 6.14](#). Using the standard bilinear shape functions,  $N_i = \frac{1}{4}(1 + \xi\xi_i)(1 + \eta\eta_i)$  (Appendix I) the shear strain  $\gamma_{xz}$  is given by

$$\begin{aligned} \gamma_{xz} = \frac{\partial w}{\partial x} - \theta_x = \sum_{i=1}^4 \left[ \left( \frac{\xi_i}{4a} w_i - \frac{1}{4} \theta_{x_i} \right) + \left( \frac{\xi_i \eta_i}{4a} w_i - \frac{\eta_i}{4} \theta_{x_i} \right) \eta + \right. \\ \left. + \left( \frac{\xi_i}{4} \theta_{x_i} \right) \xi - \left( \frac{\xi_i \eta_i}{4} \theta_{x_i} \right) \xi \eta \right] = \alpha_1(w_i, \theta_{x_i}) + \\ + \alpha_2(w_i, \theta_{x_i}) \eta + \alpha_3(\theta_{x_i}) \xi + \alpha_4(\theta_{x_i}) \xi \eta \end{aligned} \quad (6.55)$$

The Kirchhoff constraint  $\gamma_{xz} = 0$ , implies  $\alpha_1 = \alpha_2 = \alpha_3 = \alpha_4 = 0$ . The conditions on  $\alpha_1$  and  $\alpha_2$  are physically possible and they impose a relationship between the average rotation  $\theta_x$  over the element and the nodal deflections. However, the element is unable to satisfy naturally the conditions  $\alpha_3 = 0$  and  $\alpha_4 = 0$ , unless  $\theta_{x_i} = 0$  (which leads to  $w_i = 0$  and, hence, to locking). Identical conclusions are found for  $\gamma_{yz}$  simply by interchanging  $\xi$  by  $\eta$  and  $\theta_{x_i}$  by  $\theta_{y_i}$ . Note the analogy with the performance of the 2-noded Timoshenko beam element (Section 2.8.4).

We deduce from above that a simple way to avoid locking is to evaluate the transverse shear strains at points where the undesirable terms  $\alpha_j(\theta_i)$  vanish. For the 4-noded rectangle the terms  $\alpha_3$  and  $\alpha_4$  are zero if  $\gamma_{xz}$  and  $\gamma_{yz}$  are sampled along the lines  $\xi = 0$  and  $\eta = 0$ , respectively. The resulting expansion for  $\hat{\epsilon}_s$  is

$$\hat{\epsilon}_s = \begin{Bmatrix} \gamma_{xz} \\ \gamma_{yz} \end{Bmatrix} = \begin{Bmatrix} \alpha_1(w_i, \theta_{x_i}) + \alpha_2(w_i, \theta_{y_i}) \eta \\ \bar{\alpha}_1(w_i, \theta_{x_i}) + \bar{\alpha}_2(w_i, \theta_{y_i}) \xi \end{Bmatrix} = \bar{\mathbf{B}}_s \mathbf{a}^{(e)} \quad (6.56)$$

This transverse shear strain field can satisfy naturally the thin plate condition. *The substitute transverse shear strain matrix  $\bar{\mathbf{B}}_s$  is used instead of the original matrix  $\mathbf{B}_s$  for computing the shear stiffness matrix in Eq.(6.39b), i.e.*

$$\mathbf{K}_s^{(e)} = \iint_{A^{(e)}} \bar{\mathbf{B}}_s^T \hat{\mathbf{D}}_s \bar{\mathbf{B}}_s dA \quad (6.57)$$

The new shear stiffness matrix can now be integrated “exactly” (using a  $2 \times 2$  quadrature).

The  $\bar{\mathbf{B}}_s$  matrix was already introduced in Section 2.4.1 for the Timoshenko beam element.

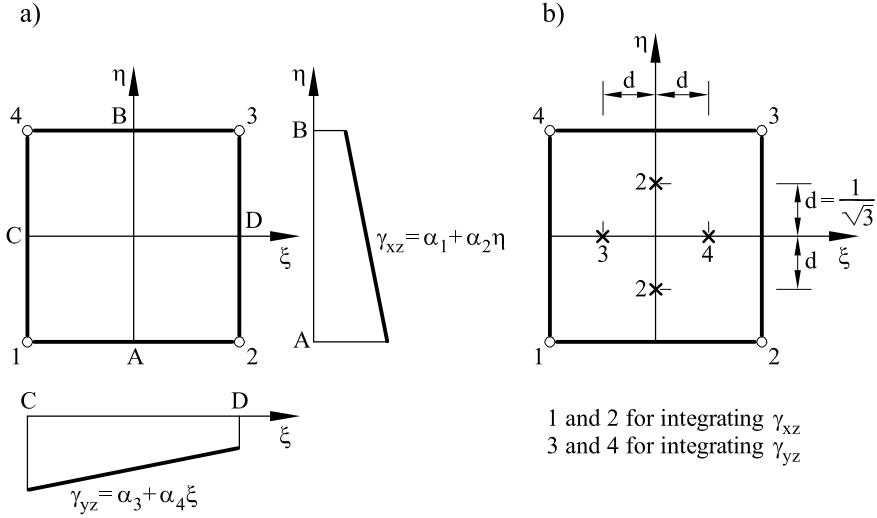


**Fig. 6.14** Four-noded plate quadrilateral. a) Assumed transverse shear strain field. b) Reduced quadrature for integrating the shear terms in the original  $\mathbf{K}_s^{(e)}$  matrix

The “assumed” transverse shear strain field is displayed in [Figure 6.14](#). The element is identical to that proposed by Bathe and Dvorkin [BD] (termed here QLLL) and is studied in some detail in Section 6.7.

For rectangles the shear stiffness matrix of Eq.(6.57) is identical to that obtained with the original  $\mathbf{B}_s$  matrix and the special reduced quadrature shown in [Figure 6.14b](#). The reasons for this coincidence are:

1. Sampling the original shear strain field at the quadrature points shown in the figure leads precisely to the assumed field of Eq.(6.56).
2. The quadrature points along the lines  $\xi = 0$  and  $\eta = 0$  integrate exactly the quadratic terms in  $\eta$  and  $\xi$  of the original shear stiffness matrix, respectively. This leads to the same stiffness matrix of Eq.(6.57) using  $2 \times 2$  integration.

Above arguments show us the coincidence between the assumed shear strain method and an “ad hoc” reduced quadrature for  $\mathbf{K}_s^{(e)}$  in the standard stiffness matrix. Unfortunately, the “special” reduced quadrature is not so simple to identify in other cases and the general procedure described next is recommended in practice.

The general method is based in imposing “a priori” a transverse shear strain field which fulfils condition (6.54), thus allowing the vanishing of  $\hat{\boldsymbol{\varepsilon}}_s$

in the thin limit. The assumed transverse shear strain interpolation is

$$\hat{\boldsymbol{\varepsilon}}_s = \sum_{k=1}^m N_{\gamma_k} \boldsymbol{\gamma}_k = \mathbf{N}_\gamma \boldsymbol{\gamma}^{(e)} \quad (6.58)$$

where  $\boldsymbol{\gamma}_k^{(e)}$  are the transverse shear strain values at  $m$  points within the element and  $N_{\gamma_k}$  are the shear interpolating functions. Combining Eqs.(6.53) and (6.58) gives

$$\hat{\boldsymbol{\varepsilon}}_s = \sum_{k=1}^m N_{\gamma_k} \mathbf{B}_{s_k} \mathbf{a}_k = \bar{\mathbf{B}}_s \mathbf{a}^{(e)} \quad (6.59)$$

Eq.(6.59) can be written in the form (6.53) and this ensures a locking-free element, as long as the conditions described in the next section are satisfied.

### 6.6.2 Selection of the transverse shear strain field

The assumed transverse shear strain field must satisfy certain conditions. The starting point is a three field mixed formulation where the deflection, the rotations and the transverse shear strains are interpolated independently as

$$w = \mathbf{N}_w \mathbf{w}^{(e)}; \quad \boldsymbol{\theta} = \mathbf{N}_\theta \boldsymbol{\theta}^{(e)}; \quad \hat{\boldsymbol{\varepsilon}}_s = \mathbf{N}_\gamma \boldsymbol{\gamma}^{(e)} \quad (6.60)$$

The conditions which must satisfy the three fields are [ZL,ZQTN,ZT2]

$$\boxed{\begin{array}{l} n_\theta + n_w \geq n_\gamma \\ n_\gamma \geq n_w \end{array}} \quad (6.61)$$

where  $n_w$ ,  $n_\theta$  y  $n_\gamma$  are the number of variables involved in the interpolation of the deflection, the rotations and the transverse shear strains, respectively (after eliminating the prescribed values). The proof of Eq.(6.61) is given in Appendix G. It is important to point out that the rotation field in Eq.(6.60) has to be  $C^0$  continuous, whereas a *discontinuous* interpolation can be used for the deflection and the transverse shear strain fields.

Note also that the conditions (6.61) are identical to (2.79) for Timoshenko beam elements.

Conditions (6.61) apply for each element, or any patch of elements, as a *necessary* (although not always sufficient) requirement for the stability of the solution [BFS3,ZL,ZQTN,ZTPO,ZT2]. The convergence must be verified via the patch test. It is interesting that the condition  $n_w + n_\theta > n_\gamma$  is analogous to the singularity condition for  $\mathbf{K}_s$  (Appendix G). This shows



the link between reduced integration and assumed transverse shear strain techniques [MH]. A systematic way for deriving  $\bar{\mathbf{B}}_s$  is presented in the next section.

### 6.6.3 Derivation of the substitute transverse shear strain matrix

We consider an isoparametric Reissner–Mindlin plate element with  $n$  nodes for which the deflection, the rotation and the transverse shear strains are interpolated independently according to Eq.(6.60). We also assume that this interpolation satisfies conditions (6.61).

#### Step 1

The transverse shear strains are interpolated in the natural coordinate system  $\xi, \eta$  as

$$\boldsymbol{\gamma}' = \begin{Bmatrix} \gamma_\xi \\ \gamma_\eta \end{Bmatrix} = \begin{bmatrix} 1 & \xi & \eta & \xi\eta & \cdots & \xi^p\eta^q & | & 0 & 0 & 0 & \cdots & 0 \\ 0 & 0 & 0 & 0 & \cdots & 0 & | & 1 & \xi & \eta & \cdots & \xi^r\eta^s \end{bmatrix} \begin{Bmatrix} \alpha_1 \\ \alpha_2 \\ \vdots \\ \alpha_{n_\gamma} \end{Bmatrix} = \mathbf{A}\boldsymbol{\alpha} \quad (6.62)$$

where  $n_\gamma$  is the number of sampling points defining the polynomial expansion for  $\gamma_\xi$  and  $\gamma_\eta$  within the element. To simplify the notation, the generalized transverse shear strain vector  $\hat{\boldsymbol{\epsilon}}_s$  is denoted hereonwards  $\boldsymbol{\gamma}$ .

The transverse shear strains in the cartesian system are obtained as

$$\boldsymbol{\gamma} = \begin{Bmatrix} \gamma_{xz} \\ \gamma_{yz} \end{Bmatrix} = \mathbf{J}^{-1}\boldsymbol{\gamma}' \quad (6.63a)$$

where  $\mathbf{J}$  is the 2D Jacobian matrix [Hu,On4,ZTZ]

$$\mathbf{J} = \begin{bmatrix} \frac{\partial x}{\partial \xi} & \frac{\partial y}{\partial \xi} \\ \frac{\partial x}{\partial \eta} & \frac{\partial y}{\partial \eta} \end{bmatrix} \quad (6.63b)$$

#### Step 2

The transverse shear strain along a natural direction  $\bar{\xi}_i$  is defined as

$$\gamma_{\bar{\xi}_i} = \cos \beta_i \gamma_\xi + \sin \beta_i \gamma_\eta \quad (6.64)$$

where  $\beta_i$  is the angle that the  $\bar{\xi}_i$  direction forms with the natural  $\xi$  axis. The  $\bar{\xi}_i$  direction along the element sides is taken so that it follows the increasing numbering of the corner nodes (Figure 6.16).

The shear strains  $\gamma_{\bar{\xi}_i}$  are sampled at each of the  $\eta_\gamma$  points placed along the  $\bar{\xi}_i$  directions. From Eq.(6.64)

$$\gamma_{\bar{\xi}} = \mathbf{T}(\beta_i)\hat{\gamma}' \quad (6.65)$$

where

$$\gamma_{\bar{\xi}} = [\gamma_{\bar{\xi}}^1, \gamma_{\bar{\xi}}^2, \dots, \gamma_{\bar{\xi}}^{n_\gamma}]^T \quad (6.66a)$$

$$\hat{\gamma}' = [\gamma_{\xi}^1, \gamma_{\eta}^1, \gamma_{\xi}^2, \gamma_{\eta}^2, \dots, \gamma_{\xi}^{n_\gamma}, \gamma_{\eta}^{n_\gamma}]^T \quad (6.66b)$$

where  $(\cdot)^1, (\cdot)^2$  etc. denote values at each sampling point.

From Eq.(6.62) it is found

$$\hat{\gamma}' = \begin{bmatrix} \mathbf{A}^1 \\ \vdots \\ \mathbf{A}^{n_\gamma} \end{bmatrix} \boldsymbol{\alpha} = \hat{\mathbf{A}}(\xi_i, \eta_i) \boldsymbol{\alpha} \quad (6.67)$$

Substituting Eq.(6.67) into (6.65) gives

$$\gamma_{\bar{\xi}} = \mathbf{P}(\xi_i, \eta_i, \beta_i) \boldsymbol{\alpha} \quad (6.68)$$

where  $\mathbf{P} = \mathbf{T}\hat{\mathbf{A}}$  is a  $n_\gamma \times n_\gamma$  matrix.

Vector  $\boldsymbol{\alpha}$  is obtained as

$$\boldsymbol{\alpha} = \mathbf{P}^{-1} \gamma_{\bar{\xi}} \quad (6.69)$$

### Step 3

Combining Eqs.(6.62), (6.65) and (6.69) gives

$$\gamma' = \mathbf{A} \mathbf{P}^{-1} \mathbf{T} \hat{\gamma}' \quad (6.70)$$

In many cases the relationship between  $\gamma'$  and  $\hat{\gamma}'$  can be written from simple observation of the assumed transverse shear strain field. This allows writing directly the matrix resulting from the product  $\mathbf{A}\mathbf{P}^{-1}\mathbf{T}$ .

### Step 4

The relationship between the cartesian and the natural transverse shear strains at each sampling point is

$$\hat{\gamma}'_i = \begin{Bmatrix} \gamma_{\xi}^i \\ \gamma_{\eta}^i \end{Bmatrix} = \mathbf{J}^i \begin{Bmatrix} \gamma_{xz}^i \\ \gamma_{yz}^i \end{Bmatrix} = \mathbf{J}^i \hat{\gamma}^i \quad (6.71)$$

where  $\mathbf{J}^i$  is the Jacobian matrix at the  $i$ th sampling point. Thus,

$$\hat{\boldsymbol{\gamma}}' = \begin{bmatrix} \mathbf{J}^1 & \mathbf{0} \\ & \ddots \\ \mathbf{0} & \mathbf{J}^{n_\gamma} \end{bmatrix} \begin{Bmatrix} \hat{\boldsymbol{\gamma}}^1 \\ \vdots \\ \hat{\boldsymbol{\gamma}}^{n_\gamma} \end{Bmatrix} = \mathbf{C} \hat{\boldsymbol{\gamma}} \quad (6.72)$$

Substituting Eqs.(6.70) and (6.72) into (6.63a) gives

$$\boldsymbol{\gamma} = \mathbf{J}^{-1} \mathbf{A} \mathbf{P}^{-1} \mathbf{T} \mathbf{C} \hat{\boldsymbol{\gamma}} = \mathbf{N}_\gamma \hat{\boldsymbol{\gamma}} \quad (6.73)$$

where

$$\mathbf{N}_\gamma = \mathbf{J}^{-1} \mathbf{A} \mathbf{P} \mathbf{T}^{-1} \mathbf{C} \quad (6.74)$$

are the shape functions which interpolate the cartesian transverse shear strains in terms of their values at the sampling points.

### Step 5

The general relationship between the cartesian transverse shear strains and the nodal displacements for each element can be written using a weighted residual procedure [OZST,ZT2,ZTZ] as

$$\iint_{A^{(e)}} W_k [\boldsymbol{\gamma} - (\boldsymbol{\nabla} w - \boldsymbol{\theta})] dA = \mathbf{0} \quad (6.75)$$

where  $\boldsymbol{\nabla} = \left[ \frac{\partial}{\partial x}, \frac{\partial}{\partial y} \right]^T$  and  $W_k$  are arbitrarily chosen weighting functions. Eq.(6.75) imposes the satisfaction of the equality  $\boldsymbol{\gamma} = \boldsymbol{\nabla} w - \boldsymbol{\theta}$  in a mean integral sense over the element.

Substituting Eqs.(6.73) and (6.31) into (6.75) and choosing a Galerkin weighting, i.e.  $W_k = N_{\gamma_k}$  [ZTZ] gives

$$\left[ \iint_{A^{(e)}} \mathbf{N}_\gamma^T \mathbf{N}_\gamma dA \right] \hat{\boldsymbol{\gamma}} = \left[ \iint_{A^{(e)}} \mathbf{N}_\gamma^T \mathbf{B}_s dA \right] \mathbf{a}^{(e)} \quad (6.76)$$

where  $\mathbf{B}_s$  is the standard transverse shear strain matrix of Eq.(6.32). Eq.(6.76) is used to obtain the shear strains at the sampling points for each element as

$$\hat{\boldsymbol{\gamma}} = \hat{\mathbf{B}}_s \mathbf{a}^{(e)} \quad (6.77)$$

with

$$\hat{\mathbf{B}}_s = \left[ \iint_{A^{(e)}} \mathbf{N}_\gamma^T \mathbf{N}_\gamma dA \right]^{-1} \iint_{A^{(e)}} \mathbf{N}_\gamma^T \mathbf{B}_s dA \quad (6.78)$$

A simpler procedure is to use point collocation in Eq.(6.75). This implies choosing  $W_i = \delta_i$  where  $\delta_i$  is the Dirac delta at the  $i$ th sampling point ( $i = 1, \dots, n_\gamma$ ). This gives

$$\hat{\mathbf{B}}_s = \begin{Bmatrix} \mathbf{B}_s^1 \\ \vdots \\ \mathbf{B}_s^{n_\gamma} \end{Bmatrix} \quad (6.79)$$

where  $\mathbf{B}_s^i$  is the value of the original transverse shear strain matrix at the  $i$ th sampling point.

### Step 6

Combining steps 1–5 yields finally

$$\boldsymbol{\gamma} = \mathbf{J}^{-1} \mathbf{A} \mathbf{P}^{-1} \mathbf{T} \mathbf{C} \hat{\mathbf{B}}_s \mathbf{a}^{(e)} = \bar{\mathbf{B}}_s \mathbf{a}^{(e)} \quad (6.80)$$

where  $\bar{\mathbf{B}}_s$  is the substitutive transverse shear strain matrix given by

$$\boxed{\bar{\mathbf{B}}_s = \mathbf{J}^{-1} \mathbf{A} \mathbf{P}^{-1} \mathbf{T} \mathbf{C} \hat{\mathbf{B}}_s} \quad (6.81)$$

The weighting procedure described in Step 5 is not the only alternative to derive a relationship between the transverse shear strains and the nodal displacements. One could for instance require integrals such as

$$\int_{\Gamma^{(e)}} W_k \left[ \gamma_{\bar{\xi}} - \left( \frac{\partial w}{\partial \bar{\xi}} - \theta_{\bar{\xi}} \right) \right] d\Gamma \quad (6.82)$$

to vanish on a segment of the element boundary  $\Gamma^{(e)}$ . This allows us to obtain directly a relationship of the form

$$\boldsymbol{\gamma}_{\bar{\xi}} = [\mathbf{T} \mathbf{C} \mathbf{B}] \mathbf{a}^{(e)} \quad (6.83)$$

and the substitute shear strain matrix is given by [OTZ,OZST,ZT2]

$$\bar{\mathbf{B}}_s = \mathbf{J}^{-1} \mathbf{A} \mathbf{P}^{-1} [\mathbf{T} \mathbf{C} \mathbf{B}] \quad (6.84)$$

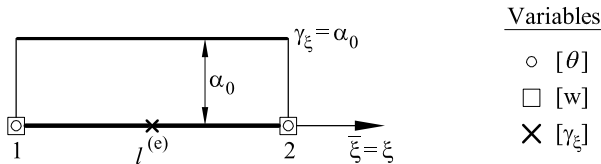


Fig. 6.15 2-noded Timoshenko beam element

**Example 6.1:** Obtain the substitutive transverse shear strain matrix for the 2-noded Timoshenko beam element using a constant shear strain field.

**- Solution**

The element is shown in Figure 6.15. In this case

$$\gamma_\xi = (\alpha_0 + \alpha_1 \xi)_{\xi=0} = \alpha_0, \quad \mathbf{A} = [1]$$

The natural direction  $\bar{\xi}$  coincides with  $\xi$  and therefore

$$\gamma_{\bar{\xi}} = \gamma_\xi; \quad \beta = 0 \quad \text{and} \quad \mathbf{P} = [1], \quad \mathbf{T} = [1]$$

Also

$$\begin{aligned} (\gamma_\xi)_{\xi=0} &= \frac{l^{(e)}}{2} (\gamma_x)_{\xi=0} \quad \text{and} \quad \mathbf{J} = \left[ \frac{l^{(e)}}{2} \right], \quad \mathbf{C} = \left[ \frac{l^{(e)}}{2} \right] \\ (\gamma_x)_{\xi=0} &= \frac{1}{l^{(e)}} \left[ -1, -\frac{l^{(e)}}{2}, 1, -\frac{l^{(e)}}{2} \right] \mathbf{a}^{(e)} = \hat{\mathbf{B}}_s \mathbf{a}^{(e)} \end{aligned} \quad (6.85)$$

Finally from Eq.(6.81)

$$\bar{\mathbf{B}}_s = \mathbf{J}^{-1} \mathbf{A} \mathbf{P}^{-1} \mathbf{T} \mathbf{C} \hat{\mathbf{B}}_s = \frac{1}{l^{(e)}} \left[ -1, -\frac{l^{(e)}}{2}, 1, -\frac{l^{(e)}}{2} \right]$$

Note that  $\bar{\mathbf{B}}_s$  coincides with the original  $\mathbf{B}_s$  matrix (Eq.(2.15)) evaluated at the element mid-point. This is another evidence of the analogy between the assumed transverse shear strain procedure and reduced integration (see also Section 2.8.4 and Example 2.8).

## 6.7 REISSNER-MINDLIN PLATE QUADRILATERALS BASED ON ASSUMED TRANSVERSE SHEAR STRAIN FIELDS

### 6.7.1 4-noded plate quadrilateral with linear shear field (QLLL)

This popular element was initially developed by Bathe and Dvorkin [BD,DB]. Its formulation can be considered a particularization of the procedures based on auxiliary transverse shear modes proposed by Mac Neal [Ma, Ma2] and Hughes *et al.* [HTT]. Donea and Lamain [DL] and Oñate *et al.* [OTZ, OZBT] derived the element using assumed strain concepts. In

the following lines we will derive the element following the methodology described in Section 6.6.3.

The starting point is the standard 4-noded Q4 element of Section 6.5.1 with a bilinear interpolation of the deflections and the rotations. We define an assumed transverse shear strain field in the natural system  $\xi, \eta$  as (Figure 6.14a)

$$\begin{aligned}\gamma_\xi &= \alpha_1 + \alpha_2\eta \\ \gamma_\eta &= \alpha_3 + \alpha_4\xi; \quad \text{i.e.} \quad \mathbf{A} = \begin{bmatrix} 1 & \eta & 0 & 0 \\ 0 & 0 & 1 & \xi \end{bmatrix}\end{aligned}\quad (6.86)$$

The  $\alpha_i$  parameters are found by sampling the natural transverse shear strains  $\gamma_{\bar{\xi}}$  at the four mid-side points shown in Figure 6.16, with

$$\gamma_{\bar{\xi}_i} = (\alpha_1 + \alpha_2\eta) \cos \beta_i + (\alpha_3 + \alpha_4\xi) \sin \beta_i; \quad i = 1, 4 \quad (6.87)$$

where  $\beta_i$  is the angle between the  $\bar{\xi}_i$  and  $\xi$  axis. A simple operation gives

$$\underbrace{\begin{bmatrix} 1 & -1 & 0 & 0 \\ 0 & 0 & 1 & 1 \\ -1 & -1 & 0 & 0 \\ 0 & 0 & 1 & -1 \end{bmatrix}}_{\mathbf{P}} \begin{Bmatrix} \alpha_1 \\ \alpha_2 \\ \alpha_3 \\ \alpha_4 \end{Bmatrix} = \begin{Bmatrix} \gamma_{\bar{\xi}}^1 \\ \gamma_{\bar{\xi}}^2 \\ \gamma_{\bar{\xi}}^3 \\ \gamma_{\bar{\xi}}^4 \end{Bmatrix} \quad \text{and} \quad \mathbf{P}^{-1} = \frac{1}{2} \begin{bmatrix} 1 & 0 & -1 & 0 \\ -1 & 0 & -1 & 0 \\ 0 & 1 & 0 & 1 \\ 0 & 1 & 0 & -1 \end{bmatrix} \quad (6.88)$$

The strains  $\gamma_{\bar{\xi}}^i$  are related to  $\gamma_{\xi}^i, \gamma_{\eta}^i$  by

$$\begin{Bmatrix} \gamma_{\bar{\xi}}^1 \\ \gamma_{\bar{\xi}}^2 \\ \gamma_{\bar{\xi}}^3 \\ \gamma_{\bar{\xi}}^4 \end{Bmatrix} = \begin{bmatrix} 1 & 0 & & \mathbf{0} \\ & 0 & 1 & \\ & & -1 & 0 \\ \mathbf{0} & & & 0 & 1 \end{bmatrix} \begin{Bmatrix} \gamma_{\xi}^1 \\ \gamma_{\eta}^1 \\ \vdots \\ \gamma_{\xi}^4 \\ \gamma_{\eta}^4 \end{Bmatrix} = \mathbf{T} \hat{\boldsymbol{\gamma}}' \quad (6.89)$$

The cartesian transverse shear strains at the sampling points are related to the natural transverse shear strains by

$$\hat{\boldsymbol{\gamma}}' = \begin{bmatrix} \mathbf{J}^1 & & \mathbf{0} \\ & \mathbf{J}^2 & \\ & & \mathbf{J}^3 \\ \mathbf{0} & & & \mathbf{J}^4 \end{bmatrix} \begin{Bmatrix} \hat{\boldsymbol{\gamma}}^1 \\ \vdots \\ \hat{\boldsymbol{\gamma}}^4 \end{Bmatrix} = \mathbf{C} \hat{\boldsymbol{\gamma}} \quad ; \quad \hat{\boldsymbol{\gamma}}^i = \begin{Bmatrix} \gamma_{xz}^i \\ \gamma_{yz}^i \end{Bmatrix} \quad (6.90)$$

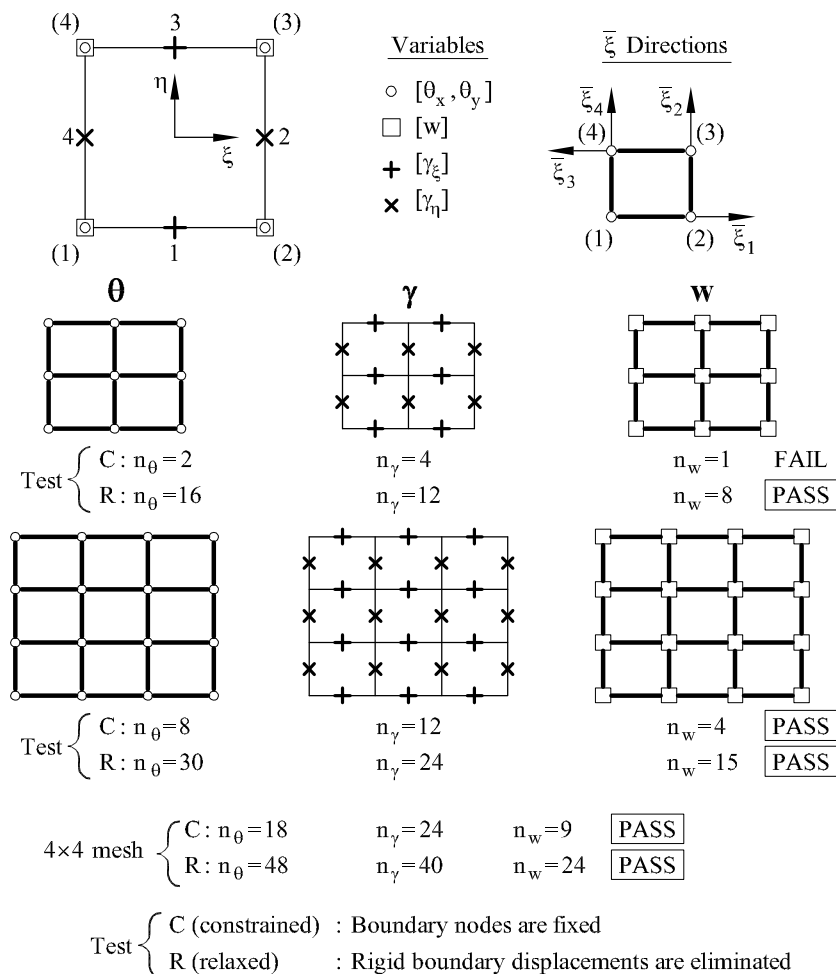


**Fig. 6.16** 4-noded Reissner-Mindlin plate quadrilateral with assumed linear transverse shear strain field (QLLL). Numbers within brackets denote node numbers

The relationship between the cartesian transverse shear strains at the four sampling points and the nodal displacements is

$$\hat{\gamma} = \begin{Bmatrix} \mathbf{B}_s^1 \\ \mathbf{B}_s^2 \\ \mathbf{B}_s^3 \\ \mathbf{B}_s^4 \end{Bmatrix} \mathbf{a}^{(e)} = \hat{\mathbf{B}}_s \mathbf{a}^{(e)} \quad (6.91)$$

The substitute transverse shear strain matrix is obtained by Eq.(6.81).

This element has been given different names in the literature [ZT2]. Here it is termed QLLL (for **Q**uadrilateral, bi**L**inear deflection, bi**L**inear rotations and **L**inear transverse shear strain fields). The QLLL element satisfies conditions (6.61) for meshes of more than  $2 \times 2$  elements (Figure 6.16) and it is considered robust for practical applications. Computation of the stiffness matrix requires a full  $2 \times 2$  quadrature for *all* terms, and this preserves the element from spurious mechanisms. The bending moments and shear forces are constant along each natural direction. Hence fine meshes are required for certain applications. The extension for shell analysis is studied in Chapter 9.

The product  $\mathbf{A} \mathbf{P}^{-1} \mathbf{T}$  in Eq.(6.70) is

$$\mathbf{A} \mathbf{P}^{-1} \mathbf{T} = \frac{1}{2} \left[ \begin{array}{cc|cc} (1-\eta) & 0 & 0 & (1+\eta) & 0 & 0 \\ 0 & 0 & 0 & 0 & 0 & 0 \end{array} \right] \quad (6.92)$$

This matrix could have been anticipated by writing directly the assumed transverse shear strain field as

$$\begin{aligned} \gamma_\xi &= \frac{1}{2}(1-\eta)\gamma_\xi^1 + \frac{1}{2}(1+\eta)\gamma_\xi^3 \\ \gamma_\eta &= \frac{1}{2}(1+\xi)\gamma_\eta^2 + \frac{1}{2}(1-\xi)\gamma_\eta^4 \end{aligned} \quad (6.93)$$

### 6.7.2 8-noded Serendipity plate quadrilateral with assumed quadratic transverse shear strain field (QQQQ-S)

The starting point is the QS8 plate quadrilateral of Section 6.5.2. The fulfilment of conditions (6.61) requires an assumed transverse shear strain field containing ten terms. The simplest choice is

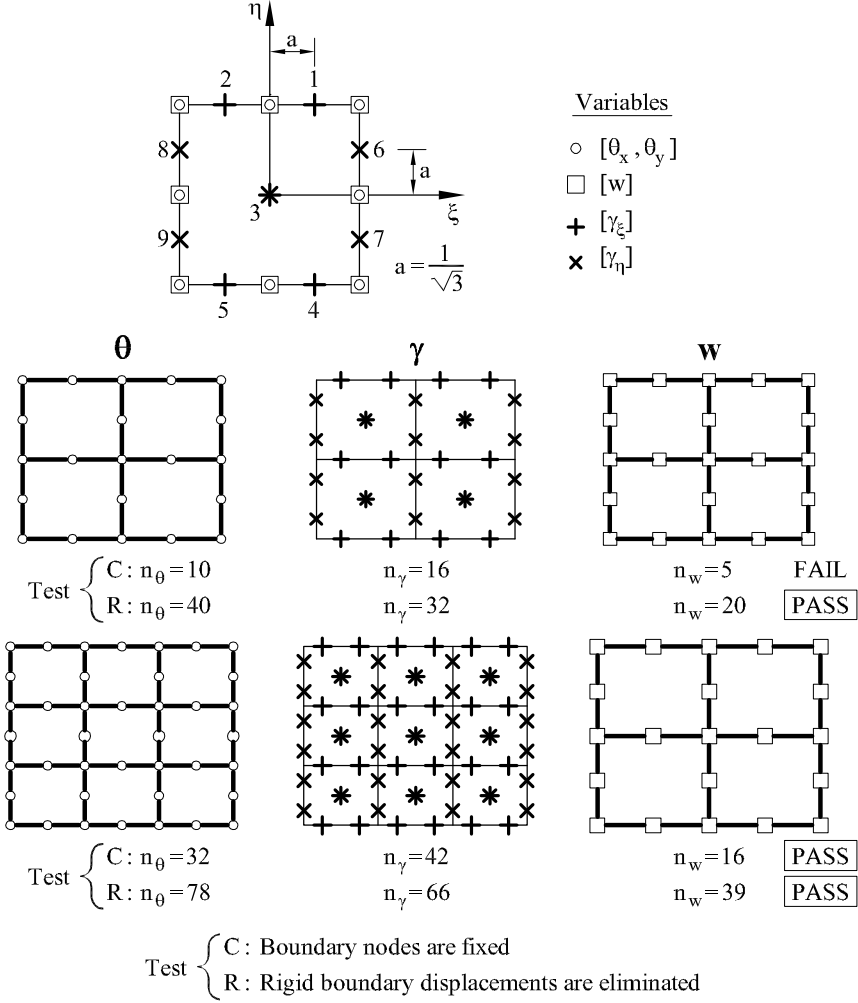
$$\begin{aligned} \gamma_\xi &= \alpha_1 + \alpha_2\xi + \alpha_3\eta + \alpha_4\xi\eta + \alpha_5\eta^2 \\ \gamma_\eta &= \alpha_6 + \alpha_7\xi + \alpha_8\eta + \alpha_9\xi\eta + \alpha_{10}\xi^2 \end{aligned} \quad (6.94)$$

Figure 6.17 shows the sampling points for the transverse shear strains  $\gamma_\xi$  and  $\gamma_\eta$  (two points along each side and the central point). The  $\bar{\xi}$  directions coincide with those defined for the QLLL element (Figure 6.16).

The derivation of the substitute transverse shear strain matrix can be simplified if we define the assumed field for  $\gamma_\xi$  as

$$\begin{aligned} \gamma_\xi &= \frac{1}{4} \left[ \left( 1 + \frac{1}{a}\xi \right) \gamma_\xi^1 + \left( 1 - \frac{1}{a}\xi \right) \gamma_\xi^2 \right] (1+\eta) + \\ &+ \frac{1}{4} \left[ \left( 1 + \frac{1}{a}\xi \right) \gamma_\xi^4 + \left( 1 - \frac{1}{a}\xi \right) \gamma_\xi^5 \right] (1-\eta) + (1-\eta^2)\gamma_\xi^3 \end{aligned} \quad (6.95)$$





**Fig. 6.17** 8-noded Reissner-Mindlin plate quadrilateral with an assumed quadratic transverse shear strain field (QQQQ-S)

with  $a = \frac{1}{\sqrt{3}}$ . A similar interpolation can be written for  $\gamma_\eta$  simply interchanging  $\xi$  by  $\eta$  and the points 1,2,4,5 by 6,7,8 and 9, respectively in Eq.(6.94). This yields directly the product  $\mathbf{A} \mathbf{P}^{-1} \mathbf{T}$  in Eq.(6.70) as

$$\mathbf{A} \mathbf{P}^{-1} \mathbf{T} = \begin{bmatrix} \frac{A\eta_1}{4} & 0 & \frac{B\eta_1}{4} & 0 & \eta_3 & 0 & \frac{A\eta_2}{4} & 0 & \frac{B\eta_2}{4} & 0 & \mathbf{0}_{1 \times 8} \\ \mathbf{0}_{1 \times 8} & 0 & \frac{\bar{A}\xi_1}{4} & 0 & \frac{\bar{B}\xi_1}{4} & 0 & \xi_3 & 0 & \frac{\bar{A}\xi_2}{4} & 0 & \frac{\bar{B}\xi_2}{4} \end{bmatrix} \quad (6.96)$$

with

$$\begin{aligned} A = 1 + \sqrt{3}\xi, \quad B = 1 - \sqrt{3}\xi, \quad \bar{A} = 1 + \sqrt{3}\eta, \quad \bar{B} = 1 - \sqrt{3}\eta \\ s_1 = 1 + s, \quad s_2 = 1 - s, \quad s_3 = 1 - s^2 \quad \text{with } s = \xi, \eta \end{aligned} \quad (6.97)$$

The following expressions for  $\mathbf{C}$  and  $\hat{\mathbf{B}}_s$  are necessary for computing the constitutive transverse shear strain matrix  $\bar{\mathbf{B}}_s$  via Eq.(6.81)

$$\mathbf{C} = \begin{bmatrix} \mathbf{J}_1 & & & \mathbf{0} \\ & \mathbf{J}_2 & & \\ & & \ddots & \\ \mathbf{0} & & & \mathbf{J}_9 \end{bmatrix}, \quad \hat{\mathbf{B}}_s = \begin{Bmatrix} \mathbf{B}_s^1 \\ \mathbf{B}_s^2 \\ \vdots \\ \mathbf{B}_s^9 \end{Bmatrix} \quad (6.98)$$

The global stiffness matrix is integrated with a full  $3 \times 3$  quadrature which eliminates any spurious mechanisms [DL,HH2,HH4].

This element is termed QQQQ-S (for **S**erendipity plate **Q**uadrilateral with **Q**uadratic deflection, **Q**uadratic rotations and **Q**uadratic transverse shear strain fields). Conditions (6.61) are satisfied for meshes of more than  $2 \times 2$  elements (Figure 6.17).

### 6.7.3 9-noded Lagrange plate quadrilateral with assumed quadratic transverse shear strain field (QQQQ-L)

The starting point is the QL9 element of Section 6.5.3. Satisfaction of condition (6.61) requires the following assumed transverse shear strain field containing 12 terms

$$\begin{aligned} \gamma_\xi &= \alpha_1 + \alpha_2\xi + \alpha_3\eta + \alpha_4\xi\eta + \alpha_5\eta^2 + \alpha_6\xi\eta^2 \\ \gamma_\eta &= \alpha_7 + \alpha_8\xi + \alpha_9\eta + \alpha_{10}\xi\eta + \alpha_{11}\xi^2 + \alpha_{12}\eta\xi^2 \end{aligned} \quad (6.99)$$

Figure 6.18 displays the sampling points for the transverse shear strains. The  $\bar{\xi}$  directions coincide again with those shown in Figure 6.16.

Direct observation gives the  $\gamma_\xi$  field as

$$\begin{aligned} \gamma_\xi &= \frac{1}{4} \left[ \left(1 + \frac{1}{a}\xi\right)\gamma_\xi^1 + \left(1 - \frac{1}{a}\xi\right)\gamma_\xi^2 \right] \eta(1 + \eta) + \\ &\quad + \frac{1}{2} \left[ \left(1 + \frac{1}{a}\xi\right)\gamma_\xi^3 + \left(1 - \frac{1}{a}\xi\right)\gamma_\xi^4 \right] (1 - \eta^2) + \\ &\quad + \frac{1}{4} \left[ \left(1 + \frac{1}{a}\xi\right)\gamma_\xi^5 + \left(1 - \frac{1}{a}\xi\right)\gamma_\xi^6 \right] \eta(\eta - 1) \end{aligned} \quad (6.100)$$



where  $A, B, \bar{A}$  and  $\bar{B}$  coincide with the values given in Eq.(6.97) and

$$s_1 = s(1 + s), \quad s_2 = 1 - s^2, \quad s_3 = s(1 - s) \quad \text{with } s = \xi, \eta \quad (6.102)$$

The  $\mathbf{C}$  and  $\hat{\mathbf{B}}_s$  matrices for computing the substitute transverse shear strain matrix are

$$\mathbf{C} = \begin{bmatrix} \mathbf{J}_1 & & & \mathbf{0} \\ & \mathbf{J}_2 & & \\ & & \ddots & \\ \mathbf{0} & & & \mathbf{J}_{12} \end{bmatrix}, \quad \hat{\mathbf{B}}_s = \begin{Bmatrix} \mathbf{B}_s^1 \\ \mathbf{B}_s^2 \\ \vdots \\ \mathbf{B}_s^{12} \end{Bmatrix} \quad (6.103)$$

A full  $3 \times 3$  quadrature is used for integrating *all* the stiffness matrix terms and this eliminates the spurious mechanisms. The element satisfies conditions (6.61) for meshes with more than one element (Figure 6.18).

The element is termed QQQQ-L (for **L**agrange plate **Q**uadrilateral with **Q**uadratic deflection, **Q**uadratic rotations and **Q**uadratic trasverse shear strain fields). This element was simultaneously developed by Hinton and Huang [HH3,HH4] and Bathe and Dvorkin [BD2]. Donea y Lamain [DL] presented a different version of the element based in the direct derivation of expressions (6.100) in cartesian coordinates. The performance of the QQQQ-L element is superior to the QQQQ-S.

### 6.7.4 Sixteen DOFs plate quadrilateral (QLQL)

The interpolating fields are the following.

1. The deflection is bi-linearly interpolated as

$$w = \sum_{i=1}^4 N_i w_i \quad (6.104)$$

where  $N_i$  are the bilinear shape functions of the Q4 element.

2. An incomplete quadratic interpolation is chosen for the rotations as

$$\begin{aligned} \boldsymbol{\theta} = & \sum_{i=1}^4 N_i \boldsymbol{\theta}_i + f(\xi)(1 - \eta) \mathbf{e}_{12} \Delta \theta_{s_5} + f(\eta)(1 + \xi) \mathbf{e}_{23} \Delta \theta_{s_6} + \\ & + f(\xi)(1 + \eta) \mathbf{e}_{23} \Delta \theta_{s_7} + f(\eta)(1 - \xi) \mathbf{e}_{14} \Delta \theta_{s_8} \end{aligned} \quad (6.105)$$

where  $f(\xi) = 1 - \xi^2$  and  $f(\eta) = 1 - \eta^2$ . In above  $\Delta \theta_{S_i}$  is a hierarchical tangential mid-side rotation and  $\mathbf{e}_{ij}$  are unit vectors along the side directions (Figure 6.19).

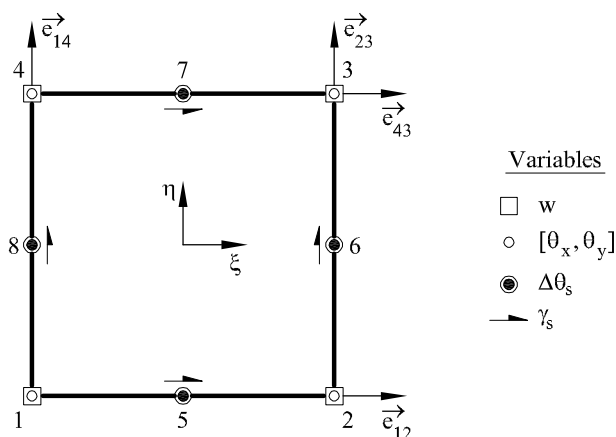


**Fig. 6.19** Sixteen DOFs QLLQ Reissner-Mindlin plate quadrilateral, ( $w$  linear,  $\theta$ , quadratic and  $\gamma$  linear)

3. The transverse shear strains are assumed to vary linearly as in Eq.(6.86). The substitute transverse shear strain matrix is found as explained for the QLL element (Section 6.7.1). A  $2 \times 2$  quadrature is used for all the terms of the stiffness matrix.

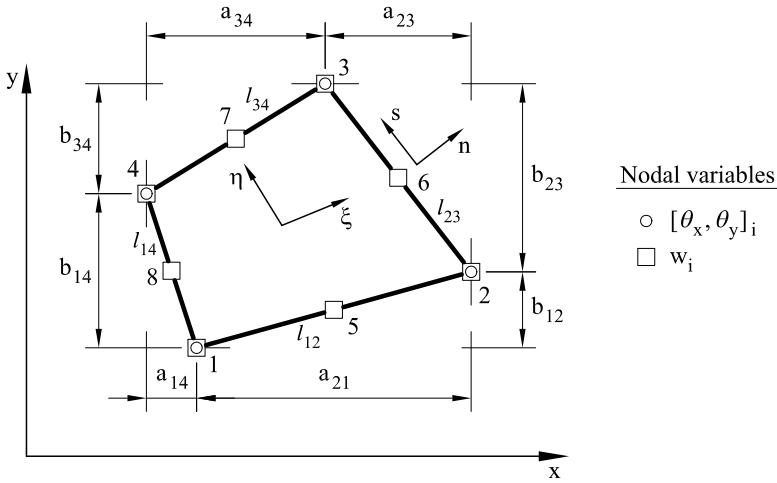
The element is termed QLLQ (for **Q**uadrilateral, **b**iLinear deflection, **Q**uadratic rotations and **L**inear transverse shear strain fields) and it satisfies conditions (6.61) for all meshes.

The hierarchical side rotations can be eliminated by imposing the condition of zero transverse shear strains along the sides. This leads to a 4-noded Discrete Kirchhoff thin plate quadrilateral identical to that proposed by Batoz and Ben Tahar [BBt] (Section 6.11.2). A procedure for eliminating the side rotations while still preserving some shear strain energy within the element is described in [BBt,BD5].

### 6.7.5 4-noded plate quadrilateral of Tessler-Hughes

Tessler and Hughes [TH] derived a plate quadrilateral with a quadratic interpolation for the deflection, a linear one for the rotations and a constant transverse shear strain along the sides. The element is free from spurious mechanisms and applicable to both thick and thin plates.

The formulation shares some similarities with the Heterosis and Hierarchical plate elements (Sections 6.5.4–6.5.6). The starting point is the standard 8-noded Serendipity interpolation for the deflection, while the



Average size dimensions :  $a = \frac{1}{2}(l_{12} + l_{34})$ ;  $b = \frac{1}{2}(l_{14} + l_{23})$

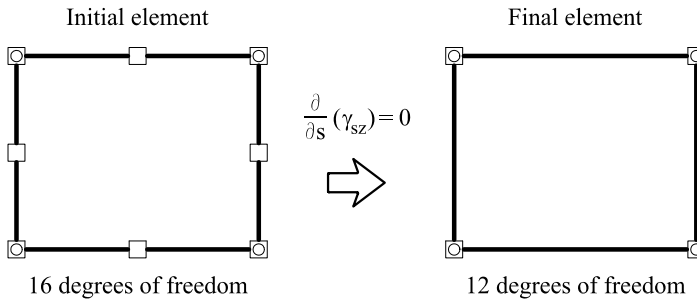


**Fig. 6.20** Four-noded plate quadrilateral of Tessler and Hughes [TH]

rotations are bilinearly interpolated using the corner node values (Figure 6.20). Thus

$$\mathbf{u} = \begin{Bmatrix} w \\ \theta_x \\ \theta_y \end{Bmatrix} = \begin{bmatrix} \bar{\mathbf{N}}(\xi^2, \eta^2) & 0 & 0 \\ 0 & \mathbf{P}(\xi, \eta) & 0 \\ 0 & 0 & \mathbf{P}(\xi, \eta) \end{bmatrix} \begin{Bmatrix} \mathbf{w} \\ \boldsymbol{\theta}_x \\ \boldsymbol{\theta}_y \end{Bmatrix}^{(e)} = \hat{\mathbf{N}} \mathbf{a}^{(e)} \quad (6.106)$$

where  $\bar{\mathbf{N}}(\xi^2, \eta^2) = [N_1, N_2, \dots, N_8]$  are the quadratic shape functions of the QS8 element and  $\mathbf{P}(\xi, \eta) = [P_1, P_2, P_3, P_4]$  are the bilinear shape functions of the QL4 element. The nodal displacement vector is written as

$$\mathbf{a}^{(e)}_{16 \times 1} = [w_1, \dots, w_8, \theta_{x_1}, \dots, \theta_{x_4}, \theta_{y_1}, \dots, \theta_{y_4}]^T \quad (6.107)$$

The 4-noded configuration is reached after eliminating the mid-side deflections  $w_5, w_6, w_7$  and  $w_8$  by imposing a constant transverse shear

strain  $\gamma_{sz}$  along the sides, where  $s$  is the size direction (Figure 6.20). This ensures continuity of the tangential transverse shear strain across the sides of adjacent elements. The final displacement interpolation is written as

$$\mathbf{u} = \mathbf{N}\hat{\mathbf{a}}^{(e)} \quad (6.108)$$

where

$$\hat{\mathbf{a}}^{(e)} = [w_1, \dots, w_4, \theta_{x_1}, \dots, \theta_{x_4}, \theta_{y_1}, \dots, \theta_{y_4}]^T_{12 \times 1}$$

$$\mathbf{N} = \begin{bmatrix} \mathbf{P}(\xi, \eta) & \mathbf{N}_x(\xi^2, \eta^2) & \mathbf{N}_y(\xi^2, \eta^2) \\ \mathbf{0} & \mathbf{P}(\xi, \eta) & \mathbf{0} \\ \mathbf{0} & \mathbf{0} & \mathbf{P}(\xi, \eta) \end{bmatrix} \quad (6.109)$$

with  $\mathbf{N}_x = [N_{x_1}, N_{x_2}, N_{x_3}, N_{x_4}]$ ,  $\mathbf{N}_y = [N_{y_1}, N_{y_2}, N_{y_3}, N_{y_4}]$  and

$$\begin{aligned} N_{x_1} &= \frac{1}{8} [-b_{12}N_5 - b_{14}N_8]; & N_{x_2} &= \frac{1}{8} [b_{12}N_5 - b_{23}N_6] \\ N_{x_3} &= \frac{1}{8} [b_{23}N_6 + b_{34}N_7]; & N_{x_4} &= \frac{1}{8} [-b_{34}N_7 + b_{14}N_8] \\ N_{y_1} &= \frac{1}{8} [-a_{12}N_5 + a_{14}N_8]; & N_{y_2} &= \frac{1}{8} [a_{12}N_5 + a_{23}N_6] \\ N_{y_3} &= \frac{1}{8} [a_{34}N_7 - a_{23}N_6]; & N_{y_4} &= \frac{1}{8} [-a_{34}N_7 - a_{14}N_8] \end{aligned} \quad (6.110)$$

where  $a_{ij}$  and  $b_{ij}$  are given in Figure 6.20.

Note that the interpolation for the deflection involves also the rotations. This can be seen as a class of “linked interpolation” (Section 6.10).

The geometry is defined in sub-parametric manner using the corner nodes coordinates. The bending and transverse shear strain matrices are

$$\mathbf{B}_b = \begin{bmatrix} \mathbf{0} & \frac{\partial}{\partial x} \mathbf{P} & \mathbf{0} \\ \mathbf{0} & \mathbf{0} & \frac{\partial}{\partial y} \mathbf{P} \\ \mathbf{0} & -\frac{\partial}{\partial y} \mathbf{P} & -\frac{\partial}{\partial x} \mathbf{P} \end{bmatrix}, \quad \mathbf{B}_s = \begin{bmatrix} \frac{\partial}{\partial x} \mathbf{P} \left( \frac{\partial}{\partial x} \mathbf{N}_x - \mathbf{P} \right) & \frac{\partial}{\partial x} \mathbf{P} \\ \frac{\partial}{\partial y} \mathbf{P} & \frac{\partial}{\partial y} \mathbf{P} \left( \frac{\partial}{\partial y} \mathbf{N}_y - \mathbf{P} \right) \end{bmatrix} \quad (6.111)$$

The equivalent nodal force vector for distributed loads is

$$\mathbf{f}^{(e)} = \iint_{A^{(e)}} \left( f_z \begin{Bmatrix} \mathbf{P}^T \\ \mathbf{N}_x^T \\ \mathbf{N}_y^T \end{Bmatrix} + \begin{Bmatrix} \mathbf{0} \\ m_x \mathbf{P}^T \\ m_y \mathbf{P}^T \end{Bmatrix} \right) dA \quad (6.112)$$

Note that bending moment components are introduced in  $\mathbf{f}^{(e)}$  by the distributed load  $f_z$ .

A  $2 \times 2$  reduced quadrature eliminates spurious mechanisms and avoids locking. However, the behaviour of the element is somehow stiff for very thin plates.

An enhanced element can be derived by modifying the shear correction parameter  $k$  as we did by using a substitute shear modulus for Timoshenko beams (Section 2.6). The substitute shear correction parameter  $k^*$  is found by comparing the analytical solution for a simple supported rectangular plate with that obtained with a single element in a quarter of the plate (using symmetry conditions) giving [TH]

$$k^* = \frac{C_b \psi}{1 + C_b \psi} k \quad \text{with} \quad \psi = \frac{w_s}{w_b} \quad (6.113)$$

where  $w_b$  and  $w_s$  are the bending and shear contributions to the analytical solution for the central deflection and  $C_b$  is a number close to unity deduced from numerical experiments. Good results were reported in [TH] using  $C_b = 0.9$  and the value of  $\psi$  obtained from the analysis of a rectangular plate ( $a \times b$ ) under sine loading giving

$$\psi = \frac{\pi^2}{6(1-\nu)k} \left( \frac{t}{a} \right)^2 \left[ 1 + \frac{a^2}{b^2} \right] \quad (6.114)$$

For arbitrary shape elements  $a$  and  $b$  are taken as the average side lengths (Figure 6.20).

Similar substitute shear correction parameters for Reissner-Mindlin plate elements have been suggested [Fr,Fr2,FY,Ma,Ma2,SV,TH2]. A simple one was proposed by Carpenter *et al.* [CBS] as

$$k^* = \frac{c}{1 + c} k \quad \text{with} \quad c = \frac{E t^2}{2\alpha G(1-\nu^2)A^{(e)}} \quad (6.115)$$

### 6.7.6 8-noded plate quadrilateral proposed by Crisfield

Crisfield [Cr3] developed an 8-noded thick quadrilateral following similar arguments as for the 4-noded Tessler-Hughes element of the previous section. The starting point is the 27 DOFs quadrilateral of Figure 6.21. The standard quadratic 8-noded Serendipity interpolation is used for the rotations and a quadratic 9-noded Lagrange field is used for the deflections.

The four mid-side deflections are eliminated by imposing a constant tangential shear strains along the sides. The central deflection is eliminated by imposing an “effective” constant shear strain field along the two diagonals (Example 2.8).



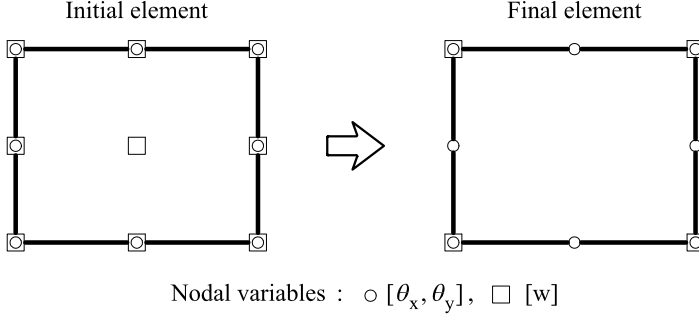


**Fig. 6.21** 8-noded plate quadrilateral of Crisfield [Cr3]

The final element has 20 DOFs as shown in Figure 6.21. A full  $3 \times 3$  quadrature is required for all the stiffness terms. This element has similar features as the QQLQ of Section 6.7.4 but has more DOFs.

### 6.7.7 Higher order 12 and 16-noded plate quadrilaterals with assumed transverse shear strain fields

Hinton and Huang [HH2,HH4] developed 12 and 16-noded plate quadrilaterals using assumed transverse shear strain fields with 16 and 24 parameters, respectively. The elements perform well for thick and thin plates but contain an excessive number of variables for practical purposes.

## 6.8 REISSNER-MINDLIN PLATE TRIANGLES

Most Reissner-Mindlin plate triangles have been developed using the assumed transverse shear strain methodology. Some popular elements are presented next.

### 6.8.1 6-noded quadratic triangle with assumed linear shear strains (TQQL)

Zienkiewicz *et al.* [ZTPO] developed a 6-noded plate triangle with a standard quadratic interpolation for the deflection and the rotations and the following assumed linear transverse shear strain field

$$\begin{aligned} \gamma_\xi &= \alpha_1 + \alpha_2 \xi + \alpha_3 \eta, \\ \gamma_\eta &= \alpha_4 + \alpha_5 \xi + \alpha_6 \eta, \end{aligned} \quad \text{i.e.} \quad \mathbf{A} = \begin{bmatrix} 1 & \xi & \eta & 0 & 0 & 0 \\ 0 & 0 & 0 & 1 & \xi & \eta \end{bmatrix} \quad (6.116)$$

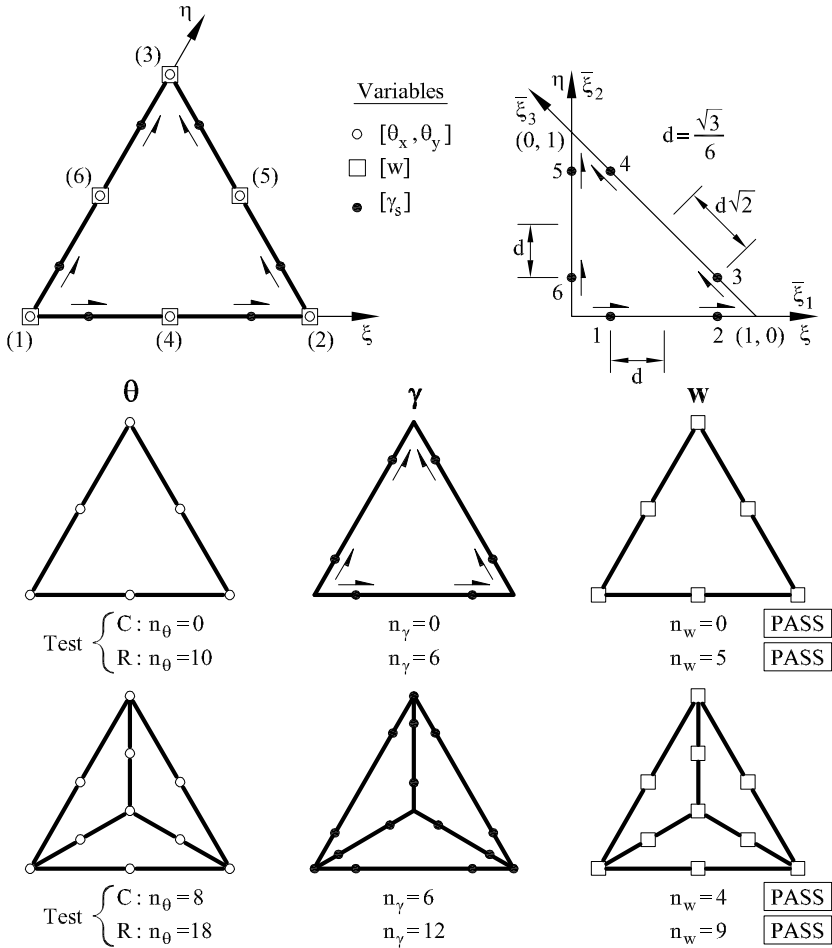


**Fig. 6.22** Eighteen DOFs TQQQ Reissner-Mindlin plate triangle ( $w$  Quadratic,  $\theta$  Quadratic,  $\gamma$ , Linear). Figures within brackets denote node numbers

Figure 6.22 shows the position of the six shear sampling points and the  $\bar{\xi}_i$  directions. Following the procedure of Section 6.6.3 we find

$$\mathbf{P} = \begin{bmatrix} 1 & \xi_1 & \eta_1 & 0 & 0 & 0 \\ 1 & \xi_2 & \eta_2 & 0 & 0 & 0 \\ -a & -a\xi_3 & -a\eta_3 & a & a\xi_3 & a\eta_3 \\ -a & -a\xi_4 & -a\eta_4 & a & a\xi_4 & a\eta_4 \\ 0 & 0 & 0 & 1 & \xi_5 & \eta_5 \\ 0 & 0 & 0 & 1 & \xi_6 & \eta_6 \end{bmatrix}; \mathbf{T} = \begin{bmatrix} 1 & 0 & & & & 0 \\ & 1 & 0 & & & \\ & & -a & a & & \\ & & & -a & a & \\ & & & & 0 & 1 \\ 0 & & & & & 0 & 1 \end{bmatrix}$$

$$\mathbf{C} = \begin{bmatrix} \mathbf{J}^1 & & & \mathbf{0} \\ & \mathbf{J}^2 & & \\ & & \ddots & \\ \mathbf{0} & & & \mathbf{J}^6 \end{bmatrix}, \quad \hat{\mathbf{B}}_s = \begin{Bmatrix} \mathbf{B}^1 \\ \mathbf{B}^2 \\ \vdots \\ \mathbf{B}^6 \end{Bmatrix}, \quad a = \frac{\sqrt{2}}{2} \quad (6.117)$$

Matrix  $\bar{\mathbf{B}}_s$  is computed by Eq.(6.81). A full 3-point Gauss quadrature is used for the numerical integration of  $\mathbf{K}_s^{(e)}$ .

This element was termed TRI-6R in [ZTPO] and T6D6 in [ZT2]. In our notation we call it TQQL (for **T**riangle, **Q**uadratic deflection, **Q**uadratic rotation and **L**inear transverse shear strain fields). The element satisfies conditions (6.61) for all meshes (Figure 6.22).

The TQQL element performs well although sometimes is too flexible [ZTPO,ZT2]. Improvements are found by imposing a linear variation for the normal rotation  $\theta_n$  along the three sides as

$$\theta_{n_i} - \frac{1}{2}(\theta_{n_{i-2}} + \theta_{n_{i+2}}) = 0 \quad (6.118)$$

where  $i = 4, 5, 6$  are the mid-side nodes (Figure 6.22).

Eq.(6.118) can be used for eliminating the normal rotation at the mid-side nodes [OC,ZTPO]. Conditions (6.61) still hold in this case. A plate triangle based on this concept is presented next.

### 6.8.2 Quadratic/Linear Reissner–Mindlin plate triangle (TLQL)

Zienkiewicz *et al.* [ZTPO], Papadopoulos and Taylor [PT] and Oñate *et al.* [OC,OTZ,OZBT] developed very similar enhanced versions of the TQQL element of previous section. The basic assumptions are

1. The deflection varies linearly as:

$$w = \sum_{i=1}^3 N_i w_i \quad (6.119)$$

2. A incomplete quadratic interpolation is used for the rotations:

$$\boldsymbol{\theta} = \sum_{i=1}^3 N_i \boldsymbol{\theta}_i + 4N_1 N_2 \mathbf{e}_{12} \Delta\theta_{s_4} + 4N_2 N_3 \mathbf{e}_{23} \Delta\theta_{s_5} + 4N_1 N_3 \mathbf{e}_{13} \Delta\theta_{s_6} \quad (6.120)$$

3. The transverse shear strains vary linearly within the element in terms of the three shear strain  $\gamma_s$  at the element mid-side points. This defines a constant shear strain along each side.

In above expressions  $N_i$  are the standard linear shape functions for the 3-noded triangle,  $\Delta\theta_{s_i}$  is a hierarchical tangential rotation at the mid-side points and  $\mathbf{e}_{ij}$  are unit vectors along the side directions (Figure 6.23). Eq.(6.120) defines a linear variation for the normal rotation along the sides, while the tangential rotation varies quadratically. This is equivalent to imposing condition (6.118) explicitly. The vector of nodal variables is

$$\mathbf{a}^{(e)} = [w_1, \theta_{x_1}, \theta_{y_1}, w_2, \theta_{x_2}, \theta_{y_2}, w_3, \theta_{x_3}, \theta_{y_3}, \Delta\theta_{s_1}, \Delta\theta_{s_1}, \Delta\theta_{s_3}]^T \quad (6.121)$$

This element was termed DRM in [ZTPO] and T3T3 in [ZT]. Here it is called TLQL (for **T**riangle, **L**inear deflection, **Q**uadratic rotations and **L**inear transverse shear strain fields). The TLQL element satisfies conditions (6.61), for all meshes (Figure 6.23). It can be considered the triangular counterpart of the QLQL quadrilateral of Section 6.7.4. Matrix  $\bar{\mathbf{B}}_s$  can be derived by constraining the quadratic shear strain field of the TQQL element. A more direct procedure is to write the assumed linear shear strain field in the natural coordinate system as [OZBT]

$$\boldsymbol{\gamma}' = \begin{Bmatrix} \gamma_\xi \\ \gamma_\eta \end{Bmatrix} = \begin{bmatrix} 1 - \eta - \sqrt{2}\eta & \eta \\ \xi & \sqrt{2}\xi & 1 - \xi \end{bmatrix} \begin{Bmatrix} \gamma_\xi^{12} \\ \gamma_\xi^{23} \\ \gamma_\xi^{13} \end{Bmatrix} = [A^{-1}PT]\boldsymbol{\gamma}_\xi \quad (6.122)$$

where  $\boldsymbol{\gamma}_\xi^{ij} = [\gamma_\xi^{12}, \gamma_\xi^{23}, \gamma_\xi^{13}]^T$  contains the local shear strains at the element mid-side points. The signs in Eq.(6.122) correspond to the side coordinates  $\bar{\xi}_1, \bar{\xi}_2$  and  $\bar{\xi}_3$  as defined in Figure 6.23.

The relationship between the shear strains and the nodal displacements is obtained by imposing the condition  $\gamma_\xi^{ij} = \left(\frac{\partial w}{\partial \bar{\xi}} - \theta_s\right)$  to be satisfied along each side in a weighted residual form, similarly as explained in step 5 of Section 6.6.3. Thus, we write

$$\int_{l^{ij}} W_k \left[ \gamma_\xi^{ij} - \frac{\partial w}{\partial \bar{\xi}} + \theta_s \right] d\bar{\xi} = 0 \quad (6.123)$$

where  $l^{ij}$  is the length of the side  $ij$ .

Choosing a Galerkin weighting with  $W_k = 1$  [ZTZ] and assuming that  $\gamma_\xi^{ij}$  is constant along each side leads, after substituting Eqs.(6.119) and

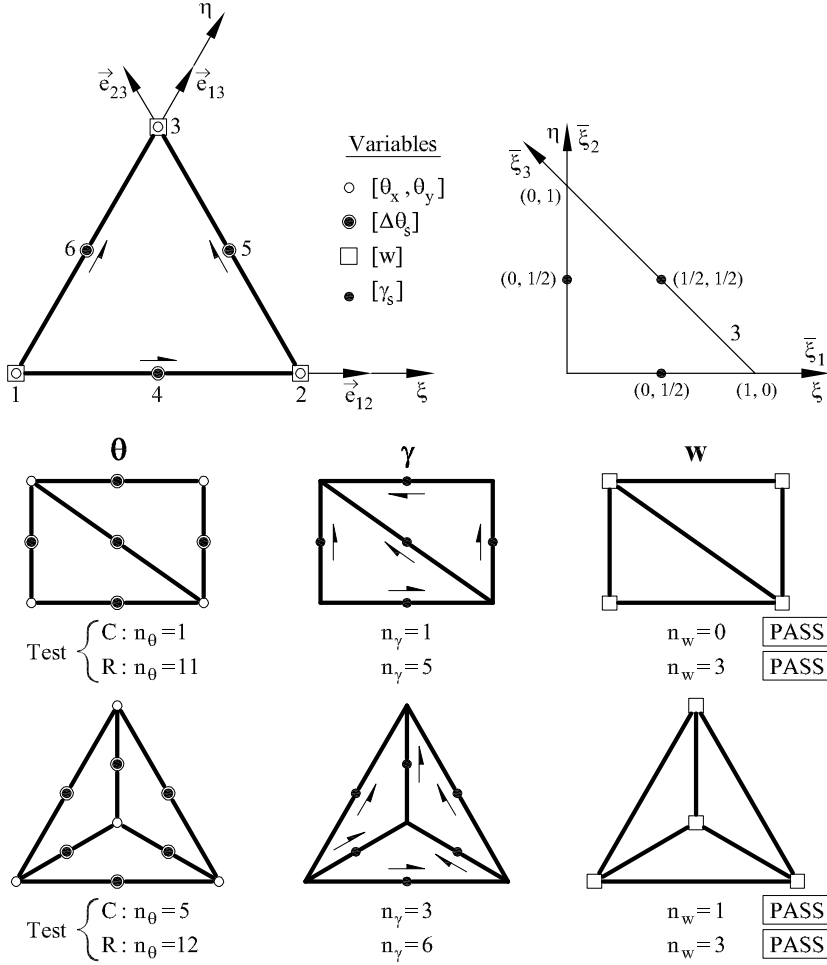


**Fig. 6.23** Twelve DOFs TLQL Reissner-Mindlin plate triangle ( $w$  Linear,  $Q$  Quadratic,  $\gamma$  Linear)

(6.120) into (6.123), to the following equation for each side

$$\gamma_{\bar{\xi}}^{ij} = \frac{1}{l_{\bar{\xi}}^{ij}} \int_{l_{\bar{\xi}}} \left( \frac{\partial w}{\partial \bar{\xi}} - \theta_{\bar{\xi}} \right) d\bar{\xi} = \frac{1}{l_{\bar{\xi}}^{ij}} (w_j - w_i) - \frac{l_{\bar{\xi}}^{ij}}{2l_{\bar{\xi}}^{ij}} \mathbf{e}_{ij}^T (\boldsymbol{\theta}_i + \boldsymbol{\theta}_j) - \frac{2}{3} \Delta\theta_{s_k} \frac{l_{\bar{\xi}}^{ij}}{l_{\bar{\xi}}^{ij}} \quad (6.124)$$

where  $k = 3 + i$ ,  $l_{\bar{\xi}}^{12} = l_{\bar{\xi}}^{13} = 1$  and  $l_{\bar{\xi}}^{23} = \sqrt{2}$ . Vectors  $\mathbf{e}_{ij}$  are defined so that  $i$  and  $j$  coincide with the corner nodes with smaller and larger global numbers, respectively (Figure 6.23). From Eq.(6.124) we can write

$$\boldsymbol{\gamma}_{\bar{\xi}} = [TCB] \mathbf{a}^{(e)} \quad (6.125)$$

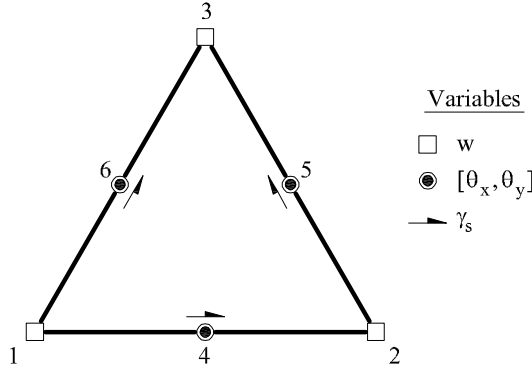


**Fig. 6.24** Nine DOFs TLLL Reissner-Mindlin plate triangle ( $w$  linear,  $\theta$  quadratic,  $\gamma$  linear) [OZF]

where

$$[TCB] = \begin{bmatrix} -1 & \frac{x_{12}}{2} & \frac{y_{12}}{2} & 1 & \frac{x_{12}}{2} & \frac{y_{12}}{2} & 0 & 0 & 0 & -\frac{2}{3}l^{12} & 0 & 0 \\ 0 & 0 & 0 & -\frac{1}{\sqrt{2}} & \frac{x_{23}}{\sqrt{2}} & \frac{y_{23}}{\sqrt{2}} & \frac{1}{\sqrt{2}} & \frac{x_{23}}{\sqrt{2}} & \frac{y_{23}}{\sqrt{2}} & 0 & -\frac{\sqrt{2}}{3}l^{23} & 0 \\ 1 & -\frac{\bar{C}_{13}}{2} & -\frac{\bar{S}_{13}}{2} & 0 & 0 & 0 & -1 & -\frac{\bar{C}_{13}}{2} & -\frac{\bar{S}_{13}}{2} & 0 & 0 & -\frac{2}{3}l^{13} \end{bmatrix} \quad (6.126)$$

with  $x_{ij} = x_i - x_j$  and  $y_{ij} = y_i - y_j$ . The substitute transverse shear strain matrix is

$$\bar{\mathbf{B}}_s = \mathbf{J}^{-1}[\mathbf{A}^{-1}PT][TCB] \quad (6.127)$$

where  $[\mathbf{A}^{-1}PT]$  is deduced from Eq.(6.122). A full 3 point quadrature is used and this prevents the element from having spurious mechanisms.

The TLQL element performs well and examples can be found in [OZBT] and in Section 6.11. The element yields linear bending moments and constant transverse shear distributions along the sides which satisfy the equilibrium conditions (5.23). This contributes to its good behaviour.

The three hierarchical tangential rotations  $\Delta\theta_{s_k}$  at the mid-side points can be eliminated by imposing a zero value of the transverse shear strain along the sides. This leads to the nine DOFs Discrete Kirchhoff thin plate triangle (DKT) described in Section 6.11.1.

### 6.8.3 Linear plate triangle with nine DOFs (TLLL)

Oñate *et al.* [OZF] proposed a low order Reissner-Mindlin plate triangle based on the following fields (Figure 6.24)

1. The deflection is linearly interpolated in terms of the three corner values by Eq.(6.119)
2. The rotations are linearly interpolated in terms of mid-side values by

$$\boldsymbol{\theta} = \sum_{i=4}^6 N_i^\theta \boldsymbol{\theta}_i; \quad \boldsymbol{\theta}_i = [\theta_{x_i}, \theta_{y_i}]^T \quad (6.128)$$

where

$$N_4^\theta = 1 - 2\eta, \quad N_s^\theta = 2\xi + 2\eta - 1, \quad N_6^\theta = 1 - 2\xi \quad (6.129a)$$

For convenience, we define the displacement vector as

$$\mathbf{a}^{(e)} = [w_1, w_2, w_3, \theta_{x_4}, \theta_{y_4}, \theta_{x_5}, \theta_{y_5}, \theta_{x_6}, \theta_{y_6}]^T \quad (6.129b)$$

Eq.(6.128) defines an incompatible rotation field with interelemental compatibility satisfied at the mid-side nodes only. The good performance of the element is ensured as the patch test is satisfied [OFZ].

3. A linear assumed transverse shear strain field is assumed identical to that of Eq.(6.122) for the TLQL element. The derivation of  $\bar{\mathbf{B}}_s$  follows the arguments of the preceding section with matrix  $[A^{-1}PT]$  deduced from Eq.(6.122) and matrix  $[TCB]$  given by

$$[TCB] = \begin{bmatrix} -1 & 1 & 0 & x_{12} & y_{12} & 0 & 0 & 0 & 0 \\ 0 & \frac{1}{\sqrt{2}} & \frac{1}{\sqrt{2}} & 0 & 0 & \frac{x_{23}}{\sqrt{2}} & \frac{x_{23}}{\sqrt{2}} & 0 & 0 \\ -1 & 0 & 1 & 0 & 0 & 0 & 0 & x_{13} & y_{13} \end{bmatrix} \quad (6.130)$$

A full 3 point quadrature is used.

The TLLL element (for **T**riangle and **L**inear interpolation for the deflection, the rotations and the transverse shear fields) satisfies conditions (6.61) and it is free from spurious mechanisms. Examples of its good behaviour can be found in Section 6.14.1 and [OFZ].

Flores and Oñate [FO2] have enhanced the behaviour of the TLLL element for plate and shell analysis by using a one-point reduced integration for the shear stiffness matrix. A stabilized method is used for eliminating the spurious energy modes induced by reduced integration.

The tangential side rotations can be eliminated by constraining the mid-side shear strains to be zero. This yields a six DOFs Discrete Kirchhoff thin plate triangle with identical features as the Morley triangle (Section 5.5.1) [On4].

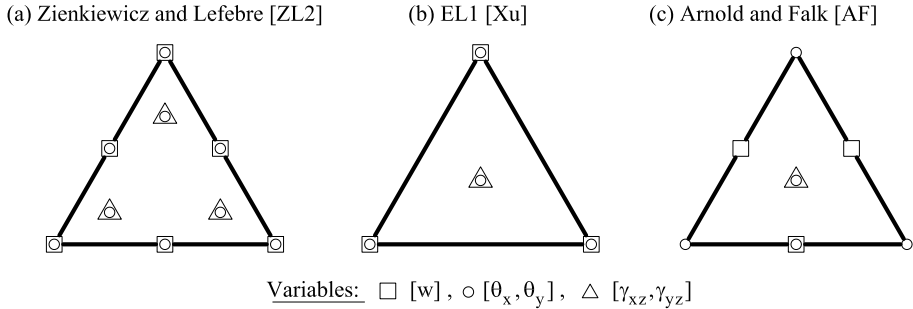


**Fig. 6.25** Reissner-Mindlin plate triangles based on assumed transverse shear strain fields

## 6.9 MORE PLATE TRIANGLES BASED ON ASSUMED SHEAR STRAIN FIELDS

Zienkiewicz and Lefebvre [ZL2] developed a quadratic triangle with a linear interpolation for the transverse shear strains. Three hierarchical quartic bubbles are added to the standard quadratic field giving a total of 24 DOFs (Figure 6.25a). Good performance is obtained by integrating  $\mathbf{K}_b$  and  $\mathbf{K}_s$  with seven and four point quadratures, respectively.

A linear triangle with an additional cubic bubble to the linear rotational interpolation and a constant shear field was developed by Xu [Xu] (Figure 6.25b). The original 9 DOFs element satisfies Eqs.(6.61) but it locks for very thin plates. The so-called EL1 element was enhanced using the concept of linked interpolation described in the next section [XZZ].

Arnold and Falk [AF] proposed a 9 DOFs plate triangle with an incomplete cubic interpolation for the rotations, a linear *discontinuous* deflection field and a constant transverse shear strain field (Figure 6.25c). The element performs reasonably well after eliminating the internal rotations [AF,Di]. However, the representation of the deflection field requires an adequate smoothing to avoid non-physical discontinuities.

Belytschko *et al.* [BSC] developed a 3-noded plate triangle by splitting the strain energy into bending and transverse shear modes. The bending mode is defined so that the bending energy coincides with that of an equivalent Kirchhoff mode with zero transverse shear strains. The rest of the element strain energy is associated to the transverse shear mode.

Hughes and Taylor [HT] proposed a 3-noded plate triangle based on a degeneration of a 4-noded quadrilateral with a linear transverse shear field. This element only works correctly with a reduced one point quadrature.



The stiffness matrix is then identical to that of the triangle proposed by Belytschko *et al.* [BSC].

The popularity of many of these elements has been limited by the difficulties for their extension to shell analysis. A review of Reissner-Mindlin plate elements can be found in [BD5, On3, Tu, ZT2].

## 6.10 REISSNER-MINDLIN PLATE ELEMENTS BASED ON LINKED INTERPOLATIONS

A different class of Reissner-Mindlin plate elements can be derived by using an interpolation for the deflection field of one order higher than for the rotations. This favours satisfying the thin plate conditions  $\theta_x = \frac{\partial w}{\partial x}$  and  $\theta_y = \frac{\partial w}{\partial y}$  in the thin limit. The concept is similar to that studied for Timoshenko beams in Section 2.8.2.

An effective procedure of this type is via “linked interpolations”, where the deflection field is enriched with additional higher order polynomial terms involving the nodal rotations (Section 2.8.3).

For the 3-noded linked triangle and the 4-noded linked quadrilateral we require that

1. The deflection field along a side is defined by the rotations at the end side nodes only, in order to guarantee  $C^0$  continuity;
2. The rotation terms must introduce quadratic expansions into the deflection field;
3. The transverse shear strains are constant along the sides.

The following interpolation satisfies above conditions

$$w = \sum_{j=1}^n N_j w_j + \frac{1}{8} \sum_{k=1}^{n_s} \bar{N}_k l_{kj} (\theta_{s_i} - \theta_{s_j}) \quad (6.131a)$$

$$\boldsymbol{\theta} = \sum_{j=1}^n N_j \boldsymbol{\theta}_j \quad (6.131b)$$

where  $N_i$  are the shape functions of the original element (with  $n = 3$  and  $n = 4$  for the linear triangle and the bilinear quadrilateral, respectively),  $n_s$  is the number of nodes along the element sides,  $l_{ij}$  is the length of side  $ij$ ,  $\theta_{s_i}$  and  $\theta_{s_j}$  are the rotations along the tangential directions to the  $k$ -th side with nodes  $i$  and  $j$  and  $\bar{N}_i$  are quadratic shape functions vanishing at the corner nodes.

For 3-noded triangles,

$$\bar{\mathbf{N}} = [\bar{N}_1, \bar{N}_2, \bar{N}_3] = 4[L_1L_2, L_2L_3, L_3L_1] \quad (6.132a)$$

For 4-noded quadrilaterals,

$$\begin{aligned} \bar{\mathbf{N}} = [\bar{N}_1, \bar{N}_2, \bar{N}_3, \bar{N}_4] = \frac{1}{2} [(1 - \xi^2)(1 - \eta), (1 - \xi)(1 - \eta^2), \\ (1 - \xi^2)(1 + \eta), (1 - \xi)(1 + \eta^2)] \end{aligned} \quad (6.132b)$$

The tangential rotations  $\theta_{s_i}$  are expressed in terms of the cartesian components at each node. For side  $ij$

$$\theta_{s_i} = \theta_{x_i} \cos \phi_{ij} + \theta_{y_i} \sin \phi_{ij} \quad (6.133)$$

where  $\phi_{ij}$  is the angle that side  $ij$  forms with the  $x$  axis. Substituting Eq.(6.133) into (6.131a) yields the deflection field in terms of the deflection and the two cartesian rotations at the corner nodes.

For a 4-noded rectangle Eq.(6.131a) takes the following form for side 12 with  $\eta = -1$

$$w = \frac{1}{2}(1 - \xi)w_1 + \frac{1}{2}(1 + \xi)w_2 + (1 - \xi^2)\frac{l_{12}}{8}(\theta_{s_1} - \theta_{s_2}) \quad (6.134)$$

Eqs.(6.134) and (6.131b) guarantee a constant shear distribution along the side. Assuming a rectangular shape with  $s = \xi = x$  gives for side 12

$$\gamma_{xz} = \frac{\partial w}{\partial x} - \theta_x = \frac{w_2 - w_1}{l_{12}} - \frac{\theta_{x_1} + \theta_{x_2}}{2} \quad (6.135)$$

and  $\gamma_{yz} = 0$ . A similar result is obtained for the three other sides. Note the analogy with the process of Section 2.8.3 for Timoshenko beams.

The linked interpolation introduces bending moments in the equivalent nodal force vector for a distributed loading, similarly as for linked beam elements (Section 2.8.3).

Linear and quadratic plate triangles based on linked interpolations have been derived by Tessler [Te], Tessler and Hughes [TH], Xu *et al.* [XZZ], Lynn *et al.* [GL,LD], Aurichio and Lodavina [AL] and Taylor *et al.* [AT2,PT,TA]. Linked plate quadrilaterals have been proposed by Crisfield [Cr], Aurichio and Taylor [AT] and Zienkiewicz *et al.* [ZXZ+].

A different strategy for deriving Reissner-Mindlin plate elements based on a sort of linked interpolation is by starting from the analytical solution for a Timoshenko beam [ZT2]. Different interesting shear-locking free 3-noded triangles and 4-noded quadrilaterals of this kind for thick/thin plate analysis have been proposed [ChC4,ChC5,Ib,SLC,SCLL,ZK].

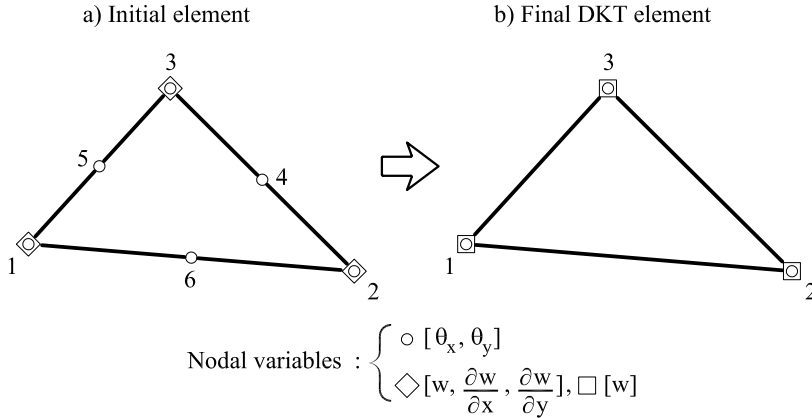


**Fig. 6.26** 3-noded DKT plate element

## 6.11 DISCRETE-KIRCHHOFF PLATE ELEMENTS

A family of thin plate elements can be derived by imposing the Kirchhoff constraints ( $\gamma_{xz} = \gamma_{yz} = 0$ ) at selected points within a Reissner-Mindlin element so that the transverse shear strain energy is effectively zero.

The so-called Discrete-Kirchhoff (DK) plate elements were originally proposed by Wempner *et al.* [WOK], Stricklin *et al.* [SHTG] and Dhatt [Dh,Dh2] as early as in 1968-70 as a way for overcoming the  $C^1$  continuity limitations of Kirchhoff plate theory. Several DK plate and shell elements were subsequently developed [BD5,6,BRI,Cr,Cr3,DMM], the most successful ones being the 3-noded DK triangle (DKT) detailed in the next section and the “semi-loop” shell element [IA,Ir2] (Section 7.12.5). The derivation of DK elements can be viewed as a particular class of assumed transverse shear strain techniques, leading to the vanishing of the transverse shear strain energy over the element. A state of the art on DK plate elements is presented in [BD3].

### 6.11.1 3-noded DK plate triangle (DKT)

The DKT element was initially developed by Stricklin *et al.* [SHTG] and subsequently modified by Dhatt [Dh,Dh2] and Batoz *et al.* [Bat,BBH,BD5] who analyzed its performance extensively.

The starting point is the 6-noded Reissner-Mindlin triangle of Figure 6.26a under the following constraints:

1. The rotations  $\theta_x$  and  $\theta_y$  vary quadratically over the element (12 DOFs).

2. The deflection varies as a cubic Hermite polynomial along each side  $ij$  in terms of  $w_i, \left(\frac{\partial w}{\partial s}\right)_i, w_j, \frac{\partial w}{\partial s_j}$ . After transformation, this gives a total of 9 DOFs ( $w, \frac{\partial w}{\partial x}$  and  $\frac{\partial w}{\partial y}$  at each corner node).
3. A linear variation for the normal rotation  $\theta_n$  is imposed along each side.
4. The conditions of zero transverse shear strain are imposed:
  - a) at the corner nodes ( $\gamma_{xz} = \gamma_{yz} = 0$ )
  - b) at the mid-side nodes ( $\gamma_{sz} = \frac{\partial w}{\partial s} + \theta_s = 0$ ).
5. Only the contribution of the bending terms is taken into account for computing the element stiffness matrix, i.e.  $\mathbf{K}^{(e)} = \mathbf{K}_b^{(e)}$ .

Conditions 3 and 4 impose twelve constraints which allow us to eliminate the slopes  $\frac{\partial w}{\partial x}$  and  $\frac{\partial w}{\partial y}$  at the corner nodes and the rotations  $\theta_n$  and  $\theta_s$  at the mid-side nodes. The rotation field is finally expressed in terms of the standard nine nodal DOFs as

$$\begin{Bmatrix} \theta_x \\ \theta_y \end{Bmatrix} = \begin{bmatrix} N_{x1}, N_{x2}, N_{x3}, N_{x4}, N_{x5}, N_{x6}, N_{x7}, N_{x8}, N_{x9} \\ N_{y1}, N_{y2}, N_{y3}, N_{y4}, N_{y5}, N_{y6}, N_{y7}, N_{y8}, N_{y9} \end{bmatrix} \mathbf{a}^{(e)} \quad (6.136)$$

where

$$\mathbf{a}^{(e)} = [w_1, \theta_{x1}, \theta_{y1}, w_2, \theta_{x2}, \theta_{y2}, w_3, \theta_{x3}, \theta_{y3}]^T \quad (6.137)$$

is the nodal displacement vector. The shape functions  $N_{x_i}$  and  $N_{y_i}$  are shown in Box 6.1.

Eq.(6.136) allows us to obtain the bending strain matrix  $\mathbf{B}_b$  from which the element stiffness matrix can be exactly computed using a 3 point quadrature. The bending moments are sampled at the quadrature points.

Batoz [Bat,BD5] derived an explicit form for the stiffness matrix of the DKT element. First the matrix is evaluated in the local axes  $\bar{x}, \bar{y}$  of [Figure 6.27](#)

$$\bar{\mathbf{K}}^{(e)} = \frac{1}{\mathbf{A}^{(e)}} \mathbf{Q} \mathbf{S} \quad (6.138)$$

Matrices  $\mathbf{Q}$  and  $\mathbf{S}$  are shown in [Figure 6.28](#). The global stiffness matrix is obtained by

$$\mathbf{K}_{ij}^{(e)} = \mathbf{T}^T \bar{\mathbf{K}}_{ij}^{(e)} \mathbf{T} \quad \text{with} \quad \mathbf{T} = \begin{bmatrix} 1 & 0 & 0 \\ 0 & -\sin \alpha & \cos \alpha \\ 0 & -\cos \alpha & -\sin \alpha \end{bmatrix} \quad (6.139)$$

The bending moments are obtained at any element point by

$$\hat{\sigma}_b = \frac{1}{2\mathbf{A}^{(e)}} \hat{\mathbf{D}}_b \mathbf{N}_3 \mathbf{S} \mathbf{a}^{(e)} \quad (6.140)$$

$$\begin{Bmatrix} \theta_x \\ \theta_y \end{Bmatrix} = \sum_{i=1}^3 \begin{bmatrix} N_{x_i} & N_{x_{i+1}} & N_{x_{i+2}} \\ N_{y_i} & N_{y_{i+1}} & N_{y_{i+2}} \end{bmatrix} \begin{Bmatrix} w_i \\ \theta_{x_i} \\ \theta_{y_i} \end{Bmatrix}$$

$$\begin{aligned} N_{x_1} &= 1.5(a_6 N_6 - a_5 N_5) & ; & & N_{x_2} &= b_5 N_5 + b_6 N_6 & & N_{x_3} &= N_1 - c_5 N_5 - c_6 N_6 \\ N_{x_4} &= 1.5(a_4 N_4 - a_6 N_6) & ; & & N_{x_5} &= b_6 N_6 + b_4 N_4 & & N_{x_6} &= N_2 - c_4 N_4 - c_6 N_6 \\ N_{x_7} &= 1.5(a_5 N_5 - a_4 N_4) & ; & & N_{x_8} &= b_4 N_4 + b_5 N_5 & & N_{x_9} &= N_3 - c_4 N_4 - c_5 N_5 \\ N_{y_1} &= 1.5(d_6 N_6 - d_5 N_5) & ; & & N_{y_2} &= -N_1 + e_5 N_5 + e_6 N_6 & ; & N_{y_3} &= -N_{x_2} \\ N_{y_4} &= 1.5(d_4 N_4 - d_6 N_6) & ; & & N_{y_5} &= -N_2 + e_4 N_4 + e_6 N_6 & ; & N_{y_6} &= -N_{x_5} \\ N_{y_7} &= 1.5(d_5 N_5 - d_4 N_4) & ; & & N_{y_8} &= -N_3 + e_4 N_4 + e_5 N_5 & ; & N_{y_9} &= -N_{x_8} \end{aligned}$$

$$a_k = -\frac{x_{ij}}{l_{ij}^2} \quad ; \quad b_k = \frac{3}{4l_{ij}^2} x_{ij} y_{ij} \quad \quad c_k = \left( \frac{1}{4} x_{ij}^2 - \frac{1}{2} y_{ij}^2 \right) / l_{ij}^2$$

$$d_k = -\frac{y_{ij}}{l_{ij}^2} \quad ; \quad l_k = \left( \frac{1}{4} y_{ij}^2 - \frac{1}{2} x_{ij}^2 \right) / l_{ij}^2 \quad ; \quad l_{ij}^2 = (x_{ij}^2 + y_{ij}^2)$$

$x_{ij} = x_i - x_j$ ,  $y_{ij} = y_i - y_j$ ,  $k = 4, 5, 6$  for sides  $ij = 23, 31, 12$ .

$N_i$  = shape functions of the 6-noded quadratic triangle (Appendix I)

### Box 6.1 Shape functions for the DKT element

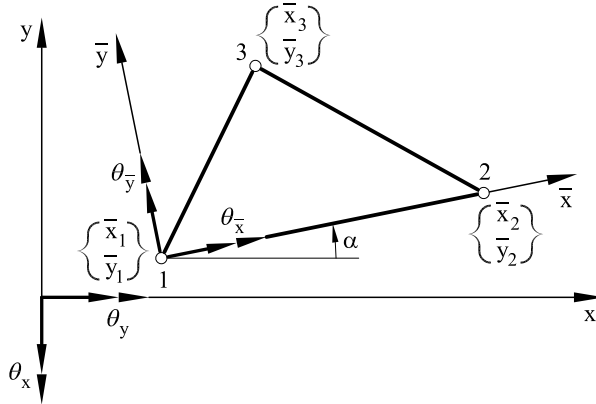


**Fig. 6.27** Sign convention for rotations and local axes for computing the stiffness matrix for the DKT plate element. Note the vectorial definition of rotations

where  $\mathbf{N}_3$  is the linear shape function matrix for the 3-noded triangle [Bat,BD5]. Figure 6.28 shows the explicit form for the local stiffness matrix of the DKT element.

### Alternative derivation of the DKT element

We present an alternative procedure for deriving a DKT element with identical features to that of the previous section. The starting point is the TLQL element of Section 6.8.2. The transverse shear strain is made zero

$$\bar{\mathbf{K}}^{(e)} = \frac{1}{2\mathbf{A}^{(e)}} \mathbf{Q} \mathbf{S}$$

$$\mathbf{Q} = \frac{1}{24} \begin{bmatrix} (\hat{d}_{11}^T \mathbf{S}_{11}^T + \hat{d}_{12}^T \mathbf{S}_{21}^T) \mathbf{R} & | & (\hat{d}_{12}^T \mathbf{S}_{11}^T + \hat{d}_{22}^T \mathbf{S}_{21}^T) \mathbf{R} & | & \hat{d}_{33}^T \mathbf{S}_{31}^T \mathbf{R} \\ (\hat{d}_{11}^T \mathbf{S}_{12}^T + \hat{d}_{12}^T \mathbf{S}_{22}^T) \mathbf{R} & | & (\hat{d}_{12}^T \mathbf{S}_{12}^T + \hat{d}_{22}^T \mathbf{S}_{22}^T) \mathbf{R} & | & \hat{d}_{33}^T \mathbf{S}_{32}^T \mathbf{R} \\ (\hat{d}_{11}^T \mathbf{S}_{13}^T + \hat{d}_{22}^T \mathbf{S}_{23}^T) \mathbf{R} & | & (\hat{d}_{12}^T \mathbf{S}_{13}^T + \hat{d}_{12}^T \mathbf{S}_{23}^T) \mathbf{R} & | & \hat{d}_{33}^T \mathbf{S}_{33}^T \mathbf{R} \end{bmatrix}; \quad \mathbf{R} = \begin{bmatrix} 2 & 1 & 1 \\ 1 & 2 & 1 \\ 1 & 1 & 2 \end{bmatrix}$$

$$\mathbf{S} = \begin{bmatrix} 6\bar{y}_3 a_6 & 0 & -4\bar{y}_3 & : & -6\bar{y}_3 a_6 & 0 & -2\bar{y}_3 & : & 0 & 0 & 0 \\ -6\bar{y}_3 a_6 & 0 & 2\bar{y}_3 & : & 6\bar{y}_3 a_6 & 0 & 4\bar{y}_3 & : & 0 & 0 & 0 \\ \bar{y}_3 p_5 & -\bar{y}_3 q_5 & \bar{y}_3(2-r_5) & : & 6\bar{y}_3 a_4 & 4\bar{y}_3 b_4 & \bar{y}_3(r_4-2) & : & -\bar{y}_3(6a_4+p_5) & \bar{y}_3(4b_4-q_5) & \bar{y}_3(r_4-r_5) \\ \dots & \dots & \dots & : & \dots & \dots & \dots & : & \dots & \dots & \dots \\ -\bar{x}_2 t_5 & \bar{x}_{23} + \bar{x}_2 r_5 & -\bar{x}_2 q_5 & : & 0 & \bar{x}_3 & 0 & : & \bar{x}_2 t_5 & \bar{x}_2(r_5-1) & \bar{x}_2 q_5 \\ 0 & \bar{x}_{23} & 0 & : & 6\bar{x}_2 d_4 & \bar{x}_3 + \bar{x}_2 r_4 & -4\bar{x}_2 b_4 & : & 6\bar{x}_2 d_4 & \bar{x}_2(r_4-1) & -4\bar{x}_2 b_4 \\ \bar{x}_{23} t_5 & \bar{x}_{23}(1-r_5) & \bar{x}_{23} q_5 & : & -6\bar{x}_3 d_4 & \bar{x}_3(1-r_4) & 4\bar{x}_3 b_4 & : & \begin{pmatrix} -\bar{x}_{23} t_5 \\ +6\bar{x}_3 d_4 \end{pmatrix} & \begin{pmatrix} -\bar{x}_{23} r_5 - \bar{x}_3 r_4 \\ -\bar{x}_2 \end{pmatrix} & 4\bar{x}_3 b_4 + \bar{x}_{23} q_5 \\ \dots & \dots & \dots & : & \dots & \dots & \dots & : & \dots & \dots & \dots \\ \begin{pmatrix} -6\bar{x}_3 a_6 \\ -\bar{x}_2 p_5 \end{pmatrix} & (\bar{x}_2 q_5 + y_3) & \begin{pmatrix} -4\bar{x}_{23} \\ +\bar{x}_2 r_5 \end{pmatrix} & : & 6\bar{x}_3 a_6 & -\bar{y}_3 & 2\bar{x}_3 & : & \bar{x}_2 p_5 & \bar{x}_2 q_5 & (r_5-2)\bar{x}_2 \\ -6\bar{x}_{23} a_6 & \bar{y}_3 & 2\bar{x}_{23} & : & \begin{pmatrix} 6\bar{x}_{23} a_6 \\ +6\bar{x}_2 a_4 \end{pmatrix} & -(\bar{y}_3 + 4\bar{x}_2 b_4) & (-4\bar{x}_3 + \bar{x}_2 r_4) & : & -6\bar{x}_2 a_4 & 4\bar{x}_2 b_4 & (r_4-2)\bar{x}_2 \\ \begin{pmatrix} \bar{x}_{23} p_5 \\ +\bar{y}_3 t_5 \end{pmatrix} & \begin{pmatrix} -\bar{x}_{23} p_5 \\ +(1-r_5)\bar{y}_3 \end{pmatrix} & \begin{pmatrix} (2-r_5)\bar{x}_{23} \\ +\bar{y}_3 q_5 \end{pmatrix} & : & \begin{pmatrix} 6\bar{x}_3 q_4 \\ -6\bar{y}_3 d_4 \end{pmatrix} & \begin{pmatrix} (r_4-1)\bar{y}_3 \\ -4\bar{x}_3 b_4 \end{pmatrix} & \begin{pmatrix} (2-r_4)\bar{x}_3 \\ -4\bar{y}_3 b_4 \end{pmatrix} & : & \begin{pmatrix} -\bar{x}_{23} q_5 \\ -4\bar{x}_3 b_4 \\ +(r_4-r_5)\bar{y}_3 \end{pmatrix} & \begin{pmatrix} \bar{x}_{23} r_5 \\ -\bar{x}_3 r_4 \\ +4\bar{x}_2 \\ +(q_5-4b_4)\bar{y}_3 \end{pmatrix} \end{bmatrix}$$

Fig. 6.28 Local stiffness matrix for the DKT element

$p_5 = -6x_3/l_{31}^2$ ,  $t_5 = -6y_3/l_{31}^2$ ,  $q_5 = 3x_3y_3/l_{31}^2$ ,  $r_4 = 3y_2^2/l_{23}^2$ ,  $r_5 = 3y_1^2/l_{31}^2$   
 $\bar{x}_i$ ,  $\bar{y}_i$  = local coordinates of node  $i$  ;  $\bar{x}_{ij}$ ,  $a_4$ ,  $a_6$ ,  $d_4$ ,  $b_4$  as in Box 6.1 changing  $\bar{x}_i$ ,  $\bar{y}_i$  for  $x_i$ ,  $y_i$ .

over the element by constraining the tangential transverse shear strains along the sides to a zero value. This allows us to eliminating the hierarchical tangential rotations at the mid-side nodes as

$$\gamma_{\xi}^{ij} = 0 \Rightarrow \Delta\theta_{s_k} = \frac{3}{2l^{ij}}(w_j - w_i) - \frac{3}{4}\mathbf{e}_{ij}(\boldsymbol{\theta}_i + \boldsymbol{\theta}_j) \quad (6.141)$$

Substituting Eq.(6.141) into (6.120) gives the new rotation field as

$$\boldsymbol{\theta} = \sum_{i=1}^3 \bar{\mathbf{N}}_i \mathbf{a}_i^{(e)} \quad ; \quad \mathbf{a}_i^{(e)} = \begin{Bmatrix} w_i \\ \theta_{x_i} \\ \theta_{y_i} \end{Bmatrix} \quad (6.142)$$

with

$$\begin{aligned} \bar{\mathbf{N}}_1 &= \left[ -\left( \frac{6L_1L_2}{l^{12}} \mathbf{e}_{12} + \frac{6L_1L_3}{l^{13}} \mathbf{e}_{23} \right), (L_1 - 3L_1L_2 - 3L_1L_3) \mathbf{I}_2 \right] \\ \bar{\mathbf{N}}_2 &= \left[ \left( \frac{6L_1L_2}{l^{12}} \mathbf{e}_{12} - \frac{6L_2L_3}{l^{23}} \mathbf{e}_{23} \right), (L_2 - 3L_1L_2 - 3L_2L_3) \mathbf{I}_2 \right] \\ \bar{\mathbf{N}}_3 &= \left[ \left( \frac{6L_2L_3}{l^{23}} \mathbf{e}_{23} + \frac{6L_1L_3}{l^{13}} \mathbf{e}_{13} \right), (L_3 - 3L_2L_3 - 3L_1L_3) \mathbf{I}_2 \right] \end{aligned} \quad (6.143)$$

where  $\mathbf{I}_2$  is the  $2 \times 2$  unit matrix.

The bending strain matrix  $\mathbf{B}_b$  is obtained by using the shape functions  $\bar{N}_i$  instead of  $N_i$  in Eq.(6.32). The bending stiffness matrix is computed with a 3 point quadrature.

Figures 6.27 and 6.28 show the performance of the DKT element for analysis of a clamped plate under point and uniform loads.

### 6.11.2 DK plate quadrilaterals

The first DK quadrilaterals were developed by Dhett and Venkatasubby [DV] and Baldwin *et al.* [BRI]. Later Irons proposed several DK plate and shell quadrilaterals [IA], among which the semi-loof [Ir2] has enjoyed big popularity (Section 7.12.5). Lyons [Ly], Crisfield [Cr,Cr2] and Batoz and Ben Tahar [BBt] have also derived DK plate quadrilaterals and some of these are displayed in Figure 6.29.

#### Derivation of a 4-noded DKQ element

The QLQL quadrilateral of Section 6.7.4 is starting point for deriving a 12 DOFs DK quadrilateral. The arguments follow as explained in the previous section for deriving a 3-noded DK triangle from the TLQL element. The

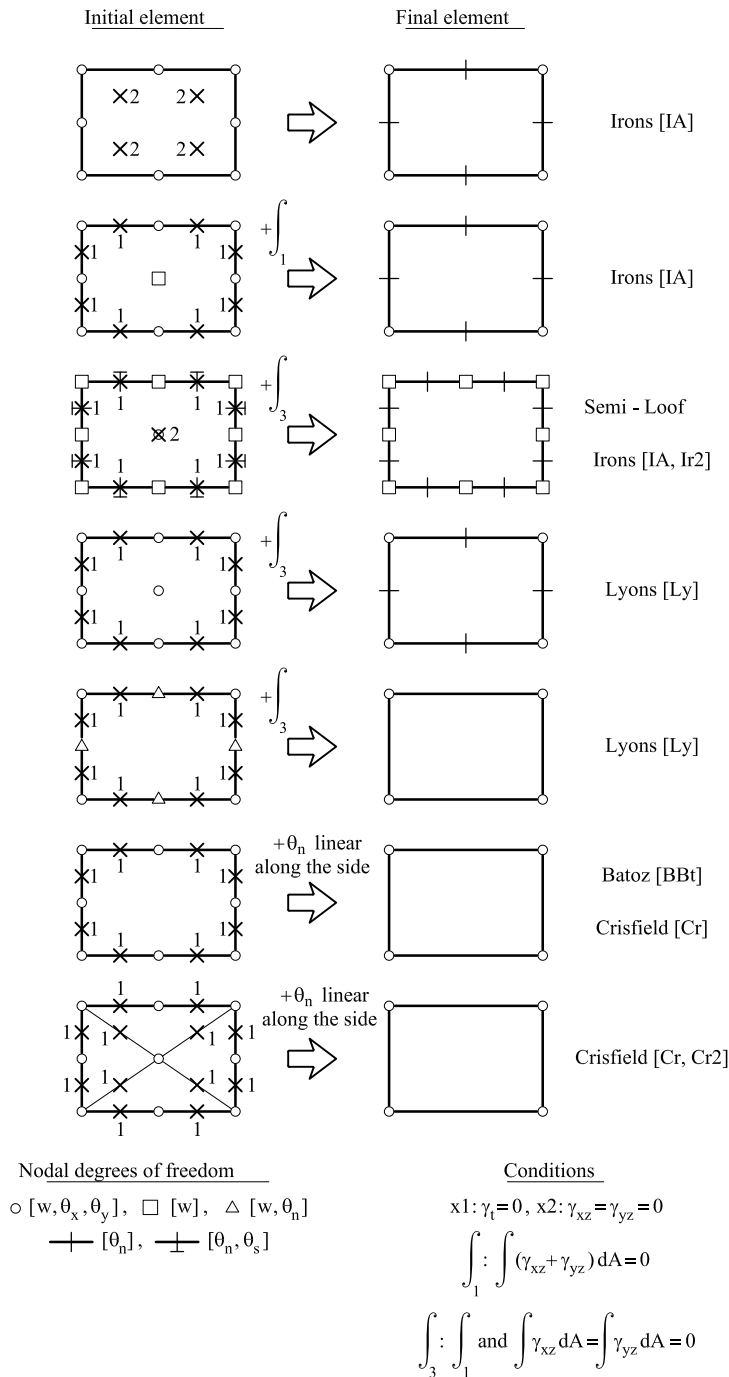


Fig. 6.29 Some DK plate quadrilaterals



constraint of vanishing transverse shear strain at the element sides (Figure 6.19) allows us to eliminate the four hierarchical tangential side rotations by an expression identical to Eq.(6.141). The final rotation field can be found substituting Eq.(6.141) into (6.105) to give

$$\boldsymbol{\theta} = \sum_{i=1}^4 \bar{\mathbf{N}}_i \mathbf{a}_i \quad \text{with} \quad \mathbf{a}_i = [w_i, \theta_{x_i}, \theta_{y_i}]^T \quad (6.144)$$

and  $\bar{\mathbf{N}}_i = [\bar{\mathbf{N}}_1, \bar{\mathbf{N}}_2, \bar{\mathbf{N}}_3, \bar{\mathbf{N}}_4]$  with

$$\begin{aligned} \bar{\mathbf{N}}_1 &= \left[ \left( -\frac{3}{4l^{12}} f(\xi)(1-\eta) \mathbf{e}_{12} - \frac{3}{4l^{14}} f(\eta)(1-\xi) \mathbf{e}_{14} \right), \left( N_1 - \frac{3}{8} f(\xi)(1-\eta) - \frac{3}{8} f(\eta)(1-\xi) \right) \mathbf{I}_2 \right] \\ \bar{\mathbf{N}}_2 &= \left[ \left( \frac{3}{4l^{12}} f(\xi)(1-\eta) \mathbf{e}_{12} - \frac{3}{4l^{23}} f(\eta)(1+\xi) \mathbf{e}_{23} \right), \left( N_2 - \frac{3}{8} f(\xi)(1-\eta) - \frac{3}{8} f(\eta)(1+\xi) \right) \mathbf{I}_2 \right] \\ \bar{\mathbf{N}}_3 &= \left[ \left( \frac{3}{4l^{43}} f(\xi)(1+\eta) \mathbf{e}_{43} + \frac{3}{4l^{23}} f(\eta)(1+\xi) \mathbf{e}_{23} \right), \left( N_3 - \frac{3}{8} f(\xi)(1+\eta) - \frac{3}{8} f(\eta)(1+\xi) \right) \mathbf{I}_2 \right] \\ \bar{\mathbf{N}}_4 &= \left[ \left( \frac{3}{4l^{14}} f(\eta)(1-\xi) \mathbf{e}_{14} - \frac{3}{4l^{43}} f(\eta)(1+\xi) \mathbf{e}_{43} \right), \left( N_4 - \frac{3}{8} f(\eta)(1-\xi) - \frac{3}{8} f(\xi)(1+\eta) \right) \mathbf{I}_2 \right] \end{aligned} \quad (6.145)$$

where  $f(\xi) = 1 - \xi^2$ ,  $f(\eta) = 1 - \eta^2$  and  $\mathbf{I}_2$  is the  $2 \times 2$  unit matrix.

Matrix  $\mathbf{B}_{b_i}$  is obtained using  $\bar{N}_i$  instead of  $N_i$  in Eq.(6.32). The bending stiffness matrix is computed with a  $2 \times 2$  quadrature.

The element is basically identical to that derived by Batoz and Ben Tahar [BBt]. Examples of its good performance can be found in [BBt,BD5].

## 6.12 DK ELEMENTS ACCOUNTING FOR SHEAR DEFORMATION EFFECTS: DST ELEMENT

Batoz and Lardeur [BL] presented an extension of the DKT element accounting for shear deformation effects. The starting point is the displacement field of the DKT element (Section 6.11.1). The fourth constraints on the transverse shear strains are modified as

4a) At the corner nodes 1, 2, 3

$$\frac{\partial w}{\partial x} - \theta_x = \gamma_{xz} \quad , \quad \frac{\partial w}{\partial y} - \theta_y = \gamma_{yz} \quad (6.146a)$$

4b) At the mid-side points 4, 5, 6

$$\left( \frac{\partial w}{\partial s} \right)_k + (\theta_s) = \gamma_{sz} = -S_k \gamma_{xz} + C_k \gamma_{yz} \quad k = 4, 5, 6 \quad (6.146b)$$

with  $S_k = \sin \phi_{ij}$ ,  $C_k = \cos \phi_{ij}$  where  $\phi_{ij}$  is the angle between the normal to the side  $ij$  and the  $x$  axis.

The transverse shear strains  $\gamma_{xz}$  and  $\gamma_{yz}$  are obtained from the equilibrium equations (Eqs.(5.23)) as

$$\begin{aligned}\gamma_{xz} &= \frac{Q_x}{\hat{D}_s} = -\frac{1}{\hat{D}_s} \left( \frac{\partial M_x}{\partial x} + \frac{\partial M_{xy}}{\partial y} \right) \\ \gamma_{yz} &= \frac{Q_y}{\hat{D}_s} = -\frac{1}{\hat{D}_s} \left( \frac{\partial M_y}{\partial y} + \frac{\partial M_{xy}}{\partial x} \right)\end{aligned}\quad (6.147)$$

Substituting the bending moments in terms of the rotations into Eq.(6.147) via Eqs.(6.22) and (6.9) gives

$$\begin{aligned}\bar{\gamma}_{xz} &= -\frac{\hat{D}_b}{\hat{D}_s} \left[ \frac{\partial^2 \theta_x}{\partial x^2} + \nu \frac{\partial \theta_y}{\partial x \partial y} + \frac{1-\nu}{2} \left( \frac{\partial^2 \theta_x}{\partial y^2} + \frac{\partial \theta_y}{\partial x \partial y} \right) \right] \\ \bar{\gamma}_{yz} &= -\frac{\hat{D}_b}{\hat{D}_s} \left[ \frac{\partial^2 \theta_y}{\partial y^2} + \nu \frac{\partial \theta_x}{\partial x \partial y} + \frac{1-\nu}{2} \left( \frac{\partial \theta_x}{\partial x \partial y} + \frac{\partial \theta_y}{\partial x^2} \right) \right]\end{aligned}\quad (6.148)$$

In the above  $\hat{D}_b = \frac{Et^3}{12(1-\nu^2)}$  and  $\hat{D}_s = kGt$ .

The nine conditions introduced by Eqs.(6.146), plus the three constraints imposed by prescribing a linear variation of  $\theta_n$  along the sides, allow us to eliminating the same twelve DOFs, similarly as for the DKT element. The rotation field is finally expressed as

$$\boldsymbol{\theta} = \mathbf{N}_\theta \mathbf{a}^{(e)} \quad , \quad \mathbf{a}^{(e)} = \begin{Bmatrix} \mathbf{a}_1^{(e)} \\ \mathbf{a}_2^{(e)} \\ \mathbf{a}_3^{(e)} \end{Bmatrix} \quad , \quad \mathbf{a}_i^{(e)} = \begin{Bmatrix} w_i \\ \theta_{x_i} \\ \theta_{y_i} \end{Bmatrix} \quad (6.149)$$

The bending and transverse shear matrices are deduced as

$$\hat{\boldsymbol{\varepsilon}}_b = \hat{\mathbf{B}}_b \mathbf{a}^{(e)} \quad \text{and} \quad \hat{\boldsymbol{\varepsilon}}_s = \hat{\mathbf{B}}_s \mathbf{a}^{(e)} \quad (6.150)$$

Matrices  $\mathbf{N}_\theta$ ,  $\hat{\mathbf{B}}_b$  and  $\hat{\mathbf{B}}_s$  can be found in [BD5,BL]. The stiffness matrix is obtained by adding the bending and transverse shear contributions, using  $\hat{\mathbf{B}}_b$  and  $\hat{\mathbf{B}}_s$  instead of  $\mathbf{B}_b$  and  $\mathbf{B}_s$  in Eqs. (6.39).

The DST element behaves well if the plate is moderately thin and transverse shear deformation effects are not very important. Its extension to shell analysis is possible but is not so simple [BD5].

Batoz and Katili [BK] derived an enhanced version of the DST element using constant bending modes plus incompatible energy orthogonal higher order bending modes. Katili [Ka2,3] proposed other simple triangular and quadrilateral elements for analysis of thick and thin plates obtained as an extension of the DKT and DKQ elements of previous sections.

## 6.13 PATCH TESTS FOR REISSNER-MINDLIN PLATE ELEMENTS

The absence of spurious modes in the element can be verified by computing the number of zero eigenvalues in excess of three in the stiffness matrix of a single unconstrained element. The procedure is the same as for assessing the mechanisms in plate elements induced by reduced and selective integration quadratures (Section 6.4.2). The absence of spurious modes and the good representation of rigid body motions can be assessed by imposing the following displacement field to the nodes laying on the boundary of a patch (patch test of type B, Section 4.9 and [On4])

$$w = c + ax + by \quad , \quad \theta_x = a \quad , \quad \theta_y = b \quad (6.151)$$

where  $a, b$  and  $c$  are arbitrary numbers. The numerical solution for the displacements at the internal node must agree with Eq.(6.151). Also the curvatures and the transverse shear strains must be zero everywhere in the patch.

A patch test can be devised for assessing the capability of Reissner-Mindlin plate elements to reproduce a pure bending state. The following displacement field is imposed to the boundary nodes of a type B patch

$$w = \frac{1}{2}(ax^2 + by^2 + cxy) \quad , \quad \theta_x = ax + \frac{1}{2}cxy \quad , \quad \theta_y = by + \frac{1}{2}cx \quad (6.152)$$

where  $a, b$  and  $c$  are arbitrary numbers. The solution for the internal nodal displacements must comply with Eq.(6.152). Also a constant curvature field  $\hat{\mathbf{e}}_b = [a, b, c]^T$  and a zero transverse shear strain field  $\hat{\mathbf{e}}_s = [0, 0]^T$  must be obtained everywhere in the patch.

A similar but less severe patch test is based in imposing the following displacement field

$$\begin{aligned} w &= 0 \quad \text{at all patch nodes} \\ \theta_x &= ax + \frac{1}{2}cy \quad , \quad \theta_y = by + \frac{1}{2}cx \end{aligned} \quad (6.153)$$

and  $\alpha = 0$  or very small in order to make  $\mathbf{K}_s$  a null matrix at each element. The numerical solution must satisfy the same conditions as for the previous test. These two tests are also applicable to DK plate elements.

The following displacement field can be imposed to the boundary nodes of a type B patch in order to verify the element ability to reproduce a

constant transverse shear strain field and a zero curvature field

$$w = \frac{1}{2}(ax + by) \quad , \quad \theta_x = \frac{-a}{2} \quad , \quad \theta_y = \frac{-b}{2} \quad (6.154)$$

Naturally, the displacements found at the internal nodes must be in accordance with Eqs.(6.154).

The stability of the element can be assessed via a patch test C (Section 4.9 of [On4]), i.e. by computing the rank of the stiffness matrix in element patches with the minimum number of DOFs prescribed. This test when applied to a single element is equivalent to the zero eigenvalue check mentioned above.

We note finally that the “count” inequalities of Eq.(6.61) are necessary conditions to be satisfied by plate elements based on assumed transverse shear strain fields. The kinematic patch tests described above are however mandatory to ascertain the good behaviour of the element.

## 6.14 EXAMPLES

### 6.14.1 Performance of some plate elements based on assumed transverse shear strain fields

The performance of some of the plate elements described in this chapter is studied first for the analysis of *a square plate* under a uniform load and a central point load. The analysis is performed for simple supported (SS) edges with hard support ( $w = \theta_s = 0$ ) and fully clamped edges. The material properties are  $E = 10.92$  and  $\nu = 0.3$  (units in the International System). The problem is solved for two values of the  $a/t$  ratio of  $\frac{a}{t} = 10$  (thick) and 100 (thin), where  $a$  and  $t$  are the plate side length and thickness, respectively. The elements studied are the QLLL (Section 6.7.1), QLQL (Section 6.7.4), TLQL (Section 6.8.2) and TLLL (Section 6.8.3). All problems were solved with uniform meshes in a quarter of the plate due to symmetry.

Results are compared with analytical and series values for the thin and thick cases when available [SG,SR,TW] or, alternatively, with FEM results for the deflection at the center of the middle plane obtained using a mesh of  $40 \times 40 \times 6$  8-noded hexahedra [On4] in a quarter of plate. *For the point load case the analytical value of the deflection under the load given by thick plate theory is infinity.* Hence, results for thick plates are compared at the mid-point along a central line in this case.

Figure 6.30 shows the convergence of the normalized values of the central and mid-side deflection for the QLLL and QLQL elements under point and uniform loads. Both elements converge well to the reference solutions for thick and thin situations.

Figure 6.31 shows similar results for the TLQL element for the two mesh orientations shown. Results are sensitive to the mesh orientation. This does not preclude the convergence of the element.

Figure 6.32 shows results for the same SS square plate obtained with the TLLL element for the SS (hard) case under uniform loading. The results plotted are the central deflection and the central bending moment. The performance is good for thick and thin situations and results are less sensitive to the mesh orientation than for the TLQL element.

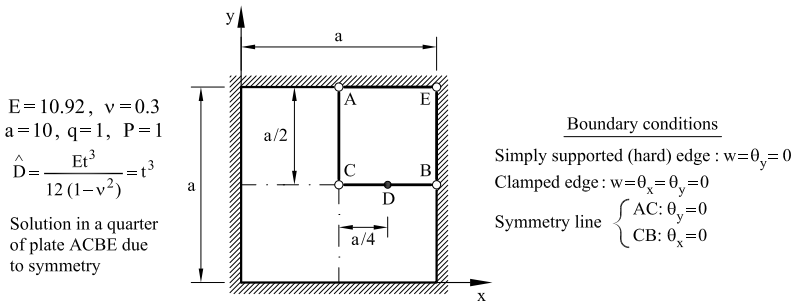
Figure 6.33 shows results for a *moderately thick clamped circular plate* using the TLQL, QLLL and QLQL elements. Graphics show the convergence of the deflection and the bending moment at the center toward the analytical solution (Appendix H and [BD5,TW]) and the distribution of the radial bending moment and the radial shear force along a radial line. All elements behave well. Note the accuracy of the QLLL element.

Table 6.3 shows results for the deflection and the bending moment at the center for thick and thin SS and clamped circular plates obtained with the TLLL element. The performance of this simple element is remarkably good with less than 10% error versus the reference solution for meshes of 64 elements in all cases.

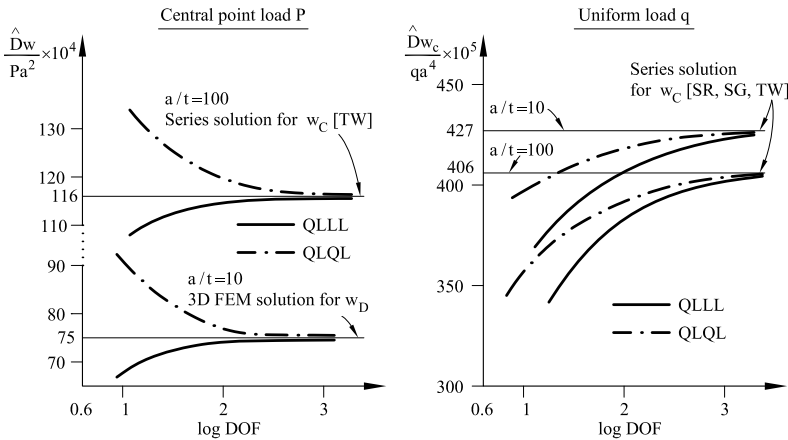
Note that in all cases the deflection for thick plates converges to larger values than those given by thin plate theory. The reason is the increased capacity of a Reissner-Mindlin plate to deform under external loads due to the shear deformation terms in the PVW.

Table 6.4 shows the convergence of the central deflection at the two free corners in *cantilever skew plates* under uniform load and different skew angles. Results obtained with the TLLL element are shown as well as those obtained with the DRM triangle [ZTPO,ZT2] (an equivalent of the TLQL of Section 6.8.2) and the EL1 triangle of Figure 6.25b for comparison purposes. The performance of the TLLL element is again noticeable.

More evidence of the good performance of the QLLL element can be found in [BD,OZST]. Results for the TLQL, QLQL and QQQQ elements are presented in [OZST]. The good behaviour of the TLLL element in its original and enhanced versions is studied in [FO,OZF].



SIMPLY SUPPORTED (HARD) SQUARE PLATE



CLAMPED SQUARE PLATE

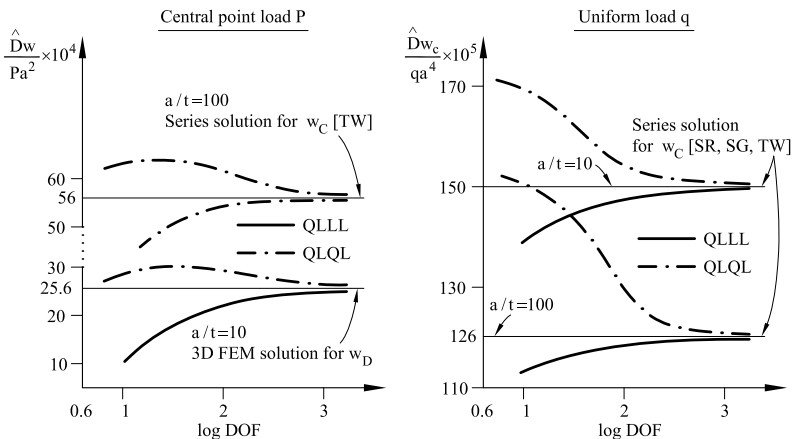


**Fig. 6.30** QLLL and QLQL elements. Square plate with SS (hard) and clamped edges under central point load and uniform load. Convergence of the deflection at the plate center  $C$  (uniform load and point load for  $a/t = 100$ ) and at a mid-side point  $D$  along a center line (point load for  $a/t = 10$ )

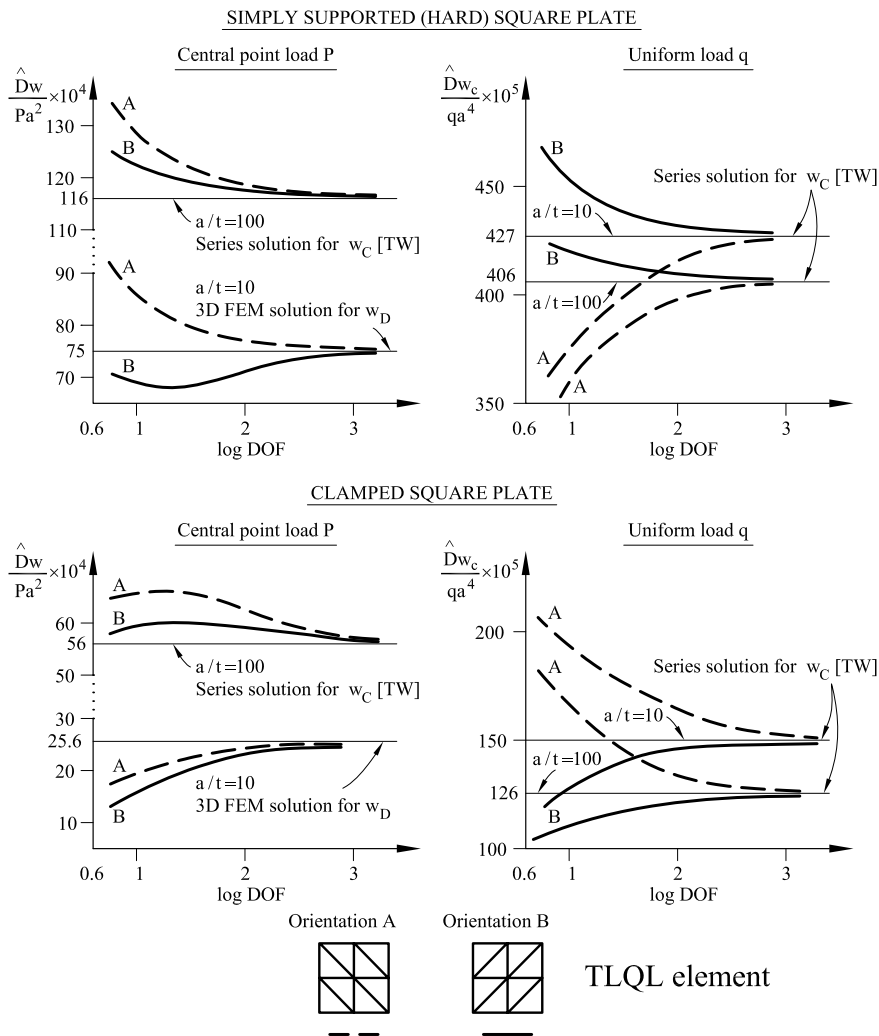


**Fig. 6.31** TLQL element. Square plate with SS (hard) and clamped edges under central point load and uniform load. Convergence of the deflection at the plate center  $C$  (uniform load and point load for  $a/t = 100$ ) and at a mid-side point  $D$  along a center line (point load for  $a/t = 10$ ) for two different thicknesses and two mesh orientations

**6.14.2 Simple supported plate under uniform load. Adaptive solution**

The next example is the analysis of a square plate with soft SS conditions ( $w = 0$ ) and uniform loading using adaptive mesh refinement (AMR) following the two AMR strategies explained in [OB] and in Section 9.9.4 of [On4]. [Figure 6.34](#) shows the geometry and material properties of the

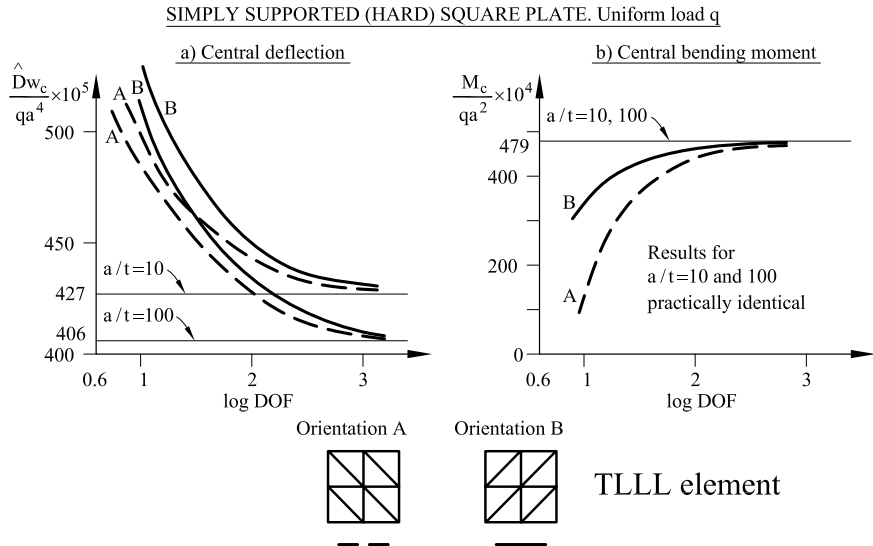


**Fig. 6.32** TLLL element. Square plate with SS (hard) edges under uniform loading. Convergence of central deflection and central bending moment for two different thicknesses and two mesh orientations

CIRCULAR PLATES. TLLL ELEMENT					
Elem.	DOF	$R/t = 10$		$R/t = 100$	
		$w_c \times 10^2$	$M_c^*$	$w_c \times 10^5$	$M_c^*$
Clamped circular plate					
4	12	3.7668	6.9599	3.6950	6.9606
16	54	2.2352	7.7235	2.1657	7.7431
64	220	1.7882	7.9751	1.7186	8.0146
144	498	1.7023	8.0243	1.6326	8.0726
225	780	1.6774	8.0391	1.6077	8.0904
Anal. (App. H)		1.6339	8.1250	1.5625	8.1250
SS circular plate (soft, $w = 0$ )					
4	17	7.2815	1.6400	7.2096	1.6402
16	62	6.7248	1.9427	6.6553	1.9449
64	236	6.5191	2.0279	6.4495	2.0319
144	522	6.4763	2.0437	6.4066	2.0487
225	810	6.4637	2.0484	6.3939	2.0536
Anal. (App. H)		6.4416	2.0625	6.3702	2.0625

\*Clamped plate:  $M_c^* = M_c$  ; SS plate:  $M_c^* = M_c \times 10$

**Table 6.3** TLLL element. Convergence of central deflection and central bending moment ( $M_{x_c} = M_{y_c} = M_c$ ) for thick and thin situations in clamped and SS (soft) circular plates under uniform load. Material properties as in [Figure 6.33](#)



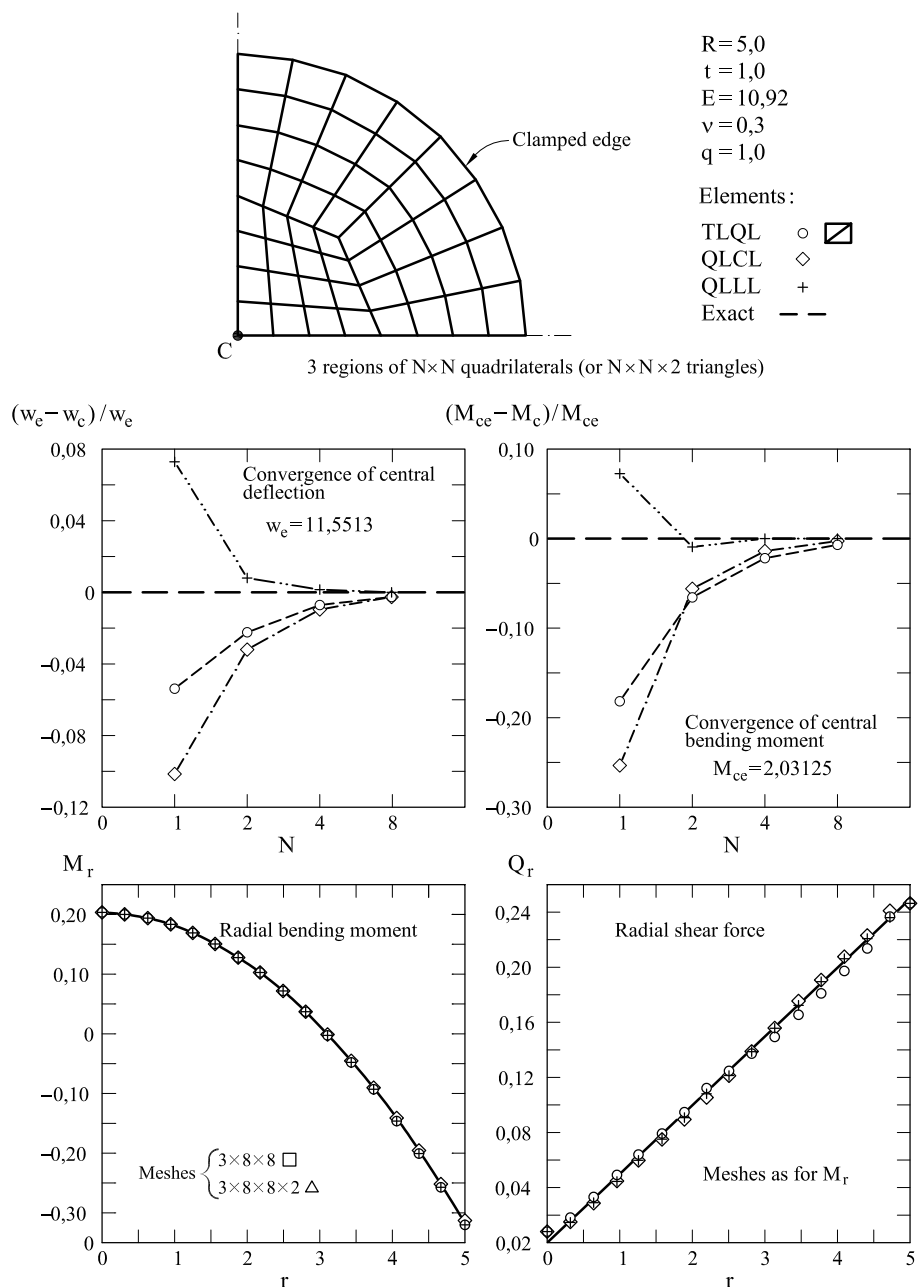


**Fig. 6.33** Clamped circular plate ( $t/R = 0.20$ ) under uniform load analyzed with TLQL, QLLL and QLQL elements. Convergence of central deflection  $w_c$  and central bending moment ( $M_{x_c} = M_{y_c} = M_c$ ) towards exact values  $w_e$  and  $M_{ce}$ . Distribution of radial bending moment  $M_r$  and radial shear force  $Q_r$  along a radius. Exact results taken from Appendix H



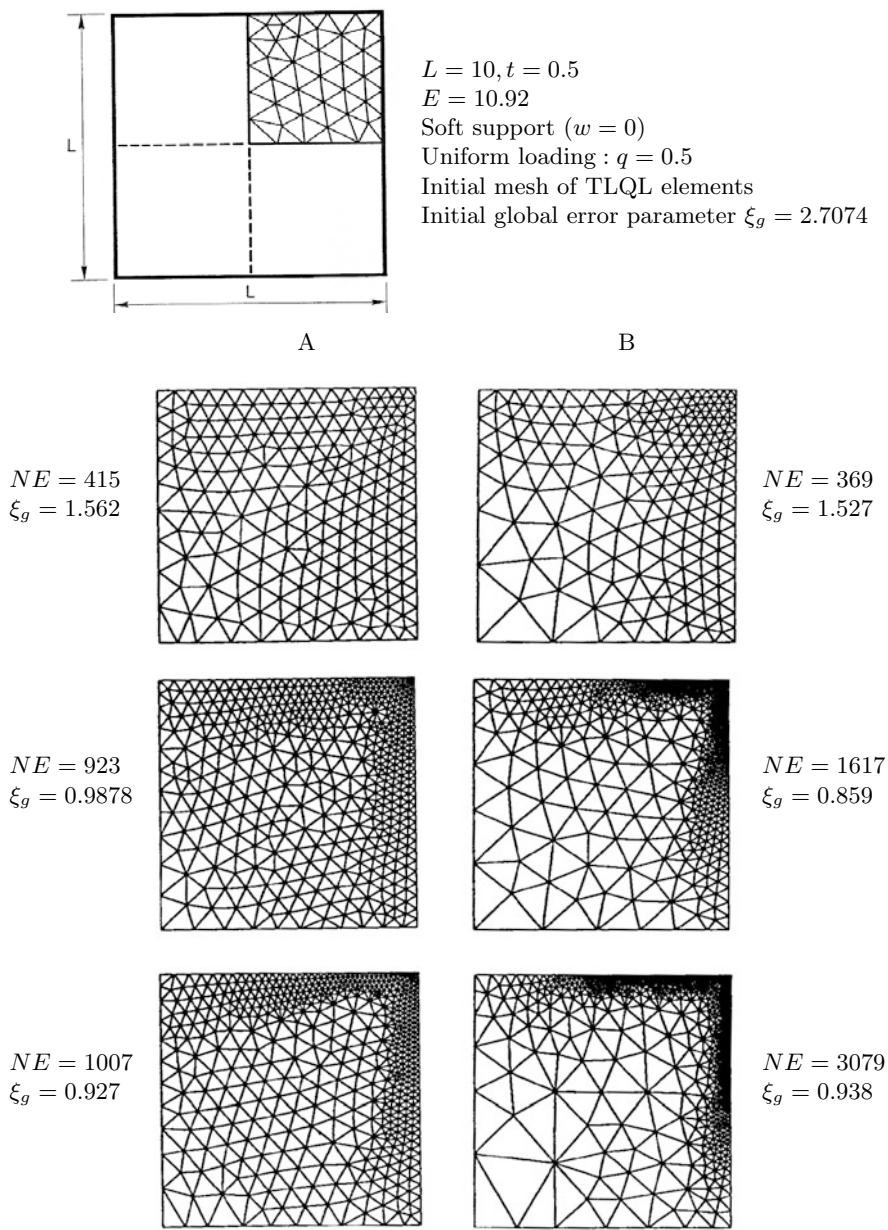


**Fig. 6.34** Symmetric quadrant of a SS (soft) plate under uniform loading. Sequence of meshes obtained with mesh adaption strategies based on: Uniform distribution of the global error (column A); Uniform distribution of the error density (column B); Target global error:  $\eta = 5\%$ ;  $NE$  = number of elements [On4,OCK]

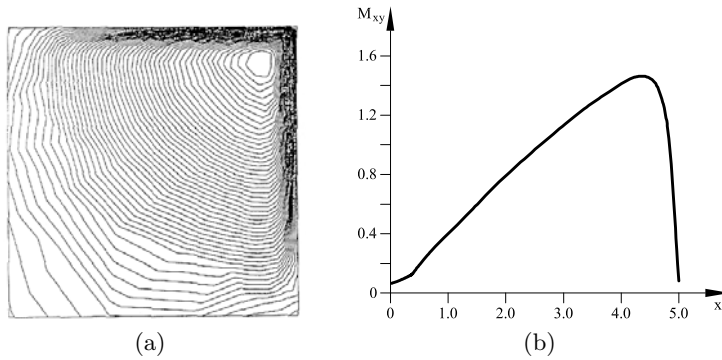


**Fig. 6.35** Symmetric quadrant ( $5.0 \times 5.0$ ) of a SS (soft) plate under uniform loading. a) Isolines for the torque  $M_{xy}$ ; b) Distribution of  $M_{xy}$  along the line  $y = 2.5$ . Results obtained with the mesh of 3079 TLQL elements of Figure 6.34

larger number of elements. Its advantage, however, is that it captures very well the boundary layer for the torque  $M_{xy}$  (Figure 6.35).

### 6.14.3 Effect of shear deformation in a plate simply supported at three edges under a line load acting on the free edge

The plate is displayed in Figure 6.36, where the geometry, the boundary conditions and the uniformly distributed loading along the edge is also shown. The edge loading induces high transverse shear stresses and strains near the edge, which play an important role in total deflection value for thick situations. This example was analyzed in [On] using 20 Reissner-Mindlin linear strip elements (Chapter 11) and in [Bl] using a mesh of  $10 \times 10$  QLLL plate elements. In both cases half of the plate was studied due to symmetry, with a finer mesh in the vicinity of the free edge. Both experimental [AR] and analytical results (based on Kirchhoff thin plate theory) [TW] are available.

Figure 6.36a shows the distribution of the maximum  $\sigma_x$  stress in the center of the free edge for different line load intensities ( $\frac{d}{a}$ ) and two values of the ratio  $\frac{t}{a} = \frac{1}{20}$  and  $\frac{1}{4}$ . The Kirchhoff analytical solution is independent of the thickness and it differs in excess from the Reissner-Mindlin finite element solution as the load concentrates and the thickness increases. This difference raises to 60% for a thick plate ( $t/a = 1/4$ ).

Figures 6.36b and c show the distribution of  $\sigma_x$  on the plate surface along several lines parallel to the loaded edge for a load intensity of  $\frac{d}{a} = 0.01$  and two thickness ratios of  $\frac{t}{a} = \frac{1}{20}$  and  $\frac{1}{4}$ , respectively. At

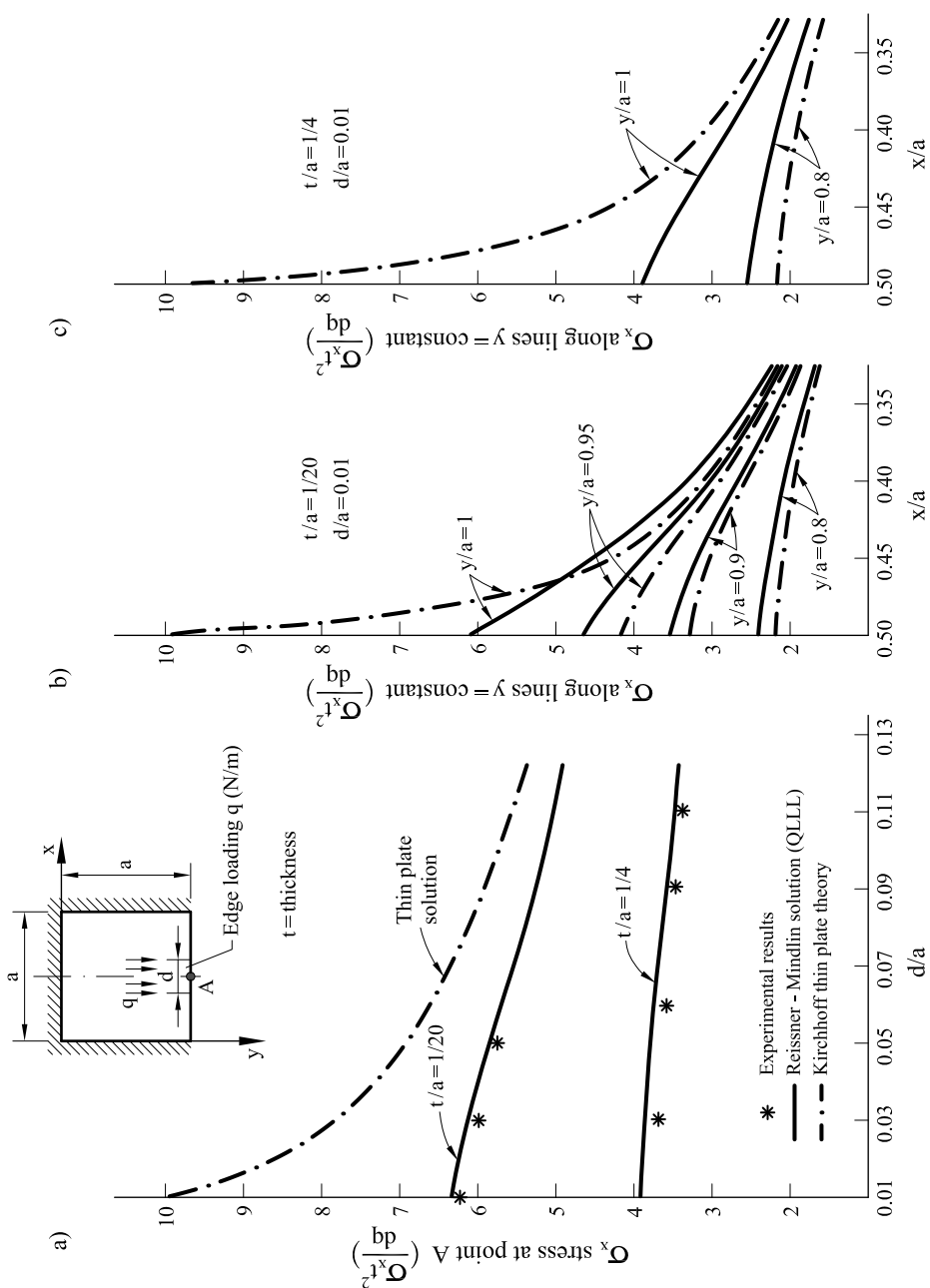


**Fig. 6.36** Square plate simply supported (soft) at three edges under a line loading acting on the free edge. Distribution of  $\sigma_x$  using Kirchhoff thin plate theory (analytical) and  $10 \times 10$  QLLL elements

the mid-point of the free edge ( $\frac{y}{a} = 1, \frac{x}{a} = 0.5$ ) the thin plate (Kirchhoff) solution yields a much larger value than the thick (Reissner-Mindlin) one, as expected.

The differences between the thin and thick plate solutions diminish as we move away from the edge and from the plate center. It is interesting that Reissner-Mindlin results are larger than the Kirchhoff values in these regions.

This example clearly shows the importance of accounting for the transverse shear deformation effects in certain situations.

## 6.15 EXTENDED ROTATION-FREE PLATE TRIANGLE WITH SHEAR DEFORMATION EFFECTS

The rotation-free basic plate triangle (BPT) of Section 5.8.2 can be extended to account for shear deformation effects. The enhanced element is termed BPT+1. The method is similar to that used to introduce shear deformation in the rotation-free CCB beam element (Section 2.10).

The curvatures in the BPT+1 element are expressed in terms of the deflection and the shear angles  $\phi_x, \phi_y$  substituting Eqs.(6.3) and (6.4) into (6.9) as

$$\hat{\epsilon}_b = \left\{ \begin{array}{c} \frac{\partial^2 w}{\partial x^2} + \frac{\partial \phi}{\partial x} \\ \frac{\partial^2 w}{\partial y^2} + \frac{\partial \phi_y}{\partial y} \\ 2 \frac{\partial^2 w}{\partial x \partial y} + \left( \frac{\partial \phi_x}{\partial y} + \frac{\partial \phi_y}{\partial x} \right) \end{array} \right\} = \kappa_w + \kappa_\phi \quad (6.155)$$

where

$$\kappa_w = \left[ \frac{\partial^2 w}{\partial x^2}, \frac{\partial^2 w}{\partial y^2}, 2 \frac{\partial^2 w}{\partial x \partial y} \right]^T, \quad \kappa_\phi = \left[ \frac{\partial \phi_x}{\partial x}, \frac{\partial \phi_y}{\partial y}, \frac{\partial \phi_y}{\partial x} + \frac{\partial \phi_x}{\partial y} \right]^T \quad (6.156)$$

are termed the geometrical curvature and the transverse shear curvature, respectively.

The transverse shear strains are expressed in terms of  $\phi_x$  and  $\phi_y$  as

$$\hat{\epsilon}_s = \left[ \frac{\partial w}{\partial x} - \theta_x, \frac{\partial w}{\partial y} - \theta_y \right]^T = -[\phi_x, \phi_y]^T = -\phi \quad (6.157)$$

The PVW is written substituting Eqs.(6.155) and (6.157) into (6.26a) (assuming a distributed vertical load  $f_z$  to act only). This gives

$$\iint_A [[\delta\boldsymbol{\kappa}_w + \delta\boldsymbol{\kappa}_\phi]^T \hat{\boldsymbol{\sigma}}_b - \delta\boldsymbol{\phi}^T \hat{\boldsymbol{\sigma}}_s] dA - \iint_A \delta w f_z dA = 0 \quad (6.158)$$

Eq.(6.158) is split in the following two independent equations

$$\iint_A \delta\boldsymbol{\kappa}_w^T \hat{\boldsymbol{\sigma}}_b dA - \iint_A \delta w f_z dA = 0 \quad (6.159)$$

$$\iint_A [\delta\boldsymbol{\kappa}_\phi^T \hat{\boldsymbol{\sigma}}_b - \delta\boldsymbol{\phi}^T \hat{\boldsymbol{\sigma}}_s] dA = 0 \quad (6.160)$$

The plate is discretized into 3-noded triangles. The deflection is linearly interpolated in terms of the nodal values within the  $p$ th triangle as

$$w = \sum_{i=1}^i N_i w_i = \mathbf{N}_w^p \mathbf{w}^p \quad , \quad \mathbf{N}_w^p = [N_1, N_2, N_3] \quad , \quad \mathbf{w}^p = [w_1, w_2, w_3]^T \quad (6.161)$$

In Eq.(6.161)  $N_i$  is the shape function for the 3-noded linear  $C^0$  triangle with area  $A^i$ , i.e.

$$N_i = \frac{1}{2A^i} (a_i + b_{ix} + c_{iy}) \quad \text{with} \quad a_i = x_j y_k - x_i y_j, \quad b_i = y_j - y_k, \quad c_i = x_k - x_j \quad (6.162)$$

We assume an average value for the geometrical curvature field  $\boldsymbol{\kappa}_w^p$  over a 3-noded triangle following the method described in Section 5.8.1, i.e.,

$$\boldsymbol{\kappa}_w = \boldsymbol{\kappa}_w^p = \frac{1}{A_p} \left[ \iint_{A^p} \boldsymbol{\kappa}_w dA \right] = \frac{1}{A_p} \int_{\Gamma_p} \mathbf{T} \nabla w d\Gamma \quad (6.163)$$

where  $\mathbf{T}$  contains the components of the outward unit normal to the boundary  $\Gamma_p$  of element  $p$  (Eq.(5.69a) and Figure 6.37).

Substituting the approximation (6.161) into (6.163) and following the procedure described in Section 5.8.2 gives

$$\boldsymbol{\kappa}_w^p = \mathbf{B}_w \bar{\mathbf{w}}^p \quad (6.164)$$

where  $\mathbf{B}_w$  coincides with matrix  $\mathbf{B}^p$  of Eq.(5.84b) and  $\bar{\mathbf{w}}^p$  is defined in Eq.(5.83).

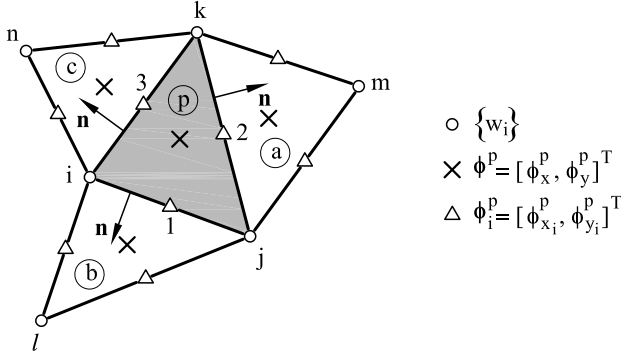


**Fig. 6.37** Four-element patch for the  $p$ th BPT+1 triangle ( $ijk$ ). Nodal deflections ( $w_i$ ), transverse shear strains for each element in the patch ( $\phi^p$ ) and at the mid-side points of element  $p$  ( $\phi_i^p$ )

The transverse shear curvature within the central triangle  $p$  is computed as follows. First the shear angles are assumed to be constant within each triangle, i.e. for the  $p$ th triangle (Figure 6.37)

$$\phi = \phi^p \quad \text{with} \quad \phi^p = [\phi_x^p, \phi_y^p]^T \quad (6.165)$$

An average value of the transverse shear curvature over the  $p$ th triangle is assumed as  $\kappa_\phi = \kappa_\phi^p$  where

$$\kappa_\phi^p = \frac{1}{A_p} \iint_{A_p} \kappa_\phi dA = \frac{1}{A_p} \int_{\Gamma^p} \mathbf{T} \phi d\Gamma = \frac{1}{A_p} \sum_{j=i}^3 l_j^p \mathbf{T}_j^p \phi_j^p = \mathbf{C}_p \hat{\phi}^p \quad (6.166)$$

where  $\mathbf{C}_p$  is given in Eq.(5.80b),  $l_j^p$  are the element sides and

$$\hat{\phi}^p = \begin{Bmatrix} \phi_1^p \\ \phi_2^p \\ \phi_3^p \end{Bmatrix} \quad (6.167)$$

where  $\phi_i^p$  are the values of the shear angles at the mid-side points of element  $p$  (Figure 6.37). As the shear angles are discontinuous at the element sides, vector  $\phi^p$  is expressed in terms of the constant shear angles for the four elements in the patch via a simple averaging procedure as

$$\phi^p = \mathbf{M}_p \bar{\phi}^p \quad \text{with} \quad \bar{\phi}^p = \begin{Bmatrix} \phi^p \\ \phi^a \\ \phi^b \\ \phi^c \end{Bmatrix} \quad (6.168)$$



where  $\mathbf{M}_p$  is given by Eq.(5.81b).

Substituting Eq.(6.168) into (6.166) gives

$$\boldsymbol{\kappa}_\phi^p = \mathbf{C}_p \mathbf{M}_p \bar{\boldsymbol{\phi}}^p = \mathbf{B}_\phi \bar{\boldsymbol{\phi}}^p \quad \text{with} \quad \mathbf{B}_\phi = \mathbf{C}_p \mathbf{M}_p \quad (6.169)$$

Substituting Eqs.(6.169) and (6.164) into (6.155) gives

$$\hat{\boldsymbol{\varepsilon}}_b^p = \mathbf{B}_w \bar{\mathbf{w}}^p + \mathbf{B}_\phi \bar{\boldsymbol{\phi}}^p \quad (6.170)$$

We assume a constant bending moment field  $\hat{\boldsymbol{\sigma}}_b^p$  over the element expressed in terms of the nodal deflections and the nodal shear angles as

$$\hat{\boldsymbol{\sigma}}_b^p = \hat{\mathbf{D}}_b^p \hat{\boldsymbol{\varepsilon}}_b^p = \hat{\mathbf{D}}_b^p [\mathbf{B}_w \bar{\mathbf{w}}^p + \mathbf{B}_\phi \bar{\boldsymbol{\phi}}^p] \quad (6.171)$$

where  $\hat{\mathbf{D}}_b^p = \frac{1}{A_p} \iint_{A_p} \hat{\mathbf{D}}_b dA$  is an average bending constitutive matrix.

The constitutive equation for the shear forces is written as

$$\hat{\boldsymbol{\sigma}}_s = \hat{\mathbf{D}}_s \hat{\boldsymbol{\varepsilon}}_s = -\hat{\mathbf{D}}_s \boldsymbol{\phi} = -\hat{\mathbf{D}}_s \mathbf{M}_p \bar{\boldsymbol{\phi}}^p \quad (6.172)$$

Substituting the assumed constant curvature fields  $\boldsymbol{\kappa}_w^p$  and  $\boldsymbol{\kappa}_\phi^p$  (via Eqs.(6.164) and (6.169)) in the PVW (Eqs.(6.159) and (6.160)) gives

$$\begin{aligned} \sum_p \left\{ [\delta \bar{\mathbf{w}}^p]^T \mathbf{B}_w^T \hat{\boldsymbol{\sigma}}_b^p A_p - \iint_{A_p} \delta w f_z dA \right\} &= 0 \\ \sum_p \left\{ [\delta \bar{\boldsymbol{\phi}}^p]^T \mathbf{B}_\phi^T \hat{\boldsymbol{\sigma}}_b^p A_p - \int_{A_p} [\delta \bar{\boldsymbol{\phi}}^p]^T \hat{\boldsymbol{\sigma}}_s dA \right\} &= 0 \end{aligned} \quad (6.173)$$

Substituting Eqs.(6.171) and (6.172) into (6.174) gives

$$\begin{aligned} \sum_p [\delta \bar{\mathbf{w}}^p]^T \left\{ [\mathbf{B}_w^T \hat{\mathbf{D}}_b \mathbf{B}_w \bar{\mathbf{w}}^p + \mathbf{B}_w^T \hat{\mathbf{D}}_b \mathbf{B}_\phi \bar{\boldsymbol{\phi}}^p] A_p - \iint_{A_p} \bar{\mathbf{N}}^p \bar{\mathbf{f}} dA \right\} &= 0 \\ \sum_p [\delta \bar{\boldsymbol{\phi}}^p]^T \left\{ \mathbf{B}_\phi^T \hat{\mathbf{D}}_b \mathbf{B}_w A_p \bar{\mathbf{w}}^p + \left( \mathbf{B}_\phi^T \hat{\mathbf{D}}_b \mathbf{B}_\phi A_p + \iint_{A_p} \mathbf{M}_p^T \hat{\mathbf{D}}_s \mathbf{M}_p dA \right) \bar{\boldsymbol{\phi}}^p \right\} &= 0 \end{aligned} \quad (6.174)$$

The sums in Eqs.(6.173) and (6.174) extend over all the triangles in the mesh and

$$\bar{\mathbf{N}}^p = [N_1, N_2, N_3, 0, 0, 0]^T \quad , \quad \bar{\mathbf{f}} = f_z [1, 1, 1, 0, 0, 0]^T \quad (6.175)$$

Simplification of the virtual DOFs yields the system of equations

$$\begin{aligned} \mathbf{K}_w \mathbf{w} + \mathbf{K}_{w\phi} \boldsymbol{\phi} &= \mathbf{f}_w \\ \mathbf{K}_{w\phi}^T \mathbf{w} + \mathbf{K}_\phi \boldsymbol{\phi} &= \mathbf{0} \end{aligned} \quad (6.176)$$

with

$$\mathbf{w} = [w_1, w_2, \dots, w_N]^T, \quad \boldsymbol{\phi} = [(\boldsymbol{\phi}^1)^T, (\boldsymbol{\phi}^2)^T, \dots, (\boldsymbol{\phi}^{n_e})^T]^T \quad (6.177)$$

where  $N$  is the total number of nodes and  $n_e$  is the total number of elements in the mesh.

The global matrices and vectors are assembled from the element contributions in the usual manner with

$$\begin{aligned} \mathbf{K}_w^p &= \mathbf{B}_w^T \hat{\mathbf{D}}_b^p \mathbf{B}_w A^p, \quad \mathbf{K}_{w\phi}^p = \mathbf{B}_w^T \hat{\mathbf{D}}_b^p \mathbf{B}_\phi A^p \\ \mathbf{K}_\phi^p &= \left[ \mathbf{B}_\phi^T \hat{\mathbf{D}}_b^p \mathbf{B}_\phi + \mathbf{M}_p^T \hat{\mathbf{D}}_s \mathbf{M}_p \right] A^p \end{aligned} \quad (6.178)$$

In the derivation of the second term in  $\mathbf{K}_\phi^p$  we have assumed a constant transverse shear constitutive matrix  $\hat{\mathbf{D}}_s$  over the element.

For a uniformly distributed load  $f_z = q$  and

$$\mathbf{f}_w^p = \frac{qA^p}{3} [1, 1, 1, 0, 0, 0]^T \quad (6.179)$$

Note the similarity of Eqs.(6.176) with Eq.(2.125) obtained for an analogous rotation-free beam element.

### 6.15.1 Iterative solution scheme

The following iterative scheme is recommended for solving Eqs.(6.176).

**Step 1. Compute the nodal deflections  $\mathbf{w}^1$**

$$\mathbf{K}_w \mathbf{w}^1 = \mathbf{f}_w \rightarrow \mathbf{w}^1 \quad (\text{Kirchhoff thin plate solution}) \quad (6.180)$$

**Step 2. Compute  $\boldsymbol{\phi}^i$ ,  $i \geq 1$**

$$\mathbf{K}_\phi \boldsymbol{\phi}^i = \mathbf{f}_\phi - \mathbf{K}_{w\phi}^T \mathbf{w}^i \rightarrow \boldsymbol{\phi}^i \quad (6.181)$$

**Step 3. Compute  $\mathbf{w}^i$ ,  $i > 1$**

$$\mathbf{K}_w \mathbf{w}^i = \mathbf{f}_w - \mathbf{K}_{w\phi} \boldsymbol{\phi}^{i-1} \rightarrow \bar{\mathbf{w}}^i \quad (6.182)$$

**Return to step 2.**

Convergence of the above iterative scheme is quite fast (2–4 iterations), even for thick plates [OZ2,3].

## 6.15.2 Boundary conditions

### Free edge

A BPT+1 element with a side along a free boundary edge has one of the triangles belonging to the patch missing. This is taken into account by ignoring the contributions of this triangle when computing  $\mathbf{B}_w$  and  $\mathbf{B}_\phi$ . This can be implemented by a simple modification of matrix  $\mathbf{M}_p$  in Eq.(6.168), similarly as described for the BPT element in Section 5.8.2.1.

### Simple supported (SS) edge

Soft (SS) condition ( $w = 0, \frac{\partial w}{\partial s} = 0$ ): The two edge deflections  $w_i$  and  $w_j$  are prescribed to a zero value when solving the system of equations.

Hard (SS) condition ( $w = 0, \theta_s = 0$ ). The condition  $w_i = 0$  at the  $SS$  nodes is imposed when solving the global system of equations.

The condition  $\theta_s = 0$  is introduced using a penalty method as follows. The expression for the virtual work is extended by adding to Eq.(6.158) the term  $\alpha l_i^p \delta \theta_s \theta_s$ , where  $\alpha l_i^p$  is the length of the  $SS$  side and  $\alpha$  is a large number that plays the role of a penalty parameter. The tangential rotation is expressed in terms of the nodal deflection and shear angle variables as

$$\begin{aligned} \theta_s &= \theta_x C_\alpha + \theta_y S_\alpha = \left( \frac{\partial w}{\partial x} + \phi_x \right) C_\alpha + \left( \frac{\partial w}{\partial y} + \phi_y \right) S_\alpha \\ &= \frac{1}{2A_p} \sum_{i=1}^3 (b_i C_\alpha + c_i S_\alpha) w_i + \phi_x^p C_\alpha + \phi_y^p S_\alpha \end{aligned} \quad (6.183)$$

where  $b_i, c_i$  are given in Eq.(6.162),  $C_\alpha = \cos \alpha$ ,  $S_\alpha = \sin \alpha$  and  $\alpha$  is the angle that the  $SS$  side forms with the  $x$  axis. Eq.(6.183) is grouped as

$$\theta_s = \mathbf{P}_w \bar{\mathbf{w}}^p + \mathbf{P}_\phi \bar{\boldsymbol{\phi}}^p \quad (6.184)$$

with

$$\begin{aligned} \mathbf{P}_w &= [P_1, P_2, P_3, 0, 0, 0] \quad , \quad P_i = \frac{1}{2A_p} (b_i C_\alpha + c_i S_\alpha) \\ \mathbf{P}_\phi &= [C_\alpha, S_\alpha, 0, 0, 0, 0, 0] \end{aligned} \quad (6.185)$$

Introducing the approximation (6.184) in the penalty term gives

$$\alpha l_i^p \delta \theta_s \theta_s = \alpha l_i^p [\mathbf{P}_w^T (\delta \bar{\mathbf{w}}^p)^T + \mathbf{P}_\phi^T (\delta \bar{\boldsymbol{\phi}}^p)^T] [\mathbf{P}_w \bar{\mathbf{w}}^p + \mathbf{P}_\phi \bar{\boldsymbol{\phi}}^p] \quad (6.186)$$

The contribution of Eq.(6.186) to the element matrices is

$$\bar{\mathbf{K}}_w^p = \mathbf{K}_w^p + \alpha l_i^p \mathbf{P}_w^T \mathbf{P}_w \quad , \quad \bar{\mathbf{K}}_{w\phi}^p = \mathbf{K}_{w\phi}^p + \alpha l_i^p \mathbf{P}_\phi^T \mathbf{P}_\phi$$

$$\bar{\mathbf{K}}_\phi^p = \mathbf{K}_\phi^p + \alpha l_i^p \mathbf{P}_\phi^T \mathbf{P}_\phi \quad (6.187)$$

where  $\mathbf{K}_w^p$ ,  $\mathbf{K}_{w\phi}^p$  and  $\mathbf{K}_\phi^p$  are given in Eq.(6.178).

Clearly as the parameter  $\alpha$  increases, the condition  $\theta_s = 0$  is better satisfied. In practice a value  $\alpha = 10^5 Et^3$  suffices to obtain accurate results.

### Clamped edge ( $\theta = 0$ )

The contribution of a clamped edge to the curvatures  $\kappa_w^p$  and  $\kappa_\phi^p$  is neglected. This implies modifying matrix  $\mathbf{M}_p$  as explained in Section 5.8.2.1. In addition, the edge deflections are prescribed to a zero value.

### Symmetry edge ( $\theta_n = 0$ )

The condition  $\theta_n = 0$  at a symmetry edge is imposed via a penalty approach similar as for the SS (hard) case. The PVW is enhanced with the term

$$\alpha l_i^p \delta \theta_n \theta_n = \alpha l_i^p [\mathbf{P}_w^T (\delta \bar{\mathbf{w}}^p)^T + \mathbf{P}_\phi^T (\delta \bar{\boldsymbol{\phi}}^p)^T] [\mathbf{P}_w \bar{\mathbf{w}}^p + \mathbf{P}_\phi \bar{\boldsymbol{\phi}}^p] \quad (6.188)$$

where  $\mathbf{P}_w$  and  $\mathbf{P}_\phi$  are given in Eq.(6.185) with  $P_i = \frac{1}{2A_p} [b_i S_\alpha - c_i C_\alpha]$ . The element matrices are modified as in Eq.(6.187).

## 6.15.3 Examples of performance of the BPT+1 element

The efficiency and accuracy of the BPT+1 element has been tested in the analysis of simply supported (SS, soft) square plates of side  $L$  and circular plates of diameter  $2L$  under uniformly distributed loading and clamped or square plates under a central point load. The study was performed for different thicknesses ranging from  $t/L = 10^{-3}$  (very thin plate) to  $t/L = 0.1$  (thick plate) and several uniform meshes with increasing number of elements *in all the plate surface*.

Results of the study using the iterative scheme of Section 6.15.1 are presented in [Figures 6.38–6.40](#). Each figure shows:

- (a) The convergence of the vertical deflection and the shear angles with the number of iterations measured as

$$L_2^w = \left[ \sum_{j=1}^N \frac{(w_j^i - w_j^{i-1})^2}{(w_j^i)^2} \right]^{1/2}, \quad L_2^\phi = \left[ \sum_{j=1}^{n_e} \frac{[\boldsymbol{\phi}_j^i - \boldsymbol{\phi}_j^{i-1}]^T (\boldsymbol{\phi}_j^i - \boldsymbol{\phi}_j^{i-1})}{[\boldsymbol{\phi}_j^i]^T \boldsymbol{\phi}_j^i} \right]^{1/2} \quad (6.189)$$

where  $N$  is the number of nodes in the mesh and an upper index denotes the iteration number. A value of  $w_j^0 = 0$  and  $\phi_j^0 = \mathbf{0}$  has been taken. The iterative scheme stops when  $L_2^w < 10^{-3}$ .

- (b) The ratio between the normalized central deflection and a reference solution for four values of  $t/L = 10^{-3}, 10^{-2}, 5 \times 10^{-2}$  and  $10^{-1}$  for each of the meshes considered. For cases when an analytical solution is not available we have used as the reference solution the 3D FEM results for the deflection at the center of the middle plane using a mesh of  $40 \times 40 \times 6$  8-noded hexahedra [On4] in a quarter of plate. For the clamped plate under central point load the analytical value for the deflection under the load given by thick plate theory is infinity (See Section 6.16). Hence, results for the deflection for thick plates ( $t/L = 0.05$  and  $t/L = 0.10$ ) are compared at the mid-point  $D$  along a central line in this case (Figure 6.39).
- (c) The distribution of the bending moment  $M_x$  and the shear force  $Q_x$  along the central line for the thick case ( $t/L = 0.10$ ) for each of the five meshes considered. The isovalues of  $M_x$  and  $Q_x$  over a quarter of the plate are also shown for the finer mesh.

The following conclusions are drawn from the examples:

- The BPT+ element reproduces accurately the expected results for the deflection field for thin and thick plates.
- A converged solution for the deflection field was obtained in a maximum of four iterations for all cases considered. The convergence of the shear angles is slightly slower than for the deflection field.
- The distribution of the bending moments and the shear forces was good and in accordance with the expected results for the thick case.
- For thin plates the distribution of bending moments is also very good. The distribution of the shear forces deteriorates slightly if computed via Eq.(6.172) as shear angles tend to zero as the plate is thinner. It is more appropriate in these cases to compute the shear forces from the bending moments via Eq.(5.23).
- Similar good results were obtained for the “hard” SS condition obtained by prescribing  $\bar{\phi}_{s_i} = 0$  at the support nodes (Table 6.5) [OZ2].

A similar 3-noded plate triangle element (called BPT+) was derived in [OZ2] using a continuous linear interpolation for the shear angles within each element. The BPT+1 element has a slightly superior behaviour for capturing shear force jumps [OZ2,3].

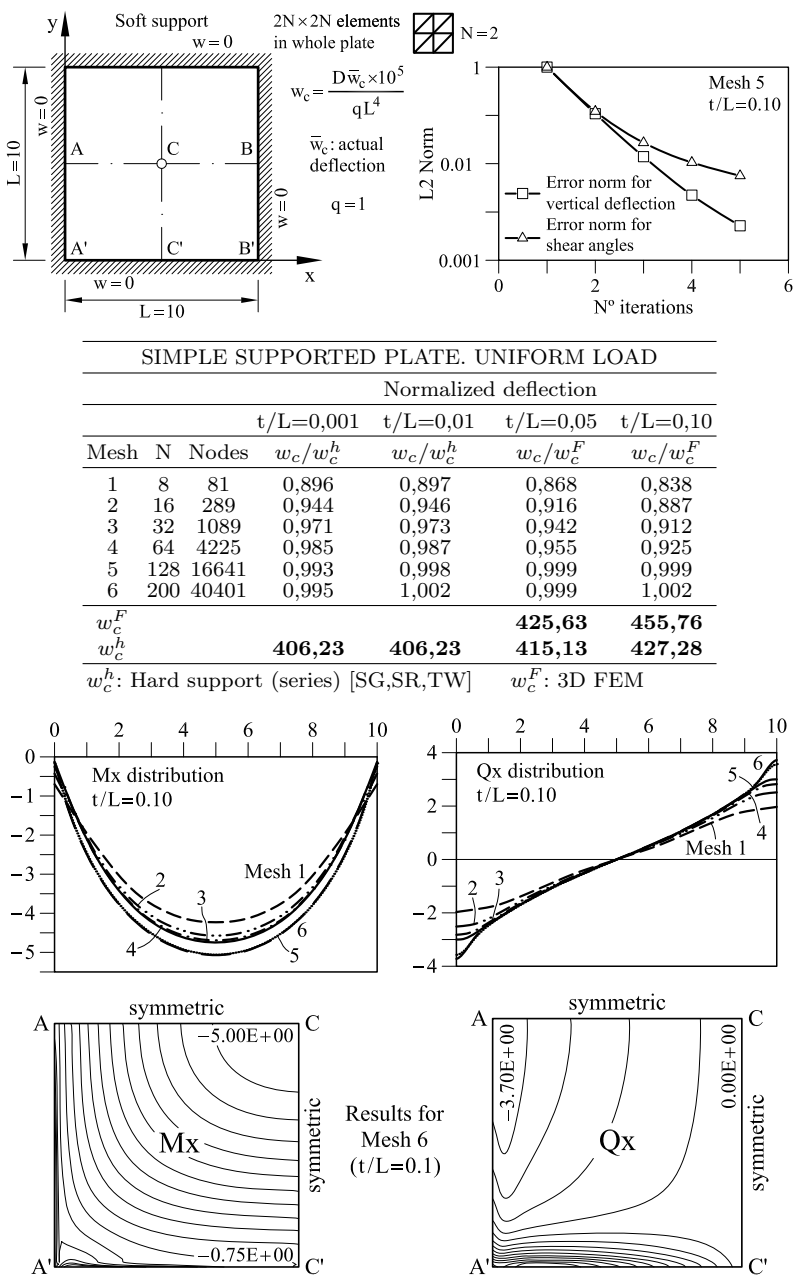


**Fig. 6.38** BPT+1 element. SS (Soft) square plate under uniform load ( $q = 1$ ). Table shows convergence of normalized central deflection  $w_c$  for different thicknesses. Upper curves show convergence of vertical deflection and shear angles for a thick plate with number of iterations. Lower diagrams show the distribution of  $M_x$  and  $Q_x$  along the central line and their contours

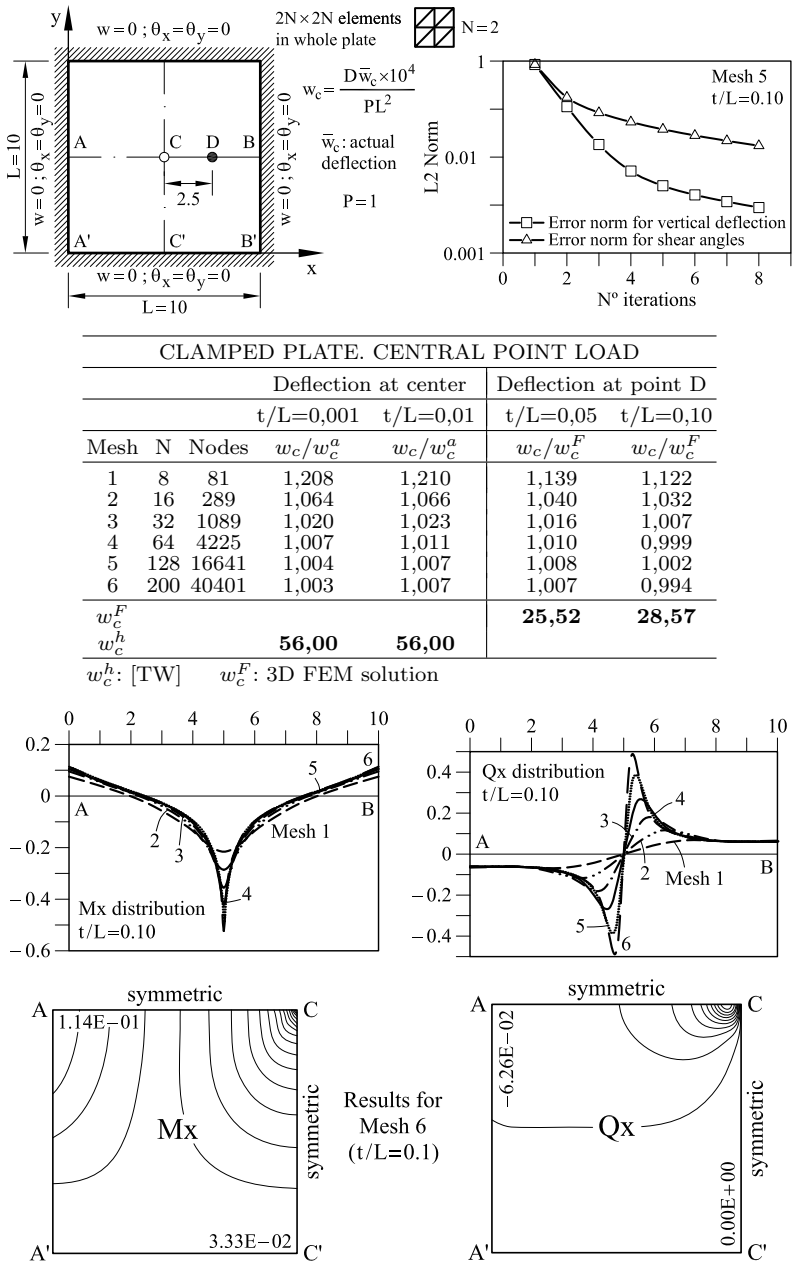


**Fig. 6.39** BPT+1 element. Clamped square plate under central point load ( $P = 1$ ). Table shows convergence of normalized central deflection  $w_c$  for different thicknesses. Upper curves show convergence of vertical deflection and shear angles for a thick plate with number of iterations. Lower diagrams show the distribution of  $M_x$  and  $Q_x$  along the central line and their contours

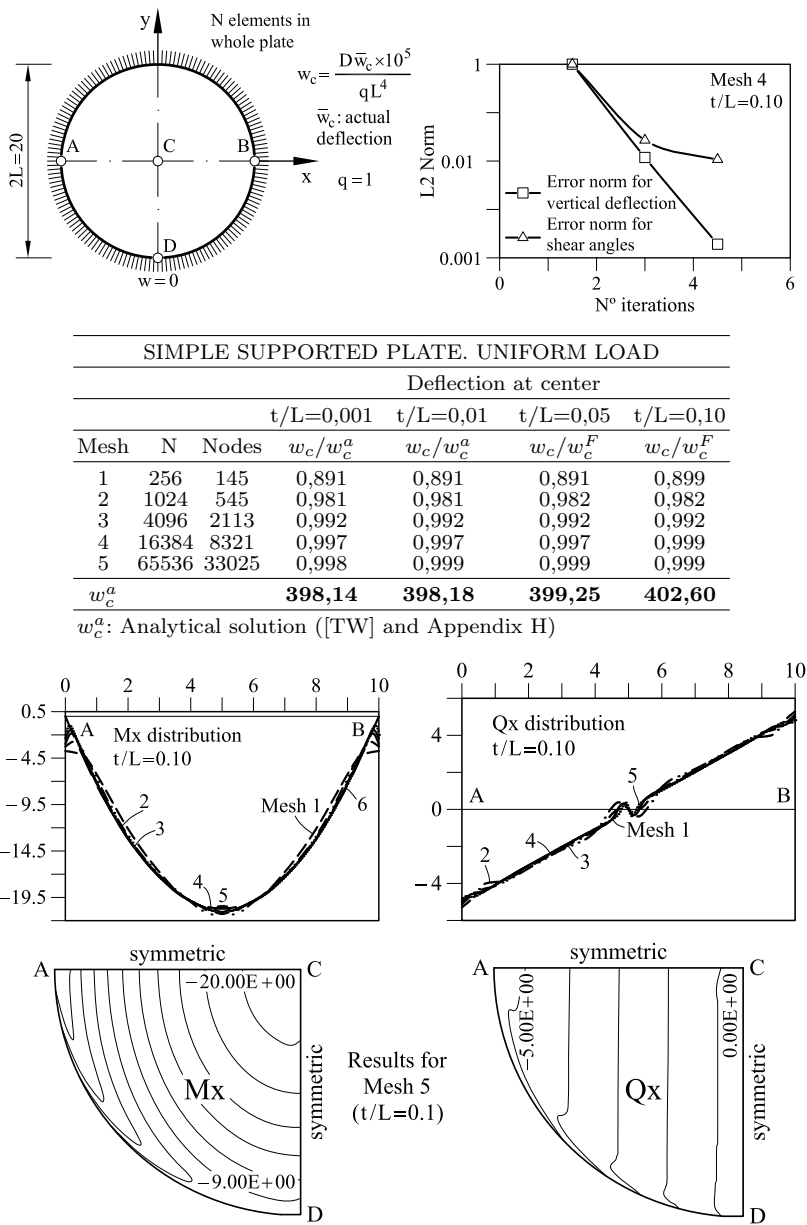


**Fig. 6.40** BPT+1 element. SS (soft) circular plate under uniform load ( $q = 1$ ). Table shows convergence of normalized central deflection  $w_c$  for different thicknesses. Upper curves show convergence of vertical deflection and shear angles for a thick plate with the number of iterations. Lower diagrams show the distribution of  $M_x$  and  $Q_x$  along the central line and their contours



SS (hard) square thick plate. Uniform load, $t/L = 0.10$						
	Mesh 1	Mesh 2	Mesh 3	Mesh 4	Mesh 5	Mesh 6
$w_c$	381,73	404,59	416,31	421,98	424,65	425,59
$w_c/w_c^h$	0,893	0,947	0,974	0,988	0,994	0,996
$w_c^h$ (Series solution): 427.28 [SG,SR,TW]						
Convergence achieved in a maximum of 4 iterations for each mesh						

**Table 6.5** BPT+1 element. SS square thick plate (hard support) under uniform load. Normalized central deflection values for  $t/L = 0.10$

Mesh, $M$	$t/L = 10^{-1}; w_c \times 10^{-2}$		$t/L = 10^{-3}; w_c \times 10^{-7}$	
	hard support	soft support	hard support	soft support
2	4.2626	4.6085	4.0389	4.2397
4	4.2720	4.5629	4.0607	4.1297
8	4.2727	4.5883	4.0637	4.0928
16	4.2728	4.6077	4.0643	4.0773
32	4.2728	4.6144	4.0644	4.0700
Series [SG,SR,TW]	4.2728		4.0624	

**Table 6.6** BPT+1 element. Normalized center displacement ( $w_c$ ) for SS plate under uniform load for two  $t/L$  ratios;  $E = 10.92$ ,  $\nu = 0.3$ ,  $L = 10$ ,  $f_z = 1$ .

6.16 LIMITATIONS OF THIN PLATE THEORY

Kirchhoff plate element have obviously limitations to reproduce the behaviour of thick plates. Reissner-Mindlin plate elements are superior as they are applicable to thick and thin situation. Table 6.6 taken from [ZT2] shows some results obtained for SS plates with hard and soft support conditions under uniform load for two different side length/thickness ratios. Numerical results were obtained with the 4-noded QLLL element (Section 6.7.1) but the conclusions hold for any Reissner-Mindlin plate element. The effect of the hard and soft SS conditions is clearly shown in the table. The central deflection for the thick plate always converges to *larger values* than those given by thin plate theory. Also for the SS case the soft support condition yields larger deflection values, as expected. These differences can be more pronounced in different plate configurations.

Figure 6.41 shows results for a simple supported rombic plate for  $L/t = 100$  and 1000 analyzed with the triangular element of Zienkiewicz and Lefebvre (Figure 6.25). There is an exact solution for this problem using Kirchhoff plate theory [Mo4]. Results for the “thicker” case ( $L/t = 100$ )

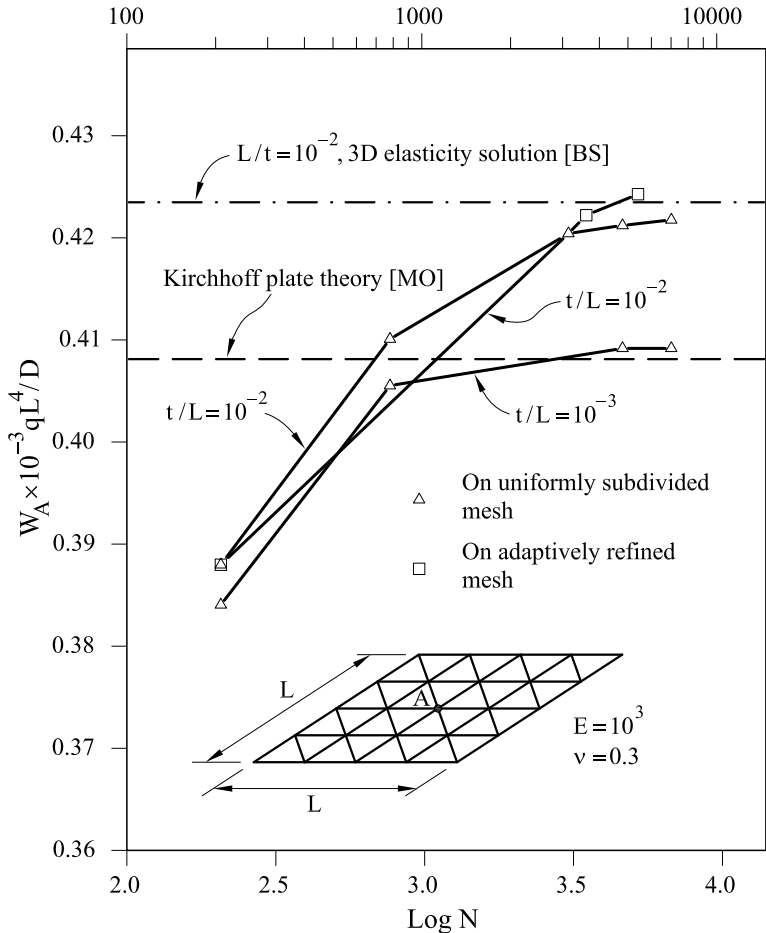


**Fig. 6.41** Skew rhombic plate ( $30^\circ$ ) with soft SS conditions under uniform load. Convergence of central deflection with the number of DOFs. The problem was solved with the triangle of Zienkiewicz and Lefebvre [ZL2] (Section 6.9)

converge to a central deflection value which is 4% larger than the exact thin plate solution.

Babüška and Scapolla [BS] studied this problem using 3D elasticity theory with “soft” support conditions which approximate better the physical problem. 3D results for  $L/t = 100$  are close to the thick plate solution. This confirms the superiority of Reissner-Mindlin theory for this problem.

We note finally an important difference between thick and thin plates when point loads are involved. In the thin case the deflection  $w$  remains

finite under the load. However, as mentioned earlier, transverse shear deformation effects *lead to an infinite displacement under the load for thick plates* (as indeed 3D elasticity theory predicts). In finite element approximations one always predicts a finite displacement at point load locations with the magnitude increasing without limit as a mesh is refined near the point load. Thus, *it is meaningless to compare the deflections at point load locations*. It is recommended to compare the total strain energy for such situations [ZT2].

## 6.17 CONCLUSIONS

Reissner-Mindlin plate theory is the basis for systematically deriving  $C^0$  continuous plate elements which include transverse shear strain effects. Practically, the only drawback of Reissner-Mindlin plate elements is the appearance of shear locking for thin plate situations. The reduced integration of the transverse shear stiffness terms is a simple and efficient procedure for eliminating shear locking, although it can introduce spurious mechanisms which can pollute the solution in some cases. The assumed transverse shear strain technique is a more consistent approach for designing robust locking-free plate elements and some of these elements have been presented in detail.

We note the good performance of the low order QLLL quadrilateral and the TLLL triangle based on assumed transverse shear strain fields.

Reissner-Mindlin plate elements are also the starting point for deriving Discrete-Kirchhoff thin plate elements, while keeping all the features of the  $C^0$  continuous formulation.

The merits of the Reissner-Mindlin plate formulation will show clearer when dealing with composite plates and shells in the subsequent chapters.